Politecnico di Milano

School of industrial and information Engineering
Department of Physics

Design and Implementation of a Terahertz Time-Domain Spectrometer

Master of Science in Engineering Physics
Photonics and Nano Optics

Supervisor:
Dr. Gianluca Galzerano
Co-Supervisor:
Eng. Lisa Marta Molteni

Master thesis of:
Matteo Perota

Academic year 2020-2021

Contents

List of Figures

List of Tables

Acknowledgments

I would like to express my sincere and personal gratitude to my thesis supervisor Dr. Gianluca Galzerano, for his precious teachings, warm guidance and the great effort he spent to make this work possible even through these difficult times. My profound thanks also to my co-supervisor Eng. Lisa Marta Molteni, for her endless patience, crucial advice and continued assistance. Special thanks to Dr. Francesco Canella and Eng. Edoardo Vicentini for their help each time I asked, and to Eng. Gabriele Di Noia for sharing with me most of this experience.

Finally, I want to acknowledge the invaluable support of my family and Martina during the five years of my engineering studies and the work of this thesis.

Abstract

This thesis reports on the design, development and characterization of a time-domain Terahertz spectrometer which relies on a pair of photoconductive antennas for both emission and detection of the Terahertz radiation. The system is pumped by an ultrafast Kerr lens mode locked Ti:Sapphire laser at 800 nm with a 250 MHz pulse repetition rate. The spectrometer has been characterized in terms of dynamic range, signal to noise ratio, detection bandwidth and spectral resolution, while different experimental parameters and signal processing techniques have been tested to optimize the raw signal. The spectrometer has been eventually used to carry out measurements of transmission function, refractive index and absorption coefficient on an heterogeneous set of materials encompassing plastic, paper, Gallium Phosphide and edible oils.

Introduction

The region of the electromagnetic spectrum included between microwave and infrared radiation has long been referred to as "the Terahertz gap", owning to limited accessibility by conventional electronic and optical techniques. Waves in this spectral range, loosely defined between 0.1 and 10 THz (3 mm to 30 μm), are characterized by a relatively low photon energy, resonant with vibrational modes of many molecules, and a long penetration depth in several materials opaque to visible light. These properties have stimulated the interest in Terahertz (THz) technology in many fields of fundamental research and have paved the way for a series of potential industrial applications. THz science has already left its mark in the security sector, with hazardous materials detection and baggage screening devices currently operating in airports all around the globe, and is expected to play a major role in several other fields such as biochemistry and material science, medicine and the food industry, just to mention a few.

Despite the great interest displayed since the late 1920s, the Terahertz region has long remained one of the least tapped of the electromagnetic spectrum. For large part of the 20-th century, the use of THz technologies was to a large extent restricted to the astronomy community for studying the background of cosmic far-infrared radiation, mainly because most of the techniques used to generate THz radiation shared common issues such as poor system stability, prohibitive size and inadequate efficiency. In the last thirty years however, owing to the fast evolution of semiconductor technologies and the emergence of ultrafast lasers, THz science has enjoyed an unprecedented pace of development, with a series of significant advances in both generation and detection of THz radiation. In particular, the invention of the photoconductive antenna by Auston et al. [1] and the subsequent improvement of these devices led to the development of coherent THz time domain spectroscopy (THz-TDS), which has nowadays established itself as perhaps the most reliable spectroscopy technique for material analysis in the THz range, mainly due to its broadband measurement capability and strong tolerance to background noise. A distinctive feature of THz-TDS is that it implements a coherent detection, which allow to measure both amplitude and phase of the acquired signal, thus opening to the possibility of using THz spectroscopy to completely characterize some of the key optical properties of a sample in the THz region, nominally the complex refractive index and the absorption coefficient.

The experimental work of this thesis deals with the design and characterization of a time domain THz spectrometer and its implementation for the analysis of the spectral response of an heterogeneous set of materials. A THz time domain spectrometer consists in an emitter device, a biased photoconductive antenna, which is made to emit THz radiation by the pumping action of an ultrafast laser, and a receiver made by a second photoconductive antenna activated by a delayed pulse of

the ultrafast laser.

The device developed during this thesis work is based on a pair of GaAs photoconductive antennas, which pumped by an ultrafast 800 nm Titanium:Sapphire ring laser allow for both generation and detection of the THz radiation. The time scan of the THz signal is provided by a mechanical delay line which permits to vary the delay of the pulse impinging on the receiver photoconductive antenna. The spectrometer under consideration is characterized by a bandwidth exceeding 3 THz in the absence of a sample, a sub-10 GHz spectral resolution, a maximum signal-to-noise ratio of 47.5 in the time domain and a dynamic range equal to 350,74 in the frequency domain. After the characterization of the reference signal, the device has been implemented for the study of the complex transmission function, refractive index and absorption coefficient of a series of materials of interest in THz spectroscopy.

This thesis is structured as following:

1. The first chapter provides a synoptic review of the most relevant sources of THz radiation, starting from novel technologies still subject to a considerable research effort, such as long wavelength quantum cascade lasers and fast electronic oscillators, to continue with more established techniques like non linear optical rectification. The working principle and main components of photoconductive antennas are eventually discussed in greater detail at the end of the chapter.

2. The second chapter deals with the theoretical foundations at the base of the solid state lasers used to pump photoconductive antennas, and is divided into two main sections. In the first one the principle of mode-locking is concisely presented, followed by the main techniques and components used to spur ultrafast pulses emission in a solid state laser. An overview of the most widespread active mediums for ultrafast lasers employed in THz-TDS is presented in the second section, encompassing the aforementioned Titanium:Sapphire, Ytterbium doped materials and the broad class of fiber lasers.

3. The experimental setup of the spectrometer is thoroughly analyzed in the third chapter. The ultrafast laser structure is initially presented in detail, starting with the pumping system and the the ring cavity design, to successively move to the characterization of the emitted ultrafast pulses. The main specifications of the photoconductive antennas implemented in the spectrometer are then discussed, such as electrodes geometry and operational parameters, as well as the alignment process necessary to couple the pump radiation into the active area of the photoantenna. The layout of the whole experimental setup and an overview of the most relevant measurement parameters are eventually provided.

4. The fourth chapter is entirely devoted to the discussion of experimental results. The THz signal is initially characterized in both time and frequency domain. The spectrometer is then employed to perform transmission measures on a set of materials of some spectroscopic interest such as plastic, paper, Gallium Phosphide and edible oils. Plastic and paper are commonly used in commercial packages, thus the understanding of their response to an incident THz field is essential in the applications of THz technology to non invasive monitoring of products. The correct measure of the refractive index of Gallium Phosphide

could help to optimize its implementation as an active material in optical rectification processes while the non invasive identification of food characteristics through THz spectroscopy is expected to play a major role in quality control processes in the years to come.

Chapter 1

Sources of Terahertz Radiation

1.1 The Terahertz radiation

Contrary to what one might think, Terahertz electromagnetic waves are not an exotic phenomenon. From cosmic background radiation to blackbody emission of room temperature objects, approximately 98% of total photons emitted in the history of the universe lie in the THz region of the electromagnetic spectrum [2]. This notwithstanding, there has been comparatively little work regarding science and applications of THz waves, at least until recent years. The reason for this paucity of results is simple; efficient generation of THz is a rather complicated problem.

THz radiation is located in the transitional region of the electromagnetic spectrum between the classically described electronics region (radio, microwaves and millimeter waves) and the photonic one (infrared, visible, UV, and X-ray), where the quantum nature of light becomes dominant. Approaching the THz regime from

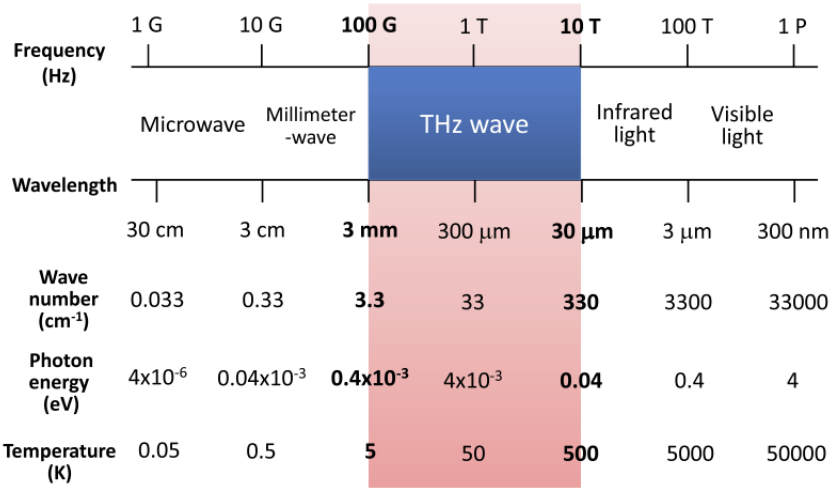

Figure 1.1: Representation of the electromagnetic spectrum with THz radiation shaded. The region between 3 mm and 30 µm has often been referred to as the "THz gap" [3]

either of these two regions presents unique challenges. Increasing the operating frequency of microwave electronic devices is limited by the intrinsic carrier mobility of

the oscillating semiconductor. On the other hand, reducing the energy of emitted photons generated by electron transitions in a semiconductor is inhibited by the fact that the energy of THz photons is lower than the thermal energy at room temperature. However, difficulties involved in the various methods of THz generation have not stopped the development of this technology and a number of novel sources have been proposed in the last decades.

In this chapter some of the most noteworthy sources of THz radiation are discussed, ranging from well established technology such as optical rectification and photoswitches to more recent devices such as tunneling THz oscillators and Quantum Cascade Lasers. Particular attention has been devoted at the end of the chapter to the analysis of photoconductive antennas, that are the components at the base of the spectrometer developed during this thesis work.

1.2 Quantum Cascade Lasers

In recent years, solid-state quantum-cascade lasers (QCLs) have been increasingly developed and seem to be a promising compact and high power ($\sim$ mW) technology for THz generation. The idea at the basis of QCLs is to exploit the intraband transition between two bound states of a potential well to obtain laser action, as already theoretically hypothesized in 1971 by Kazarinov and Suris [4]. The radiation frequency is determined by the energy spacing of the lasing sub-bands, which can be tuned in the engineering phase acting on the lattice parameters, allowing in principle operation at arbitrarily long wavelengths.

The first QCL, demonstrated in 1994 at Bell Laboratories, was based on a series of coupled quantum wells, showing an emission wavelength of $\lambda = 4.26$ μm and an output power exceeding eight milliwatts [5]. Further research brought to Terahertz emitting QCLs at cryogenic temperature in 2002 [6]. Up to present times,

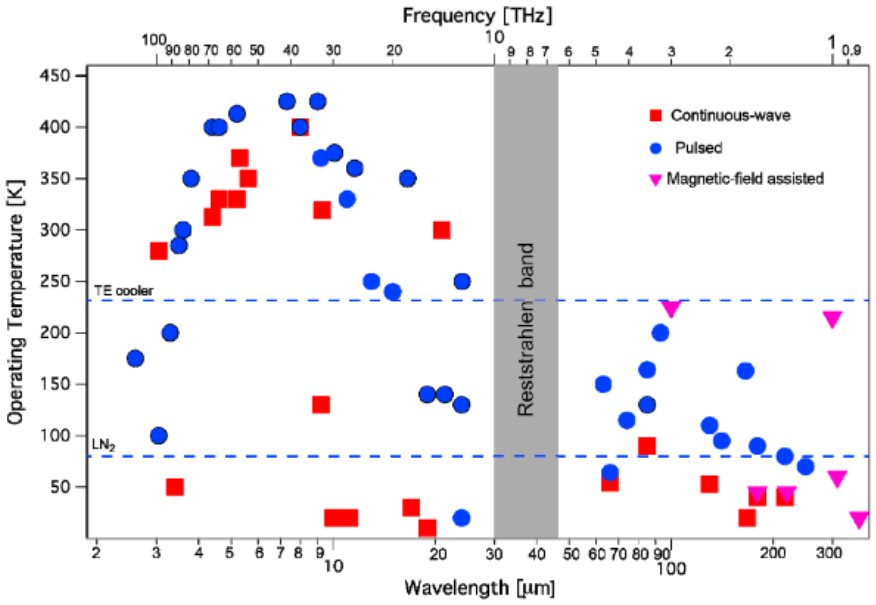

Figure 1.2: Operating temperature plot as a function of the emission wavelength (or frequency, top axis) for quantum cascade lasers [7]

THz-QCLs have achieved remarkable performances within the 1.2-4.9 THz range, providing output powers of some milliwatts, although Watt-level output has been demonstrated with large area devices, good tunability of the emission wavelength, a quantum limited linewidth and ps-pulse generation [7]. The success of THz-QCLs is mainly due to the availability of high output power, if compared to other common THz sources, and wavelength agility in a compact, potentially inexpensive and ready-to-use device. These characteristics have made THz-QCLs prime candidates for a wide range of applications, spacing from astronomy local oscillators, to the implementation in metrology and non-destructive imaging [8]. Nevertheless some open challenges still prevent THz-QCLs to be embraced in many THz technology applications. A major issue is linked with the work temperature of these devices which is close to 200K in pulsed mode and in the absence of any applied magnetic fields, as schematized in Figure 1.2. For more mainstream applications and lower costs of production, an operating temperature of at least 240K would be beneficial, in those conditions a simple Peltier cooling systems could be exploited. THz sources based on intracavity difference frequency generation in a mid-infrared emitting QCL have been studied as an alternative to realize room temperature devices [9]. In addition the generation of ultrashort-broadband pulses from QCLs has proved to be challenging. The shortest reported pulses are of the order of 10 ps. Perhaps the ultrafast electron dynamics of these devices could be the limiting factor for mode pulse formation but the exact mechanism for pulse generation is not fully understood yet [10].

Notwithstanding presently limitations, QCLs have the potential to become in the future one of the most diffused and high-performing THz sources. In the light of this, it is worth analysing the physics and the major technological aspects of such devices.

1.2.1 Physics of Quantum Cascade Lasers

In common bipolar semiconductor lasers, light emission is originated from the recombination of an electron in the conduction band and a hole in the valence band of the active material through an interband transition. Quantum Cascade Lasers are instead unipolar devices: they rely on a single type of carriers, the electrons, and the radiative recombination is due to an intraband transition that takes place between two bound states of a potential well in the conduction band.

The laser structure consists of several staked stages, each one composed by an electron injector and an active region, both based on a multiple quantum well structure. The number of injector-active region couples is not fixed a priori and is one of the engineering parameters of the device. A schematic representation of the conduction band profile for typical THz-QCLs is represented in Figure 1.3.

The name of the device derives from the fact that the electrons are subjected to a cascade process through the series of quantum wells: once an electron undergoes an intraband transition, with the emission of a photon, it is injected in the upper energy level of an adjacent well so that the emission process can be repeated. This process is also called electron recycling [11]. Therefore each electron can produce multiple photon emission as it travels along the laser structure. An electric field is applied across the device which produces the tilt of the conduction band. When the applied voltage exceeds a certain threshold value, the tilt allows for electrons to

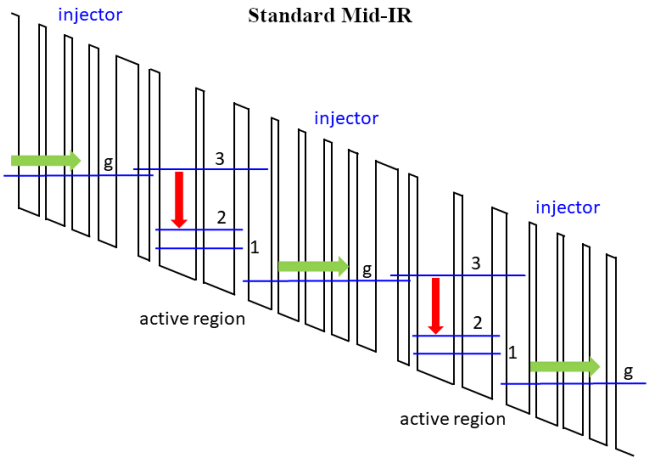

(a)

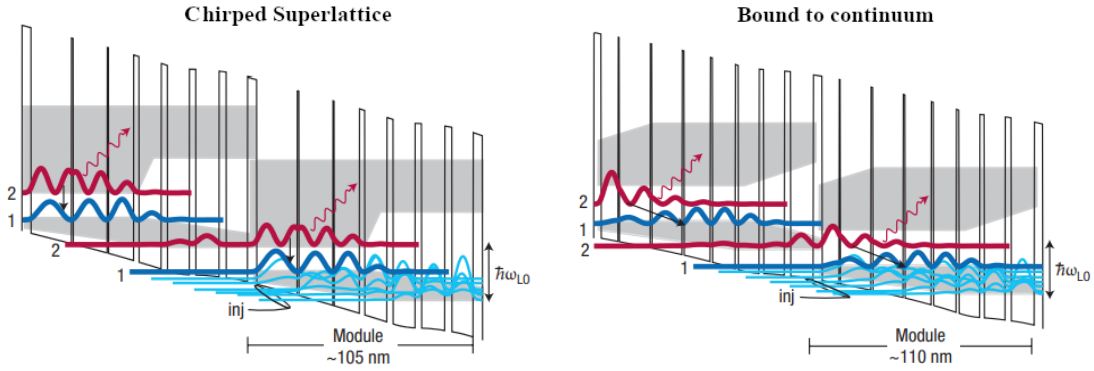

(b) (c)

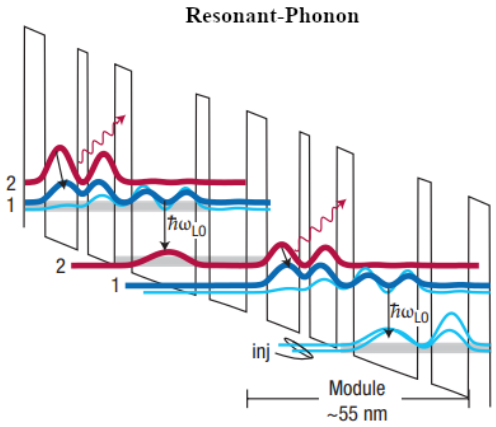

(d)

Figure 1.3: Section of conduction band structures for different types of QCLs: (a) mid-IR (*courtesy of Professor Mauro Nisoli* [11]) (b) Chirped SuperLattice (c) Bound To Continuum (d) Resonant Phonon. Minibands are shaded in gray, moduli squared of the wavefunction of each state are represented in THz structures. [12]

be injected into the upper laser level by resonant tunneling through the injection barrier.

The first and most well developed type of QCLs emit in the mid-IR region, at wavelengths shorter than the THz radiation. In mid-IR-QCLs (Figure 1.3a) population inversion is obtained thanks to the rapid resonant electron-phonon scattering of electrons from the lower laser state into the injector state with the emission of a Longitudinal-Optical (LO) phonon ($E_{LO} \sim 36$ meV). The lifetime of the upper level of the mid-IR laser is then usually significantly longer due to the larger energy separation between the two laser levels which is not resonant with LO-phonons energies. In order to prevent reverse tunneling from the upper laser level to states in the downstream adjacent injector, the injector structure is properly engineered so that a region with very low density of states, called minigap, is present at energies close to the upper radiative level.

In Thz-QCLs, achieving population inversion has proven to be considerably more challenging due to the small photon energies involved in the process. Because of the narrow energy spacing between the two laser states ($h\nu \sim 4 - 20$ meV), it is not trivial to use LO-phonon scattering to depopulate the lower radiative state without also depopulating the upper state.Three distinct active region designs have been developed to address this issue [12]: Chirped SuperLattice; Bound To Continuum; and Resonant Phonons.

Chirped SuperLattice (CSL) was the first structure to be suggested [6]. It is based on the coupling of several GaAs/AlGaAs quantum wells in a superlattice to create minibands of states. Laser radiation is originated from the transition between the lowest state of the upper miniband to the higher state of the lower miniband, as illustrated in Figure 1.3b. Scattering of electrons between the tightly coupled states within the miniband is favoured over inter-miniband scattering, thus allowing for population inversion to be established.

The Bound To Continuum (BTC) design is essentially an evolution of the CSL in which the upper radiative state is a defect state in the minigap, as can be seen in Figure 1.3c. In this situation depopulation processes of the lower level follow the same dynamic of CSL but the lifetime of the upper state is sensibly longer as non radiative scattering from this level is reduced.

In the Resonant Phonons (RP) structure, Figure 1.3d, the lattice is designed so that the lower radiative state is in a broad tunnelling resonance with the excited state in the adjacent quantum wells, so that its wavefunction is spread over several quantum wells. As a result, electrons in the lower radiative state in the active region are rapidly extracted by resonant quantum tunneling and successively relax to lower states in the injector region with the emission of a LO-phonon. The upper radiative state instead is more localized in the active region and has little overlap with the injector states, thus preventing depopulation of the upper level.

THz-QCLs need constant cooling in order to operate properly. Population inversion, and thus laser's gain, is heavily degraded at higher temperatures by means of thermal backfilling of the lower laser level and depopulation of the upper radiation level by thermally activated Phonon scattering. Backfilling from the densely populated injector state can happen either because of thermal excitation or reabsorbtion of non equilibrium LO-phonons. Thermal activated phonon scattering instead takes place when electron in the upper band acquire enough kinetic energy to emit a LO-phonon and relax in the lower subband.

Absorption by free carriers is particularly strong in the THz region, as the absorption coefficient increases proportionally to the square of the radiation wavelength. Therefore in waveguides for THz-QCLs it is of fundamental importance to minimize the overlap of the laser mode with any doped cladding layer, in order to minimize losses and obtain laser action.

A first solution exploits the guiding effect of a surface plasmon mode to achieve tight confinement of the radiation. In the so called Semi Insulating-Surface Plasmon (SI-SP) waveguide, a thin heavily doped layer is grown between the active region, on the other side of which there's a metal contact, and a semi-insulating Ga-As substrate, see Figure 1.4a. The real part of the dielectric constant of the thin layer can be made negative by appropriate doping density tuning. These conditions result in a surface plasmon mode, bounded between the top metal contact and the heavily doped layer. Although the mode extends substantially into the substrate, absorption losses take place only in the thin heavily doped region and are therefore minimized.

The other widely adopted solution is the so called Metal-Metal (MM) waveguide. It uses metal layers, which are placed immediately above and below the active region, so to obtain an almost completely confined mode, see Figure 1.4b. Being the doped contact layers generally thin, waveguide losses are dominated by absorption in the metal and re-absorption from inside the active region itself. In general MM allow for higher temperature operation and lower emission frequencies, but with a lower output power and poorer quality beam profile than SI-SP waveguides.

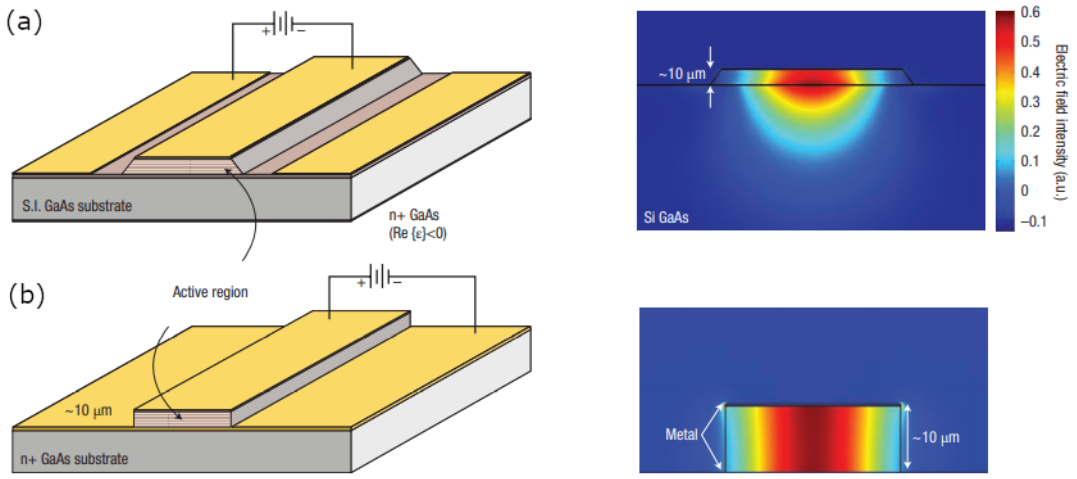

Figure 1.4: Schematic diagram (left) and typical two-dimensional mode intensity pattern (right) for SI-SP (a) and MM (b) Terahertz Quantum Cascade Laser waveguides. [12]

1.3 Electronic oscillators

The most widespread source for sub-Terahertz frequencies of the electromagnetic spectrum is the electronic oscillator. This device converts a DC supply current in an AC output signal with a stable frequency and amplitude. Oscillators are ubiquitous in modern electronics, being employed from the generation of clock frequencies for electronic devices to signal broadcast by television and radio transmitters.

Feedback oscillators are among the most common type of linear oscillator. Although many different specific circuit designs have been developed, all the feedback oscillators are essentially composed of an electronic amplification stage, such as a transistor or an operational amplifier, connected in a positive feedback loop with a frequency selective circuit (see Figure 1.5a). The frequency selective stage can be based on different kinds of filters such as inductance-capacitance (LC) or resistance-capacitance (RC) circuits and crystal resonators. The oscillating signal is obtained through the filtering and amplification of the initial noise in the circuit. The initially white noise travels around the loop, being filtered and amplified, until it converges on a sine wave at the circuit's resonant frequency.

Oscillators applications based on transistor technology are well established and represent the standard source of electromagnetic waves in the sub-terahertz region. However, transistors present some intrinsic limitations in high speed operation, mainly due to a limited carrier mobility. The flow of charge carriers between different regions of the transistor takes some time, making the response of the component to changes in input voltages and currents not instantaneous. This not negligible transit time all along with parasitic RC effects [13], limits the maximum operational frequency of such devices to few hundreds of GHz. See table 1.1 for a panoramic of the maximum operational frequency electronic components used in oscillators circuits.

Table 1.1: Active devices with approximate maximum frequency of oscillation [14]

Device	***Operational frequency***
Triode vacuum tube	∼1 GHz
Bipolar transistor (BJT)	∼20 GHz
Heterojunction bipolar transistor (HBT)	∼50 GHz
Metal–semiconductor field-effect transistor (MESFET)	∼100 GHz
High electron mobility transistor (HEMT)	∼200 GHz
Resonant Tunneling Diode (RTD)	∼1 THz

The research to extend the operational bandwidth of these devices to the THz regime is strictly linked with the development of faster electronic components. In order to obtain terahertz oscillators, the amplification stage based on transistor technology has to be replaced by components relying on a faster charge transfer mechanism while still capable of compensating for the losses of the resonator.

In fast oscillators the amplification stage can be replaced by a Negative differential Resistance device i.e. a device which shows a negative slope of the I-V characteristic for certain values of voltage applied. In the oscillator the negative resistance of the active device balances with the positive internal loss resistance of the resonator creating a resonator with no damping, which generates spontaneous continuous oscillations.

Among these negative differential resistance components, the Resonant Tunneling Diode (RTD) is particularly well suited as active device for Terahertz oscillators because of its fast charge transfer mechanism relying on quantum tunneling effect. Although oscillators based on this technology are still at an early phase of development, oscillations up to the Terahertz regime ($\sim 1 - 2$ THz) have been observed

by different research groups and further increments in the maximum oscillation frequency are believed to be expected in years to come [15–17].

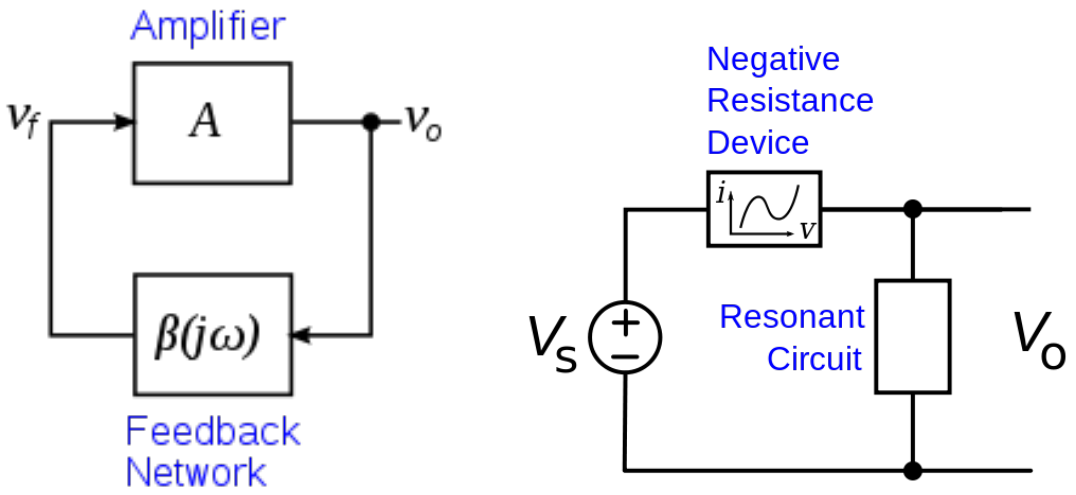

(a) (b)

Figure 1.5: Comparative view of (a) Bloch scheme of a feedback oscillator and (b) Scheme of a Negative Resistance Oscillator. Note the two points of inflexion in the I-V characteristic which make negative resistance devices well suited to emulate the working logic of transistors in many applications.

In the next section the key components and charge transfer mechanism at the base of the operation of Resonant Tunneling Diodes are briefly addressed.

1.3.1 Resonant tunneling diode oscillators

A Resonant Tunneling Diode consists of two identically heavily doped, narrow energy-gap materials encompassing an emitter region; a quantum well in between two barriers of large band gap material; and a collector region (see Figure 1.6).

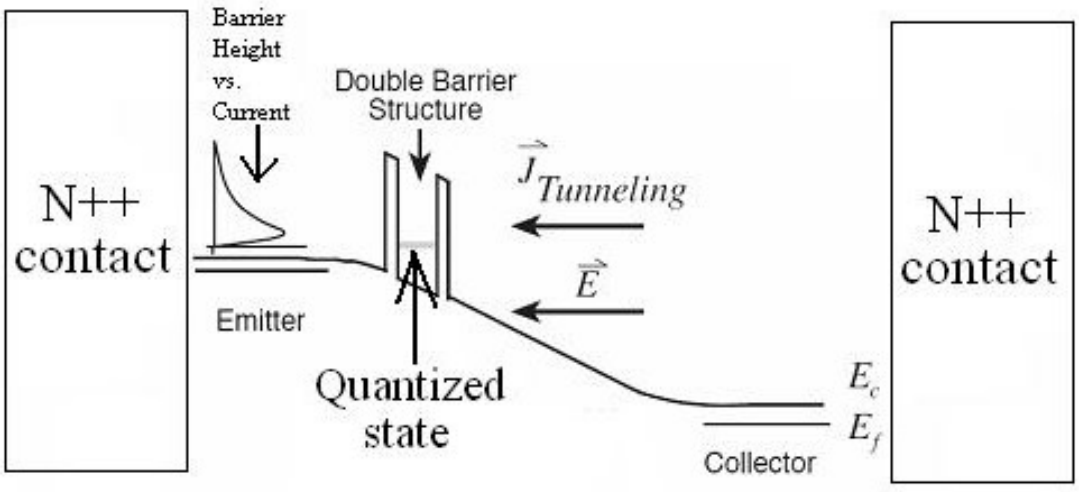

Figure 1.6: Schematic diagram of a RTD [18]

Resonant tunneling diodes conduct current only under a specific range of applied external bias voltage. In this regard RTDs are quite similar to CMOS transistors since conduction of current in both components can be turned on and off at will. However the charge transfer mechanism of RTD is completely different from the one of transistors, being the former based on resonant tunneling of electrons through quasi-bound states within a quantum well structure.

In order to understand the working principle of a RTD suppose for the sake of simplicity that the quantum well has a single quasi-bound state as in Figure 1.7. When no forward voltage bias is applied to the active device(1.7a), most of the electrons in the emitter have an energy well below the confined state between the potential barriers. In this condition no resonant tunneling can take place and the RTD acts as an open circuit.

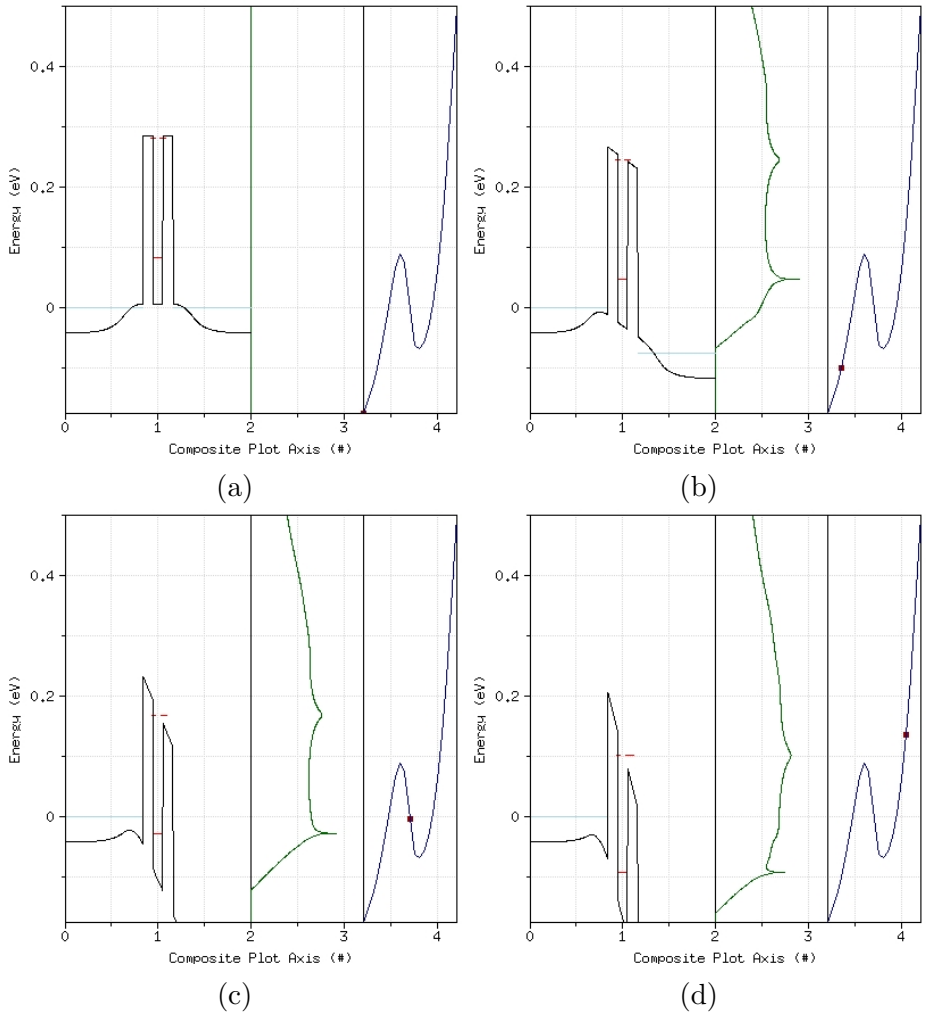

Figure 1.7: Band structure (left), Current Density (center) and I-V characteristic (right) of a RTD for increasing values of voltage applied, starting from unbiased condition. (Image generated with RTD-NEGF on NANOHUB.org)

When an increasing forward voltage bias is applied (1.7b), the Fermi level of the emitter starts getting closer to the resonant confined states of the quantum well. The quasi-bound energy state allows electrons in the emitter with a similar energy to tunnel through the well creating a current. Eventually a local maximum in current occurs when the resonance level in the quantum well is close to the conduction band

edge of the emitter.

As the applied voltage continues to increase (1.7c), more and more electrons gain too much energy to tunnel through the well as the confined state falls in the energy bandgap of the emitter. In this way as the voltage increases the current is gradually decreased so that the current-voltage curve exhibits a negative differential conductance region. This is the region utilized by the oscillator under operating conditions.

Beyond a certain voltage 1.7d), current begins to rise again because of substantial thermionic emission where the electrons can tunnel through the non-resonant energy levels of the well. This process produces a local minimum of current.

Because quantum tunneling is inherently a very fast phenomenon that is not transit-time limited, the resonant-tunneling diode is considered among the fastest electronic devices ever made. RTDs can also work up to room temperature which is a characteristic of not so many THz sources. On the other hand, it is more difficult to supply high current to resonant-tunneling diodes, thus the oscillator's output power is limited with respect to other THz generation devices.

RTD bandwidths were reported for InAs/AlSb RTDs at about 1.24 THz due to their low ohmic contact resistance and short transit times [18]. Higher bandwidths may be obtained using different contact materials with higher tunneling current densities and shorter transit times. However, in many applications InGaAs/AlAs/InP preferred to InAs/AlSb because of well established fabrication and growth technologies. In order to obtain highest possible peak currents the thickness of the quantum well can be decreased and the emitter doping level increased. However both of these methods will degrade Peak-Valley Ratio (PVR), i.e. the ratio between local maxima and minima in the current value, increasing the valley current. This increment in the valley current entails an higher power consumption due to increased leakage current so that in the end the valley current limits the minimum barrier thickness and maximum emitter doping levels.

1.4 Optical rectification

Since the dawn of laser technology and especially parallel to the development of ultrashort pulse lasers, nonlinear optical processes have been increasingly studied and exploited in a wide range of applications, among which Terahertz generation. Nonlinear effects arise due to optical excitation of a polarizable medium and their magnitude is strongly dependent on the power of the incident radiation.

In scalar approximation, assuming to have no free charges and free currents in the media, the propagation equation for the electric field can be written in the well know form:

$$\nabla^2 E - \frac{1}{c^2}\frac{\partial^2 E}{\partial t^2} = \mu_0 \frac{\partial^2 P}{\partial t^2} \tag{1.1}$$

In which the second derivative of the polarization P acts as a source term for the far field.

The polarization itself is a function of the electric field through the susceptibility tensor and can generally be expanded into a power series of E:

$$\begin{aligned} P(r,t) = \epsilon_0[\chi^{(1)}(r,t)E(r,t) + \chi^{(2)}(r,t)E(r,t)E(r,t) + \\ \chi^{(3)}(r,t)E(r,t)E(r,t)E(r,t) + ...] \end{aligned} \tag{1.2}$$

where $\chi^{(n)}(r,t)$ is the n^{th}-order nonlinear susceptibility tensor that is determined by the crystal structure.

The second term of the Equation 1.2 is the one responsible for second order nonlinear effects, such as: second harmonic generation(SHG); sum frequency generation (SFG); difference frequency generation (DFG); and optical rectification (OR). Optical rectification is basically a difference-frequency generation with a frequency difference close to zero. It could be worth noting that $\chi^{(2)}$ is null in all centro-symmetric materials, in which case no second order nonlinear effect can be observed.

Considering the incident light as a plane wave, then field can be expressed as:

$$E(t) = \int_0^\infty E(\omega)e^{-i\omega t}d\omega + c.c. \tag{1.3}$$

The optical rectification component of the polarization is then obtained by substituting Equation 1.2 into Equation 1.3:

$$\begin{aligned} P_{NL}^{(2)} &= 2\epsilon_0\chi^{(2)} \int_0^\infty \int_0^\infty E(\omega_1)E^*(\omega_2)e^{-i(\omega_1-\omega_2)t}d\omega_1 d\omega_2 \\ &= 2\epsilon_0\chi^{(2)} \int_0^\infty \int_0^\infty E(\omega+\Omega)E^*(\omega)e^{-i\Omega t}d\Omega d\omega \end{aligned} \tag{1.4}$$

where Ω is the frequency difference of two optical frequency components of the electric field.

As can be evinced from Equation 1.1, in the far field, the radiated electric field $E_r(t)$ is depends on the second time derivative of $P_{NL}^{(2)}(t)$:

$$E_r(t) \propto \frac{\partial^2}{\partial^2 t} P_{NL}^{(2)}(t) \tag{1.5}$$

Given active crystal structure and shape of the incident light, the far-field waveform of the non linear radiation can be calculated through Equation 1.5.

Typically, femtosecond laser pulses are used to generate THz radiation through second order non linear effects in Electro-Optic (EO) crystals. Due to the extremely short duration, the bandwidth of femtosecond pulses is fairly broad. Assuming for instance a transform limited gaussian pulse with a duration $\Delta\tau = 50$ fs, the spectral bandwidth span of the pulse will be:

$$\Delta\nu = \frac{TBP_{Gaussian}}{\Delta\tau} \approx 8.8THz \tag{1.6}$$

Where $TBP_{Gaussian} \sim 0.441$ is the Time-Bandwidth Product for a gaussian shaped pulse.

Any two slightly different frequency components of the spectrum can interact to contribute to the difference frequency generation. The overall resulting THz pulse is the weighted sum of all these contributions and is generally characterized by an extremely broad spectral bandwidth itself, which is a key advantage of generating Terahertz radiation through optical rectification. In general a single femtosecond pulse is enough to stimulate optical rectification radiation by self-interaction.

A fundamental role in nonlinear generation is played by the electro-optic crystal. Many factors, such as materials, crystal orientation, thickness, absorption and dispersion, diffraction, phase matching, and saturation, affect the radiation efficiency,

waveform, and frequency distribution of the transmitted radiation. Among all these factors, Phase matching has the strongest impact on generation efficiency for a nonlinear process such as optical rectification.

Phase matching condition can be expressed as:

$$\begin{cases} \omega_{01} - \omega_{02} = \Omega_{THz} \\ k_{01} - k_{02} = k_{THz} \end{cases} \tag{1.7}$$

where ω_{01}, ω_{02} and k_{01}, k_{02} are, respectively, frequencies and wave vectors of optical waves involved in THz wave generation while Ω_{THz} and k_{THz} are the frequency and wavelength of the generated THz wave. The first condition of 1.7 takes into account conservation of energy while the second equation is, in general, a vectorial one and considers conservation of momentum in the nonlinear process.

When phase matching condition is satisfied, the newly generated THz frequency is in every point in phase with the one generated through the propagation along previous sections of the crystal. This positive interference process leads to maximum energy conversion coefficient along the light propagation direction.

Considering that THz frequency is much lower than optical ones, Equations 1.7 can be simplified through dividing the first equation by the second one:

$$\frac{\partial \omega_0}{\partial k_0} = \frac{\Omega_{THz}}{k_{THz}} \tag{1.8}$$

According the to the definitions of group and phase velocities of a wave packet, Equation 1.8 gives:

$$v_{G,0} = v_{Ph,THz} \tag{1.9}$$

The equality in 1.9 means that the phase matching condition is satisfied when the group velocity of the optical beam is equal to the phase velocity of the THz beam. Since the optical pulse has a much higher oscillation frequency than the THz one, the THz pulse only sees the profile of the optical pulse rather than the individual oscillations. To have the maximum energy conversion, the optical pulse should be locked in a constant temporal delay with respect to the THz pulse along the entire interaction length.

In the case in which phase matching condition is not satisfied, a phase mismatch leads to a phase walk off during propagation. In this case the frequency generated through nonlinear frequency mixing achieves generally lower intensities and shows a periodic behaviour with respect to the interaction length.

Starting from the coupled equations of the three waves involved in the process it is possible to define the coherence length L_c, i.e. the interaction length at which the phase change reaches π and the intensity of difference frequency generated signal is at its maximum:

$$L_c = \frac{\pi}{k_{01} - k_{02} - k_{THz}} = \frac{\pi}{\delta k} \tag{1.10}$$

When it's not possible to satisfy the phase matching condition, in order to efficiently generate THz from a bulk nonlinear crystal, the thickness of crystal along the propagation direction should be selected close to the coherence length in order to avoid conversion cancellation due to phase mismatch.

When the phase matching condition is achieved the coherence length will ideally diverge, neglecting pump depletion, along the propagation direction. The two situations are illustrated in Figure 1.8.

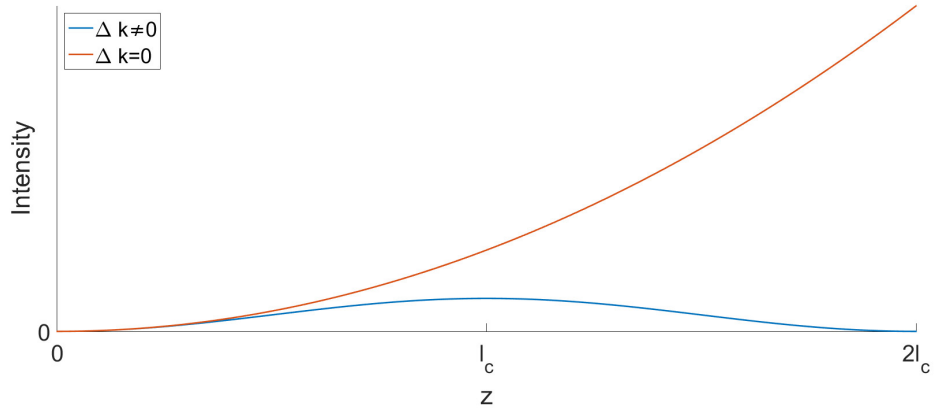

Figure 1.8: Terahertz frequency generation intensity in the ideal case of no pump depletion with and without phase matching. [19]

1.4.1 Methods for phase matching

Depending on the incident radiation and properties of the nonlinear material, the optical rectification process can happen under different conditions: If the photon energy of the incident radiation is larger than the band gap of the crystal, the whole optical beam will be absorbed within a fairly short distance. In this case phase matching is generally not very important, being the range of interaction much shorter than the coherence length. On the contrary, when the photon energy is lower than the band gap of the nonlinear material, the excitation beam can propagate for longer distances through the nonlinear crystal.

On top of these two cases the effect of different phase matching conditions must be taken into account. If phase matching is satisfied in optical rectification and the incident radiation is free to propagate along the entire crystal with negligible absorption losses, the generated THz field will continuously increase along the entire depth of the nonlinear crystal. Therefore, a high throughput for the Terahertz generated field is expected. On the other hand, if phase matching is not satisfied, generated THz waves will be periodically canceled after each coherence length and the generated Terahertz intensity will be low.

The most straightforward experimental configuration to achieve phase matching is the collinear one. Here phase matching occurs with the excitation and Terahertz beam propagating along the same direction in the nonlinear crystal. The phase matching is entirely dependent on the behaviour of the refractive index of the active crystal. Collinear phase matching not only gives a high generation coefficient due to long interaction length, but also generates THz radiation with very good beam quality.

Three are the major factors that need to be taken into account in the selection of a nonlinear crystal for Terahertz generation: Strength of the second order nonlinear optical susceptibility, absorption characteristic in both optic and THz regions of the spectrum and coherence length of the optical rectification process.

In practical applications, ZnTe crystal is one of the most common choices for nonlinear Terahertz generation in collinear phase matching configuration [20]. When a ZnTe crystal is excited by fs laser pulses with central wavelength around 800 nm ultrashort THz pulses are generated along the optical propagation axis. The main

advantage of collinear generation lies in its relatively simple experimental setup. However for pump pulses with high peak intensity, saturation effects mainly due to free carriers generated by two or higher order photon absorption limit the conversion efficiency. Multi-photon absorption not only depletes the pump pulse but also leads to a reshaping of the rectified waveform due to the influence of the photoinduced free carriers on the complex refractive index of the crystal [21–24]. An alternative method to achieve phase matching relies on the birefringece properties of some non linear crystals. In a birifrengent material, light polarized along different axis experiences different refractive indexes during propagation. By selecting the polarization of the optical and THz beams along different directions of the ellipsoid of the refractive index, phase matching can be satisfied. GaSe is often employed in this configuration due to its pronounced birefringence.

Other nonlinear crystals, such as LiNbO3, have promising properties for Terahertz generation but do not have sufficient birefringence to match the index of the optical wave with the low frequency components of the THz wave in a collinear configuration. In these cases, phase matching can be achieved by allowing the optical and THz beams to propagate in different directions. Controlling the tilting angle γ between optical and terahertz propagation directions the phase matching condition can be satisfied:

$$v_{G,O} \cos\gamma = v_{Ph,THz} \tag{1.11}$$

Although the propagation direction of THz and optical wave are different, the tilted intensity front of the pump pulses travels collinearly with THz wave with same speed. As a result, both phase and velocity matching are satisfied. A schematic representation of the experimental setup is showed in Figure 1.9

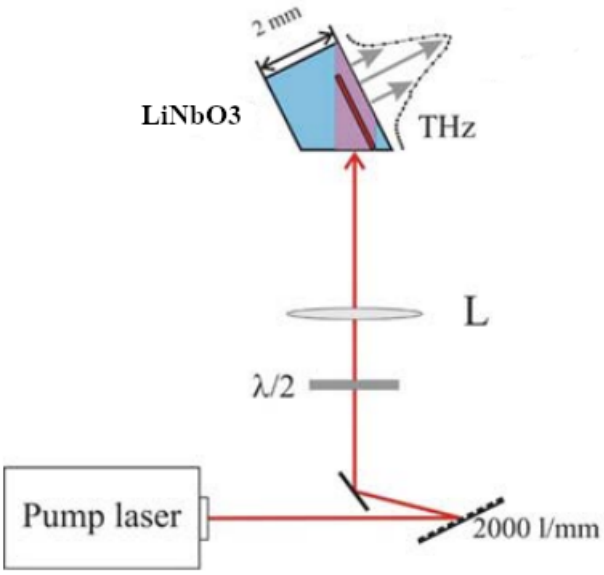

Figure 1.9: Tilted pulse front excitation scheme using a grating to tilt the pulse front and a lens to image it onto the generation crystal [25]

However, the non collinear configuration has some criticalities. The first one is that THz wave and excitation beam are overlapped for a short distance due to the different propagation direction which affects the energy conversion coefficient. The second issue is also related to the large tilt angle and regards the high internal reflectivity at the output surface of the crystal.

LiNbO3 has been widely used in non collinear configuration due to its high nonlinearity and its larger band gap with respect to other commonly used crystals such as ZnTe. The larger bandgap makes the material less susceptible to multiphoton absorption thus increasing the pumping saturation threshold. The larger pump power and the high nonlinearity allow LiNbO3 configurations to deliver stronger Terahertz radiation despite of the limits of the non collinear geometry [26]. The main drawback of LiNbO3 crystal lies in its higher absorption coefficient that severely limits the maximum crystal thickness.

1.5 Photoconductive Antennas

Photoconductive switches were among the first devices to be exploited for THz generation, with the accomplishment of subpicosecond electrical pulses back in the 1980s [1, 27]. During the last decades, Photoconductive Antennas (PCAs), based on a photoconductive switch integrated into an antenna structure, have evolved to become one of the most reliable and utilized components in generation as well as detection of broadband THz radiation.

The general structure of a PCA consists of two metal electrodes coated on a photoconductive semiconductor substrate. To generate a THz pulse, a bias voltage is applied to the electrodes and an incident optical pulse is focused in the gap between the two, as shown in Figure 1.10 for a 1 ps incident optical pulse. It is worth noting

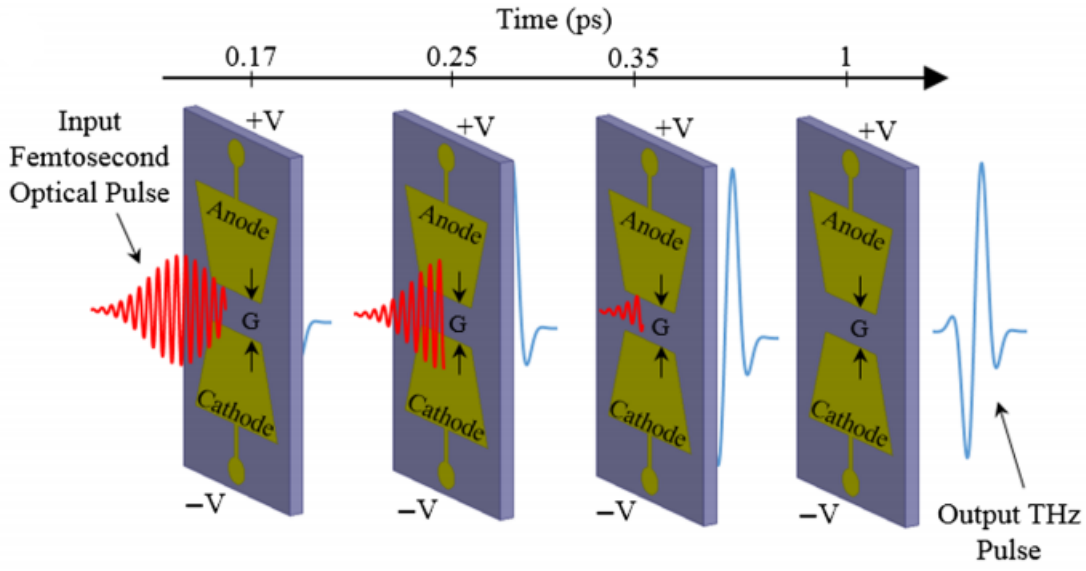

Figure 1.10: Simplified representation of the generation process of a THz pulse in a Photoantenna for a 1 ps incident optical pulse. The optical pulse is focused onto the gap (G) in between the two biased electrodes. The polarization of the outward THz pulse is aligned along the direction of the bias field. [28]

that the optical pulse must have a photon energy larger than the band gap of the substrate in order to properly generate photoinduced free carriers. This is one of the main aspects to consider when choosing the wavelength of the optical pump. As the pulse propagates through the semiconductor, its absorption is responsible for the generation of photocarriers that are accelerated by the bias field producing a transient photocurrent. This photocurrent drives the emission of the THz pulse. A temporal breakdown of the process is represented in Figure 1.11.

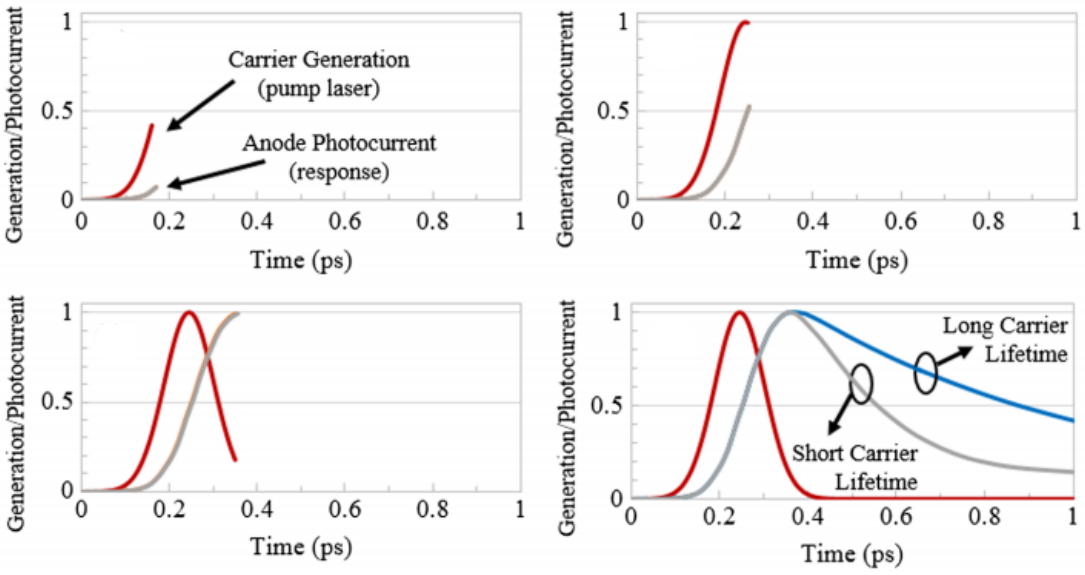

Figure 1.11: Evolution of the time profile of the optical pulse (red trace) and photocurrent in the photoconductive substrate in the case of short-carrier lifetime (grey trace) and long carrier lifetime (blue trace). [28]

As the optical pulse is absorbed, carriers in the photoconductor are generated at a rate proportional to the incident intensity. The photocarriers undergo an acceleration along the bias field direction, thus generating a transient photocurrent with a rise time approximately proportional to the one of the incident optical pulse. The photocurrent will eventually reach a peak and start to decrease, with a decay time dictated by the intrinsic properties of the photoconductive substrate rather than the temporal profile of the optical pulse.

In photoconductors with a short carrier lifetime, the photocarriers generated by the optical pulse will begin to recombine shortly after the full absorption of the optical pulse resulting in a short duration, broadband output pulse. On the contrary, a long carrier lifetime will result in a slower recombination process thus broadening the THz pulse and shrinking its overall bandwidth. To prevent this last scenario, substrates featuring subpicosecond carrier lifetime have been selected, with low temperature grown gallium arsenide (LT-GaAs) being the most common.

Although the exact mechanism of THz generation in PCAs is still subject to discussion, three are the main modalities in which the phenomena can be explained [28]: the radiation from transient acceleration and separation of carriers in the bulk semiconductor; the instantaneous drop in antenna gap resistivity after optical excitation due to the rise in carrier concentration and the direct collection, in proximity of the antenna electrodes, of photocarriers that act as a driving current producing

THz oscillations.

In the following section a theoretical model accounting for emission of THz radiation in a PCA is discussed. At first the case of weak optical excitation is considered, in which the power of THz pulses increases linearly with the bias field and optical excitation. The situation of intense optical excitation is considered thereafter. In this scenario the space charge effects play an important role in screening the bias electric field and bring to the saturation of the emitted THz power.

1.5.1 Physical model

The dependence of the radiated electric field on the induced surface photocurrent in the photoconductor can be directly derived from Maxwell's equations. In the Coulomb gauge, the radiated field E_{THz} as a function of time t at a displacement r from the antenna center is given by [29]:

$$E_{THz}(z,t) = \frac{A}{4\pi\epsilon_0 c^2 z}\frac{\partial}{\partial t}\int \frac{J_s\left(r', t - \frac{|r-r'|}{c}\right)}{|r-r'|}da' \tag{1.12}$$

Where ϵ_0 is the permittivity of free space, c is the speed of light in vacuum, $J_s()$ is the surface current in the photoconductor, A is the area of the gap under illumination, da' is the increment of surface area at displacement r' from the center of the antenna and the integration is taken over the surface of the illuminated region of the PCA.

Considering far field ($|r - r'| \approx r$) and on axis detection ($x = y = 0$), equation 1.12 can be simplified to:

$$E_{THz}(z,t) = \frac{A}{4\pi\epsilon_0 c^2 z}\frac{\partial J(t)}{\partial t} \tag{1.13}$$

With $t \to t - \frac{z}{c}$ as the new time coordinate.

In case of weak optical excitation and low bias field, space charge effects can be neglected and induced photocarriers are driven solely by the bias electric field, E_{bias}, so that the surface photocurrent is simply expressed as:

$$J(t) = n(t)\mu_e e E_{bias} \tag{1.14}$$

Where $n(t)$ is the density of photocarriers and μ_e is the electron mobility. For the sake of simplicity the contribution of holes has not been considered, owing to the lower carrier mobility.

Time evolution of Photocarrier density is mainly influenced by the generation rate from the optical excitation and the trapping of free carriers due to recombination in the semiconductor [30, 31]:

$$\frac{dn(t)}{dt} = -\frac{n(t)}{\tau_c} + \frac{\eta I_{opt}(t)}{h\nu} \tag{1.15}$$

Where τ_c is the trapping time of free carriers in the semiconductor, η is the external quantum efficiency, I_{opt} is the intensity of the optical pulse and $h\nu$ is the energy of the excitation photon.

For a constant bias field, equations 1.13, 1.14 and 1.15 give:

$$E_{THz}(z,t) = \frac{Ae}{4\pi\epsilon_0 c^2 z}\left(-\frac{n(t)}{\tau_c} + \frac{\eta I_{opt}(t)}{h\nu}\right)\mu_e E_{bias} \tag{1.16}$$

Under weak excitation the radiated THz field is proportional both to the bias field and the optical excitation. The excitation pulse acts as a trigger to release stored energy in the gap of the PCA; the higher the excitation power, the more photocarriers will be generated and accelerated through the bias field resulting in a stronger THz pulse. The effect of the bias field in turn is to increase the acceleration of photocarriers along the axis between the two electrodes, thus increasing the surface current density and the emitted THz power. It's worth noting that both the applied bias field and the optical power cannot be increased over a certain threshold without causing dielectric breakdown in the substrate.

Actually, linear relationships between the biased field and THz field, as well as between the excitation pulse energy and THz field, is only verified under weak excitation and low bias field. For higher optical excitation powers, the optical concentration of photocarriers increases, the substrate of the PCA starts to resemble more to a conductive medium than a semi-insulating material and space charge effects can no longer be neglected. The high concentration of free carriers in the antenna gap generates space-charge fields that screen the effect of the external bias field. This effect can bring to the saturation of the emission of THz radiation from the PCA for intense optical excitation.

In the situation of strong optical pump, the effect of the space-charge generated field on the free carriers themselves has to be taken into account, thus equation 1.14 becomes:

$$J(t) = \sigma_s(t)(E_{bias} + E_{in}) \tag{1.17}$$

Where E_{in} is the field generated by the photocarriers inside the semiconductor and $\sigma_s(t)$ is the surface conductivity of the emitting antenna, which can also be expressed as a function of the optical intensity impinging on the photoantenna:

$$\sigma(t) = \frac{e\mu(1-R)}{h\nu} \int I_{opt}(t')e^{-\frac{t-t'}{\tau}}dt' \tag{1.18}$$

With I_{opt} being the intensity of the incident optical radiation, R the reflectivity of the illuminated area of the photoantenna and τ the lifetime of the excited photocarriers.

The internal field can then be written as [32]:

$$E_{in}(t) = -E_{bias}\frac{\sigma_s(t)\eta_0}{\sigma_s(t)\eta_0 + (1+n)} \tag{1.19}$$

Where n is the refractive index of the photoconductor and η_0 is the impedance of air, $\eta_0 = 377\ \Omega$. As equation 1.19 clearly shows, for a sufficiently large optical pulse, the conductivity of the photoconductor can increase to such an extent that the space charge field approaches the bias one and the screening can be total. In this situation the velocity of free charges will rapidly randomize owning to collisions and the photocurrent's value plummets.

The new relation for the surface photocurrent can be obtained combining equations 1.17 and 1.19:

$$J(t) = \frac{\sigma(t)E_b}{\frac{\sigma(t)\eta_0}{1+n} + 1} \tag{1.20}$$

Defining the conductivity threshold: $\sigma_d = \frac{1+n}{\eta_0}$, the radiated THz field is proportional

to:

$$E_{THz}(z,t) \propto \frac{E_{bias}}{\left[1+\frac{\sigma(t)}{\sigma_d}\right]^2}\frac{d\sigma(t)}{dt} \tag{1.21}$$

Considering equation 1.18 and assuming the case of an ultrafast optical pulse, which is true in most of the experimental applications, the surface conductivity can be considered proportional to the peak intensity of the optical radiation, $\sigma_s(t) \propto I_0$. In these conditions the emitted field from the photoantenna is proportional to:

$$E_{THz}(z,t) \propto \frac{I_0}{(1+kI_0)^2} \tag{1.22}$$

Having defined $k = k(t)\frac{\eta_0}{1+n}$, where $k(t)$ denotes the ratio between $\sigma_s(t)$ and I_0. The above equation shows that when the excitation laser is strong enough, the impedance of the substrate becomes comparable to the air, and the THz field becomes saturating to the excitation laser power.

1.5.2 Continuous wave generation

Up to this point, PCAs have been presented as sources for the generation of ultrashort broadband THz pulses. However the same device can also be used to generate continuous waves of THz frequency.

For this purpose the optical excitation pulse is replaced by two CW laser beams focused on the same spot in the gap of the antenna, with a beat frequency lying in the THz region, as represented in Figure 1.12. The process of THz heterodyne generation is similar to the one discussed for the pulsed regime: the oscillating excitation intensity at the overlapped spot modulates the generation of photocarriers in the surface layer of the semiconductor, thus inducing CW oscillations of the photocurrent which result in the emission of the electromagnetic wave. Since the photoantenna acts as a frequency mixer for the two optical frequencies, Such devices for photoconductive CW THz generation are usually referred to as *Photomixers*.

Considering I_1 and ν_1 respectively the optical intensity and the frequency of the first impinging beam and I_2, ν_2 the intensity and frequency of the second beam, the overall surface intensity on the antenna gap can be described as:

$$I_{opt}(t) = I_1 + I_2 + 2\sqrt{I_1 I_2}\left[\cos(2\pi(\nu_2-\nu_1)t) + \cos(2\pi(\nu_1+\nu_2)t)\right] \tag{1.23}$$

The component oscillating at the sum of frequencies is significantly faster than the carrier effective recombination time τ_c, hence it's effect on the photocurrent is not noticeable. The carrier density evolution is described by equation 1.15. Substituting the explicit form for the intensity of the optical excitation, the carrier density as a function of time proves to be [33]:

$$n(t) = \frac{\eta\tau_c}{h\nu}\left(I_1 + I_2 + \frac{2\sqrt{I_1 I_2}\sin(\omega_{21}t+\phi)}{\sqrt{1+\omega_{21}^2\tau_c^2}}\right) \tag{1.24}$$

Where $\omega_{21} = 2\pi(\nu_2-\nu_1)$ is the THz frequency and $\phi = \tan^{-1}(\frac{1}{\omega_{21}\tau})$ is the phase term due to the finite carriers lifetime.

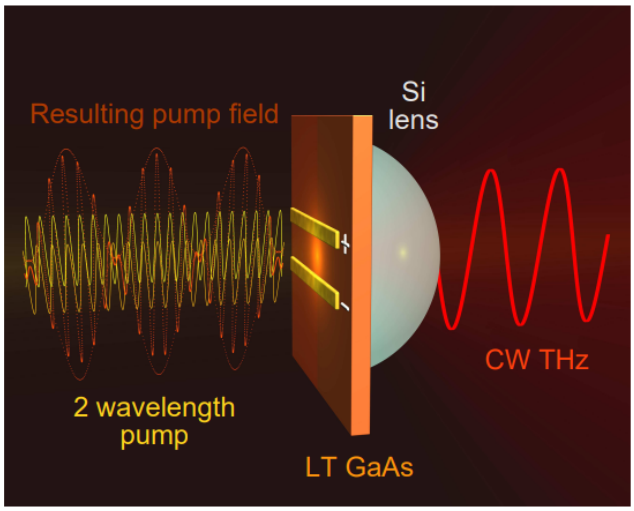

Figure 1.12: Schematic view of the experimental setup used to generate CW THz radiation by means of a LT-GaAs based photomixer. A silicon lens is used to couple the emitted THz radiation to air [31]

Considering a constant applied bias field and a weak optical excitation intensity, on the basis of equation 1.24 and 1.14, the surface photocurrent can be written as:

$$J_s(t) = I_D + \frac{I_A}{\sqrt{1+\omega_{21}^2\tau_c^2}}\sin(\omega_{21}t+\phi) \tag{1.25}$$

Having defined $I_D = E_{bias}\mu_e\tau_c(I_1+I_2)$ and $I_A = 2E_{bias}\mu_e\tau_c\sqrt{I_1I_2}$ as, respectively, the stationary and the oscillating components of the photocurrent. The oscillating component of the photocurrent is the one responsible for the generation of the THz signal. From equation 1.13, the THz field can be expressed as:

$$E_{THz}(t) \propto \frac{\partial J_s(t)}{\partial t} = \frac{\omega_{21}I_A}{\sqrt{1+\omega_{21}^2\tau_c^2}}\cos(\omega_{21}+\phi) \tag{1.26}$$

In order to obtain the maximum conversion efficiency, the intensities of the two excitation signals must be as similar as possible. Pump intensity profile, corresponding photocurrent and far field THz signal of the photomixer calculated with the described model are shown in Figure 1.13.

Terahertz radiation produced by pumping solid-state photomixers offers several advantages in particular applications, such as a narrow spectral bandwidth, which can be used to resolve individual resonances in precision spectroscopy [34], an excellent control of the emission frequency, and intensity stability.

Nevertheless, the scarce maximum achievable output power of THz photomixers represents a severe limitation in practical applications, hardly reaching the μW level due to overheating issues. Except for weak pumping regimes, the combination of continuous optical excitation and Joule heating makes the temperature at the surface of these devices extremely high. When the surface temperature gradient exceeds ~ 383 K [35, 36], device failure occurs under both room-temperature and cryogenic surrounding temperature operation. Therefore optical excitation power and bias field must be kept under a certain operating threshold in order to assure proper performance of the photomixer.

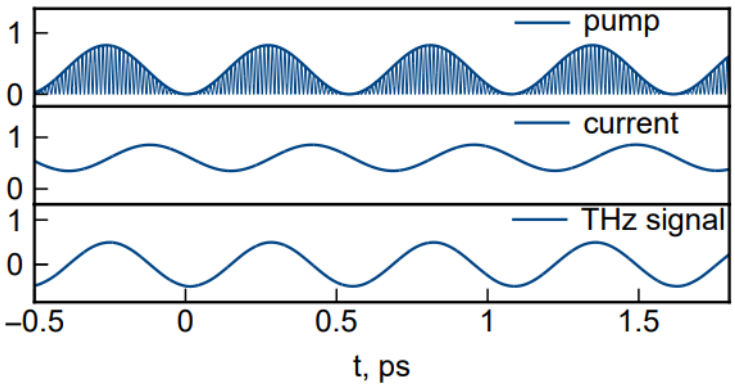

Figure 1.13: Time evolution of pump radiation envelope, antenna photocurrent and generated CW THz signal in a photomixer [31]

1.5.3 THz Time Domain Spectroscopy

An important role in wide diffusion of PCAs for THz spectroscopy has been played by the fact that these devices are not only capable of generating THz radiation but also to detect it. If the two electrodes of the antenna are connected to a current sensor rather than a power supply, a current can be measured through the contacts of the device subjected to a THz field. When optical excitation is provided, photocharges are generated in the substrate of the PCA. The incident THz field induces a time varying voltage across the photoconductive region, driving the free carriers and producing a measurable current flow in the electrodes. The induced photocurrent is directly proportional to the incident field thus allowing coherent detection, retaining both spectral and phase information of the THz signal.

This kind of detection brought to the development of THz Time Domain Spectroscopy systems that allow to reconstruct the entire profile of the THz field. An example of a standard pulsed THz-TDS setup is represented in Figure 1.14. The optical excitation is provided by a femtosecond source, generally a Ti:Sapphire laser ($\lambda \sim 800$ nm) or, in more recent applications, rare-earth-doped fiber lasers (1050 nm $< \lambda <$ 1550 nm). The optical signal is splitted by means of a beam-splitter into a pump and a probe beam. The pump beam is used in the emitter PCA to generate the THz signal, while the probe beam is focused onto the receiver photoantenna to sample the THz pulse profile. Polarization of the THz field must be perpendicular to the electrodes lines on order to obtain a current signal, thus the orientation of the receiver will be the same of the emitting device. A mechanical delay line, either on the probe or pump optical path, is used to change the time delay between THz pulse and the probe pulse. In this way the THz waveform can be scanned through its entire duration by the probe pulse, varying the time delay between the two. External noise can be partially suppressed modulating the THz field at the emission stage and extracting the demodulated signal by means of a lock-in amplifier in the detection stage. The signal modulation can be obtained mechanically by modulating the pump beam with a optical chopper, or electronically by modulation of the bias field applied to the antenna's electrodes. Eventually, the spectral content of the sampled pulse can be retrieved by Fourier transform of the acquired time-domain signal.

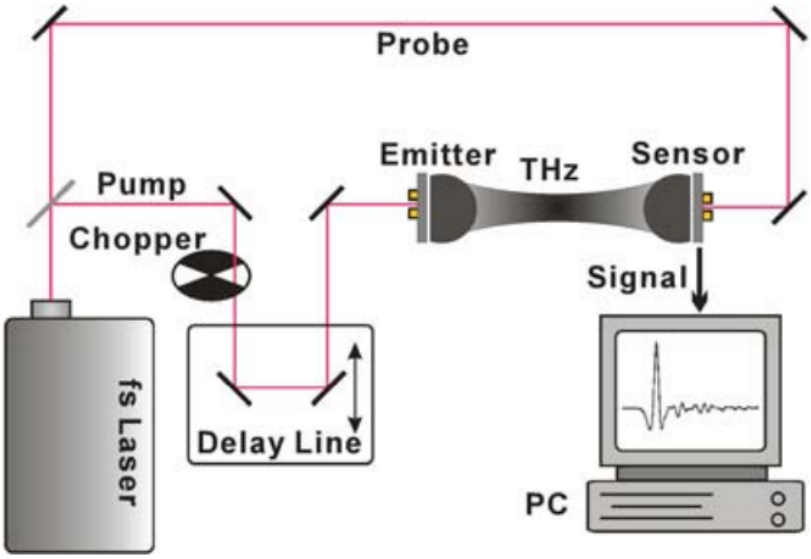

Figure 1.14: Schematic representation of the typical experimental setup of a THz-TDS system. [25]

Current generation inside the detector relies on the same process discussed for the emitter, with the only difference that the probe beam acts as a gate for the excitation of the photocarriers. Therefore the photocurrent in the receiver antenna is proportional to the convolution over time of the radiated THz field and the time-dependent conductivity of the detector. The average photocurrent as a function of delay τ between the substrate conductivity and the THz electrical pulse can be expressed as [32]:

$$i(\tau) = \left(\frac{2}{1+n_d}\right)\left(\frac{h}{T}\right)\int_0^T E_{THz}(t+\tau)\sigma_{s,d}(t)dt \tag{1.27}$$

where n_d is the refractive index of the semiconductor in the receiver antenna, h is the length of the detector electrode that is illuminated by the THz field E_{THz}, T is the time delay between successive optical probe pulses and $\sigma_{s,d}(t)$ is the time dependent surface conductivity of the detector which can be defined by an equation analogous to 1.18.

It's clear from equation 1.27 that the time response of the surface conductivity has a strong impact on the quality of the detected signal. If the conductivity resembles a narrow delta function, which is the case in short carrier lifetime photoconductors, the photocurrent will be directly proportional to the THz signal. For this reason, substrate of receiver PCAs are usually made with ultrafast photoconductive materials which present short recombination times.

A similar setup to the one in Figure 1.14 can be utilized to perform coherent detection in CW mode [37]. In this configuration the THz signal is generated and detected by a couple of photomixers, thus a double frequency pump is needed, while other components remain the same as the pulsed TDS. The detected photocurrent is a result of the superposition of the THz signal and the beating optical excitation [38]:

$$i_{ph} \propto E_{THz}\cos(\Delta\phi) \tag{1.28}$$

Where E_{THz} is the amplitude of the THz field and $\Delta\phi$ is the phase difference between the terahertz radiation and the optical beat signal. The phase difference $\Delta\phi$ can be modified acting on the variable delay stage, in such a way both amplitude and phase of the CW signal can be determined.

1.5.4 Technical layout of a Photoconductive antenna

In this section the main components and design choices adopted in the fabrication of a photoantenna will be discussed in detail, all along with the impact on performances and costs of the device. Initially a general overview of the PCA structure is presented, then breakdown in photoconductive antennas, characteristics of substrate materials and metal electrodes geometries are discussed.

General overview A top view of a standard THz PCA is shown in Figure 1.15. The main device components, including the photoconductive substrate, THz dipole antenna electrodes, and high-resistivity float-zone silicon (HRFZ Si) lens, can be seen in 1.15a. The centrally located dipole antenna is connected by means of parallel microstrip lines to larger bias pads that act as a wide electrical surface for the connection to circuitry used to apply the bias voltage. The optical pump is focused at the centre of the structure, at the the antenna dipole, where the bias field is stronger and the THz radiation is generated. The THz radiation, polarized along the axis of the bias field, propagates into the semiconductor substrate and is coupled to air by means of a Silicon lens.

The whole device is not larger than a coin, with an overall lateral dimension L in the range of a few millimeters to around a centimeter. The length of the antenna dipole D is typically of the order of 100 μm, while the gap dimension G can span from few micrometers up to almost the entire antenna dipole length D and is a particularly important parameter in the design of the PCA.

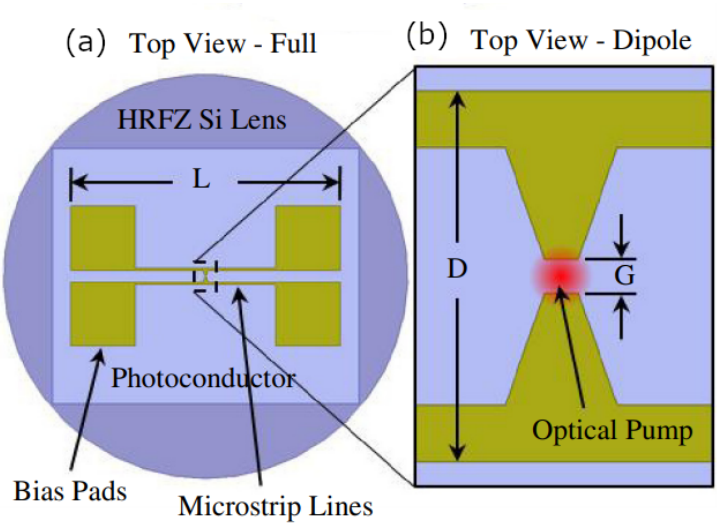

Figure 1.15: Close-up view of a photoconductive antenna. Metal electrodes, photoconductor substrate and HRFZ Si lens are represented, the antenna gap region is magnified in the box [28]

In combination with the applied bias voltage and the substrate dielectric characteristics, the gap dimension affects distribution and amplitude of the bias field in the semiconductor which in turn has a major influence on the emitted THz power, see equation 1.21.

Substrate breakdown Increasing the bias field has direct positive effects on the output power of the THz radiation. Nevertheless the electric field can not be increased indefinitely or it may cause a failure of the device due to dielectric breakdown in the substrate. Such phenomenon is called field induced breakdown: it happens when the bias field exceeds the breakdown field value of the semiconductor resulting in a instantaneous field-induced avalanche. Tipical values of the breakdown fields in photoconductive materials are in the order of hundreds of thousands of V/cm. For instance in LT-GaAs, the most diffused substrate, $E_{breakdown} \sim 300$ kV/cm [39]. Careful design of the active area of the antenna can help to increase the breakdown field and help the photoantenna to generate more intense THz pulses. Field induced breakdown is a cause of failures mainly in very small gap PCAs. The effects of a breakdown in the substrate material can be seen in Figure 1.16

Dielectric breakdown can also be caused by thermal effects in the device due to photocurrent related Joule effects and excessive optical pumping. Both optical and photocurrent energy will be partially converted into thermal energy by trapping of photocarriers and collisions between free carriers and crystal lattice. Temperature in the semiconductor will increase causing a sharp decrease in the value of the resistivity which in turn increases the current flow, generating a positive feedback loop. If proper thermal dissipation is not provided, the process will continue up to a point in which the semiconductor can no longer sustain the applied bias voltage because of the low resistivity and the breakdown occours. This is actually the most common type of breakdown in PCAs and is usually a slow process that takes some seconds or even minutes. The necessity to avoid thermal breakdown sets a trade off between the optical excitation intensity and the maximum biased voltage. In some cases, proper treatment or coating of the substrate proved to increase the breakdown field and enhance the THz generation [40].

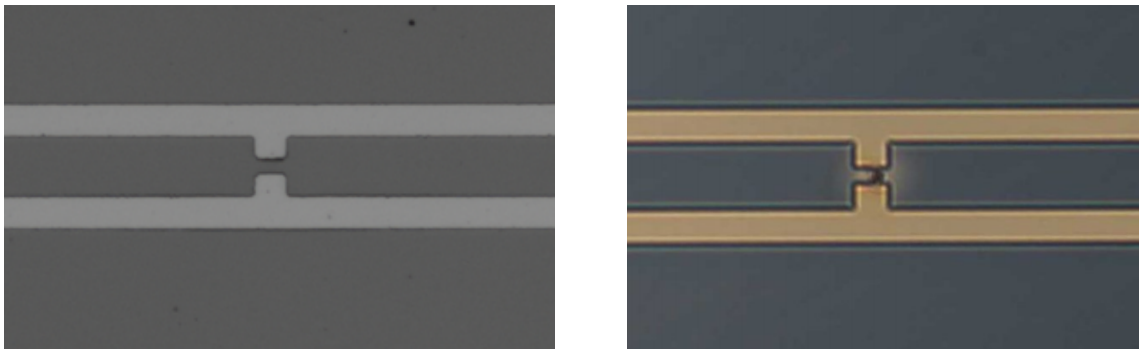

(a) (b)

Figure 1.16: Microscope view of gap region of a GaAs photoantenna. (a) Device in proper operating conditions, (b) Damaged device due to substrate breakdown [41]

Substrate materials The photoconductor substrate is perhaps the most critical component in the design of a photoantenna. On the semiconductor band structure

depend the choice of the optical excitation system and the material electro-optic characteristics influence virtually every performance aspect of the photoconductive device, such as output power, maximum optical pump, bias voltage, bandwidth and SNR. An ideal substrate material for a photoconductive antenna present the following characteristics: low carrier lifetime, maintenance of relatively high carrier mobility, appropriate bandgap, high breakdown voltage, suppression of zero bias photocurrent, and maximization the material dark resistivity. However all these properties are not indipendent of one another and in real semiconductors some trade-off may exist. While a high dark resistivity is auspicable in all applications, the optimal balance between the other characteristics depends whether the PCA is employed as a detector or a receiver. In general a short carrier lifetime tends to be more important for detectors because of the degrading impact that a slow response of the conductivity can have on the time resolution of the detected signal, see equation 1.27.
In the case of emitters a high carrier mobility is fundamental to achieve high emission power, since low values of mobility directly impact the photocurrent intensity resulting in a poor emission efficiency.

Until recently the most diffused material for PCAs substrates has been Gallium Arsenide (GaAs). GaAs has a bandagap of $1,424$ eV, corresponding to a wavelength of 871 nm, which makes it the perfect match to Titanium-doped sapphire ($Ti^{3+} : Sapphire$) femtosecond pulsed laser for optical pumping. GaAs can be obtained in different forms, depending on the temperature of growth or the presence of doping ions. The most common forms of GaAs employed in photoantennas is the Low-Temperature growth Gallium Arsenite (LT-GaAs). LT-GaAs is obtained by molecular beam epitaxy (MBE) at temperatures lower than 573 K followed by thermal annealing. As a result of the low growth temperature and the arsenic pressure during deposition, the material presents a small percentage ($1 - 2\%$) of arsenic defects. These defects are responsible for the fast carrier recombination process that results in the remarkable short carrier lifetime of this material. However, despite being the most widespread substrate, LT-GaAs present two not negligible disadvantages. The first one is the scarce reproducibility of individual semiconductor properties. Even when grown under the same conditions, two wafers generally present different characteristics in term of carrier lifetime and dark resistance. The second disadvantage is the high cost of production which prevented LT-GaAs to enter in large scale industrial production.

Another common form of GaAs is the Semi-Insulating Gallium Arsenite (SI-GaAs) which has a carrier lifetime in the order of several hundreds of picoseconds in contrast to the sub-picosecond carrier lifetime of LT-GaAs [28]. Despite of this difference, the performances of two photoantennas with the same dipole geometry but different substrates are quite similar in terms of emission spectrum, indicating that the longer carrier lifetime of SI-GaAs is not a severe limit to the high-frequency components of the radiated field, event though the effect is not completely absent as can be noticed in Figure 1.19f. Analogous considerations can be made about the impact of the different forms of GaAs on the emission power of the device which is more or less alike, see Figure 1.19a. However, LT-GaAs based antennas are generally preferred because of the higher breakdown field threshold and a more moderate saturation behaviour under strong optical pumping with respect to SI-GaAs[42].

In recent years a new class of fiber lasers with valuable properties has been

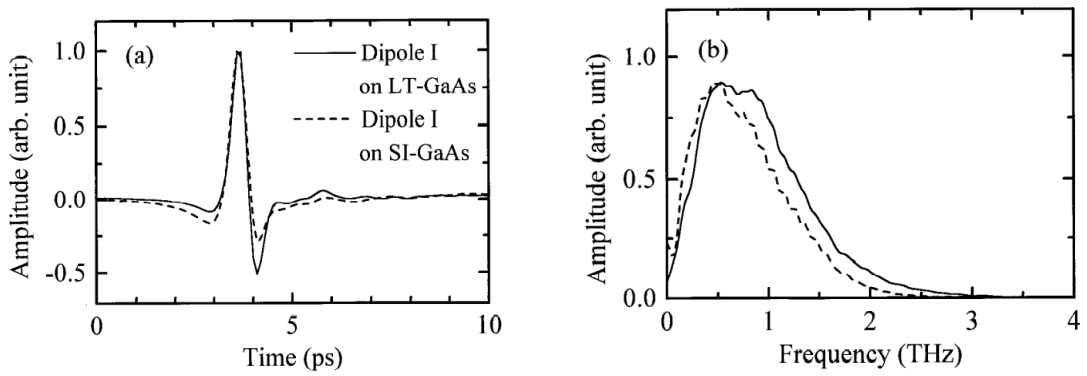

(a) (b)

Figure 1.17: Comparison of THz radiation pulses generated by two dipole antennas with different substrate materials under the same conditions. (a) Amplitude of the radiated field (b) Spectral content of the pulse. [42]

developed, such as Er:fiber ($\sim$ 1550 nm) and Yb:fiber ($\sim$ 1050 nm) lasers. The main advantages of these lasers over the most used Ti:Sapphire consist in a superior robustness, portability, stability and lower costs. The main obstacle in the direct use of these lasers as pump sources for photoconductive antennas is the reduced absorption of GaAs at longer wavelengths. For this reason new substrates with a narrower bandgap, in the order of $0.8 - 1.2$ eV, have been tested. Some examples of these alternative materials are InGaAs, InGa(Al)As heterostructures and other media with elements of groups III-V. Some of the main characteristics of these mediums are reported in in table 1.2. Unfortunately, the narrower bandgap results in a lower dark current resistance due to a larger thermal current population.

Table 1.2: Summary of substrate materials for photoconductive antennas [28]

	Advantages	*Disadvantages*	*Key performance milestones*
GaAs	Most efficient material for 800 nm excitation. Well understood growth and optimization	Poor absorption at 1.55 μm	10^4 SNR, 60 kV/cm breakdown threshold
InGaAs	1.55 μm excitation	Decreased gap dark resistivity	10 μW output THz power, 125 SNR
InGa(Al)As	1.55 μm excitation. Comparable dark resistivity to LT-GaAs	Complex material growth	10^3 SNR, 6 THz bandwidth, 1 V/cm THz amplitude
Other group III-V	Potential 1.55 μm excitation	New materials with limited understanding	1-THz bandwidth, 10^2 SNR (GaAsSb)

Electrodes geometry Electrodes are another fundamental component of a PCA. Their role is to act as an electromagnetic antenna, coupling the free-space electromagnetic radiation at THz frequencies to the photocurrent flowing in the photoconductive substrate. The most simple and widespread contact designs are based on the dipole, strip line or bow tie geometries show in Figure 1.18.

Each design has a different impact on several photoantenna parameters such as

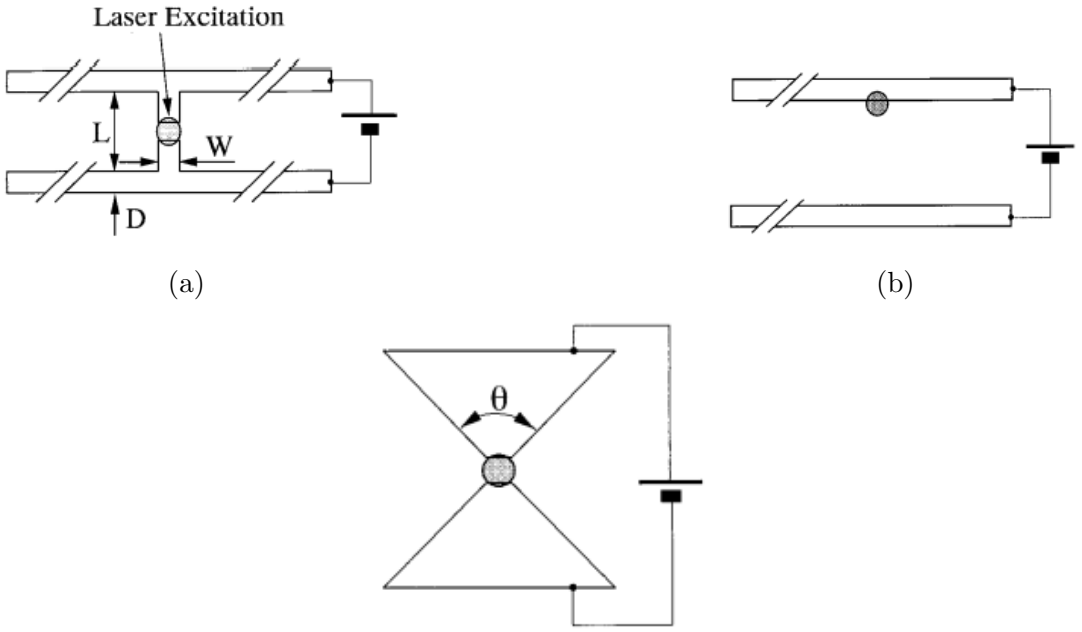

Figure 1.18: Schematic view of common electrodes geometries: (a) Dipole antenna, (b) Strip line antenna, (c) Bow-tie antenna.[42]

total efficiency, spectral response, radiation patterns and polarization of the THz signal.

Out of the three antennas, the dipole one has the poorest conversion efficiency. Under similar bias and optical pump conditions, bow tie antennas provide a larger output power but at the cost of a spectral emission content shifted to lower frequencies, as can be seen in 1.19 both in the spectral content and in the stretched pulse shape. Strip line geometry can provide the shortest pulse duration (~ 0.3 ps) and the broader spectral bandwidth. The strip line spectrum peaks at around 1 THz and extends up to ~ 4 THz, slightly outperforming the dipole design. Stripline geometry also achieves the highest output power but with a much higher bias voltage. A direct comparison of the emission power and spectral characteristics of the THz field emitted with each of the three different geometries is reported in Figure 1.19

In recent years research on novel contact designs have made a lot of progresses, introducing new layouts which could improve specific aspects of the photoantennas performance or even allow for completely new functionalities [43]. In PCA emitters the effective gap area can be increased by means of interdigitate contacts, producing larger output powers at higher saturation points [44]. Nanotechnology has also contributed, with nanostructures that can simultaneously act as contacts and plasmonic guides for the laser photons[45]. Multiple contacts devices have been developed which allow for complete characterization of the THz polarization, opening THz spectroscopy to the study of anisotropic materials [46].

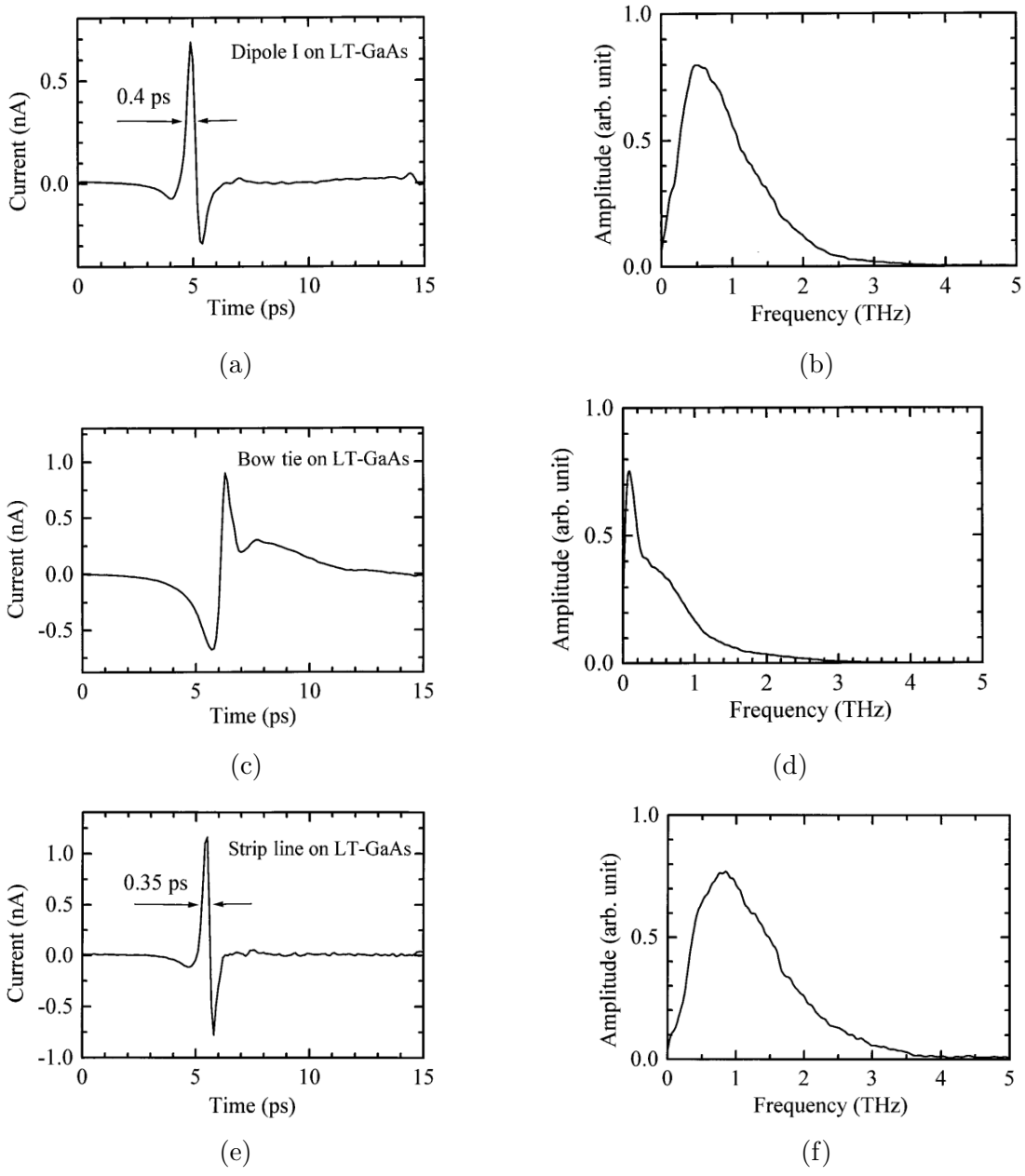

Figure 1.19: Comparison between output radiation characteristics of (a, b) Dipole, (c, d) Bow tie, (e, f) Strip line photoconductive antennas based on LT-GaAs substrate. [42]

Chapter 2

Pulsed Laser Sources for THz Generation

2.1 Ultrafast pulse generation

As discussed in the previous chapter, a large class of THz radiation sources rely on optical or near-infrared laser emission in order to operate properly. In both optical rectification processes and THz spectroscopy systems based on photoconductive antennas, the pump radiation is provided by an ultrafast laser. This noteworthy class of lasers represents one of the spearheads of laser technology, with ultrashort pulses generation and related applications being nowadays one of the most active fields in photonics. This chapter is devoted to the discussion of the main principles of ultrashort pulse generation as well as to the introduction of some of the most diffused pulsed laser sources involved in the generation of THz radiation.

Beside the role in the field of THz spectroscopy, ultrafast lasers are widely appreciated because they have proved to be a fundamental tool to study the dynamics of physical systems at very short timescales. The technique of pump-probe spectroscopy is perhaps the most excellent example of how the use of ultrashort pulses has allowed for a deeper understanding of the physics of many devices and biological systems. Moreover, an ultrashort pulse can be characterized by a high peak intensity and a broad optical spectrum, which opens to a variety of applications in material processing, non-linear optics, broadband spectroscopy and many other fields.

There has been a long-standing, ongoing effort in the field aimed at the reduction of pulse duration and at the increment of peak power of these lasers in order to improve existing applications and develop new ones. Since the development of mode-locked lasers, and in particular with effective techniques such as Kerr lens mode locking (KLM) and semiconductor saturable absorber mirrors (SESAMs), the generation of stable pulse trains from efficiently diode-pumped solid-state lasers has been made possible and is now commonly operated in research labs and industries all over the world. The continuous development has also enabled the performance of such lasers to improve by several orders of magnitude with regards to pulse duration, pulse energy and pulse repetition rates.

In this section, a simplified frequency-domain description of the mechanism at the base of mode-locking laser operation is presented, following which two of the most effective and diffused techniques for passive mode-locking will be concisely discussed.

2.1.1 Mode Locking

Mode-locking is the most used and powerful technique for the generation of ultra-short laser pulses. The term mode-locking refers to the fixed phase relation which is established between the different longitudinal modes of a mode-locked laser that allows for the generation of pulses of extremely short duration, down to the femtosecond regime, and high peak powers.

It is not uncommon for laser active mediums to show a relatively broad gain spectrum. Whenever the cavity configuration allows for it, the laser could simultaneously oscillate in several, evenly spaced, different longitudinal modes. If no particular phase relation is forced between the phases of these modes, in what is called *free running* regime, the emission intensity of the laser will show an apparently random time behavior, as shown in Figure 2.1.

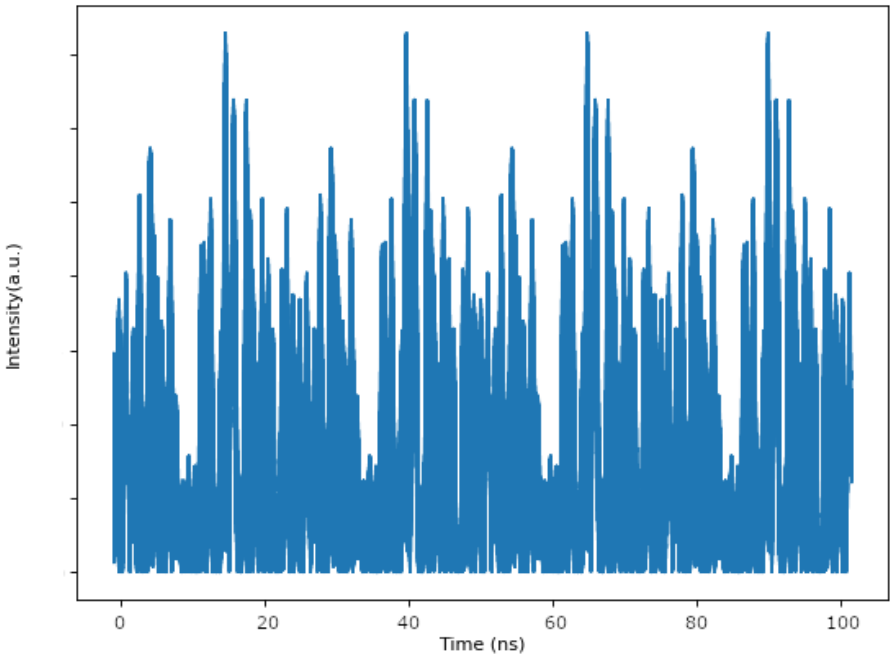

Figure 2.1: Temporal behavior of the intensity profile for 41 oscillating modes with a central wavelength $\omega_0 \sim 810$ nm, a frequency spacing $\Delta\omega = 250$ Mrad/s (39.8 MHz) between different modes, field amplitude E_0 and random phase relation.

The fact that the laser intensity is the result of a sum of sinusoidal longitudinal modes gives to the intensity profile some properties typical of Fourier series such as an overall periodicity of $\tau_p = 1/\Delta\nu$ and a duration of each spike in the random profile roughly equal to $1/N\Delta\nu$ where N is the number of oscillating modes in the cavity.

In the mode locking regime instead, a stable phase relation is forced between consecutive laser modes of equal, or at least comparable, amplitude:

$$\varphi_{l+1} = \varphi_l + \varphi \tag{2.1}$$

Where φ is a constant phase term. Considering the simple case of $2n+1$ oscillating modes of equal amplitude E_0, the total electric field of the output beam radiation

can be written in any fixed point as:

$$E(t) = \sum_{l=-n}^{n} E_0 exp\{i[(\omega_0 + l\Delta\omega)t + l\varphi]\} \tag{2.2}$$

where ω_0 is the central mode frequency, $\Delta\omega$ is the frequency difference between two consecutive modes and the the phase term of the central mode has been taken as reference.

From equation 2.2 the field can be rearranged into the product of a carrier wave at frequency ω_0 and a time dependent amplitude:

$$A(t) = \sum_{l=-n}^{n} E_0 exp\{il(\Delta\omega t + \varphi)\} \tag{2.3}$$

Given the fact that the phase term remains constant in time, it is possible to define a new temporal variable t' which satisfies:

$$\Delta\omega t' = \Delta\omega t + \varphi \tag{2.4}$$

In the new timescale the total complex field amplitude can be written as:

$$A(t') = \sum_{l=-n}^{n} E_0 exp\{il(\Delta\omega t')\} \tag{2.5}$$

The sum appearing in the right-hand side of equation 2.5 resemble a geometric progression with a ratio $exp\{i\Delta\omega t'\}$ between consecutive terms. Summing the terms of this progression the field amplitude becomes [47]:

$$A(t') = E_0 \frac{\sin[(2n+1)\Delta\omega t'/2]}{\sin[\Delta\omega t'/2]} \tag{2.6}$$

An example of the time profile of the mode locked laser emission intensity is represented in Figure 2.2.

It can be noted that the phase locking condition determines an interference of the longitudinal modes in the cavity which translates in a train of evenly space pulses on the output. Pulse peaks occur when the denominator of equation 2.6 tends to zero, i.e. when $\Delta\omega t'/2 = n\pi$ with $n = 0, 1, 2, ...$ The first maximum thus occurs at $t' = 0$ s and successive pulses are separated by a time interval:

$$\tau_p = \frac{2\pi}{\Delta\omega} = \frac{1}{\Delta\nu} = \frac{2L}{c} \tag{2.7}$$

where $\Delta\nu$ is the frequency spacing between consecutive modes and L is the length of the optical cavity. The value of the peak intensity can be derived from equation 2.6 when the denominator approaches zero: $A_{peak} \approx (2n+1)^2 E_0^2$ which is $(2n+1)$ times larger than the average intensity in the free running regime.

The experimental techniques to force a fixed phase relation between modes inside the laser cavity can be grouped into two distinguished classes, namely the active mode-locking methods and the passive mode-locking methods. In the active techniques, the mode-locking element is driven by an external source. Active induced

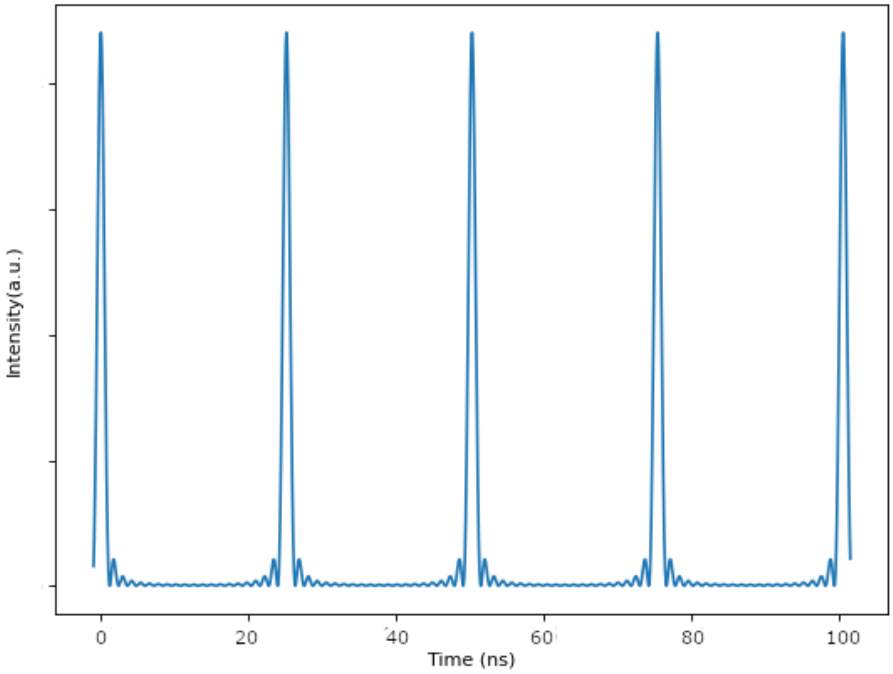

Figure 2.2: Intensity of the instantaneous complex amplitude $|A(t')|^2$ for 41 phase-locked oscillating modes with arbitrary central frequency ω_0, field amplitude E_0 and a mode spacing $\Delta\omega = 250$ Mrad/s (39.8 MHz)

mode locking can be achieved through three different techniques. The first one consists in the periodic modulation of the amplitude of the field (Amplitude Modulation mode locking); the second technique relies on the use of a phase modulator (Phase Modulation mode-locking); and the third is based in the periodic modulation of the laser gain, generally obtained varying the pumping intensity between zero and the peak value at a frequency equal to the fundamental frequency of the cavity (Synchronous Pumping mode-locking).

In passive mode-locking methods the element which induces mode-locking is not externally driven, instead it exploits some non-linear optical effects such as a saturation of the absorption or optical induced refractive index change in suitable materials. Passive mode locking techniques can be divided into four main categories: The first one makes use of the saturation properties of a fast saturable absorber, generally a dye molecule or a semiconductor (Fast saturable absorber mode-locking); the second technique exploits the Kerr effect in suitable transparent non-linear optical materials (Kerr Lens Mode-Locking); it is also possible to take advantage of the dynamic saturation of the gain medium (Slow saturable absorber mode-locking); and the fourth technique leverages the self-phase modulation induced in a non-linear optical material element in an auxiliary cavity coupled with the main one (Additive Pulse mode-locking).

Among the various viable methods of laser mode-locking, passive techniques, in particular fast saturable absorber and Kerr-lens mode locking, proved to be able to generate the shortest pulses and are relatively simple to implement. The next section presents more extensively these two techniques.

2.1.2 Passive mode locking methods

In general, passive mode locking techniques rely on the saturation of laser losses in correspondence of high intracavity powers. This non-linear behaviour for the intracavity losses is achieved by means of a particular class of materials, the so called saturable absorbers, which for high intensities of the incident radiation show a drop in the absorption of electromagnetic radiation.

Each time an energetic pulse impinges on the saturable absorber, it temporarily saturates the absorption, thus reducing laser losses, as shown in Figure 2.3. The mode-locking process can originate from noise fluctuations of the intracavity power, with an occasional spike experiencing weaker losses and higher gain with respect of radiation of lower intensity. The initial noise is then amplified at every round trip inside the cavity resulting in a single intense radiation pulse, while light at lower intensity will experience losses higher than the gain thus rapidly vanishing. The saturable absorber also tends to shrink the pulse duration, being the initial low power leading wing of the pulse absorbed in the passage through the material. In fast saturable absorbers the unsaturated absorption characteristics are rapidly recovered and also the trailing edge of the pulse is attenuated at each round trip in the cavity. A steady state is eventually reached when the amplification is just sufficient to compensate the circulating pulse losses and the dispersion inside the cavity balances the shrinking effect of the pulse edges.

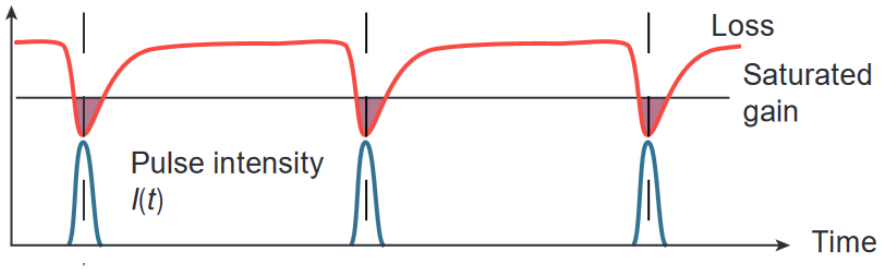

Figure 2.3: Illustration of the mechanism of fast saturable absorber passive mode-locking [48]

In general, a saturable absorber is made of an optical material which absorbs at the laser wavelength and shows an opportune absorption saturation intensity. A variety of suitable materials have been developed for the scope, some examples are the semiconductor saturable absorber (SESAM), graphene saurable absorbers and rare hearth or transition metals doped crystals. There are also various kinds of artificial saturable absorbers which do not directly exploit the saturation of absorption of a single solid state material but rather take advantage of non linear effects to modulate the losses inside the resonator. In Kerr lens mode locking for instance, losses are determined by the effect of non-linear phase shifts. The rest of this section is devoted to the discussion of two widely adopted methods for passive mode locking, the first exploiting the Kerr lens effect and the second based on a highly adjustable semiconductor structure.

Kerr-lens mode-locking Kerr lens mode locking was discovered in the nineties, perhaps in a stroke of serendipity, by a research group working on a broadband Ti:Sapphire laser [49]. Since then, it has been the leading mode locking technique in the achievement of the shortest ever witnessed light pulses, with frontier duration of $5 - 6$ fs and sub-two optical cycle pulses [50, 51]. Despite the initial uncertainty about the actual physical process at the root of this technique, the theory of Kerr lens mode locking is nowadays well understood and has been studied in detail [52]. In this section just the basic working principle based on the Kerr lens effect is introduced.

When an intense beam of light interacts with a non-linear optical medium, it induces a refractive index change in the material proportional to the intensity of the beam itself. In this sense the refractive index can be expressed as:

$$n = n(I) \simeq n_0 + n_2 I \tag{2.8}$$

Therefore the non linear refractive index will be distributed accordingly to the spatial distribution of radiation intensity impinging on the material. If the intensity profile of the transverse mode of the laser can be assimilated to a Gaussian distribution, the effect of the non linearity is to actually create a convex lens for the laser radiation. The kerr lens effect can be exploited to create a saturable absorber inside the resonator using two main configurations.

The first one, commonly referred to as 'hard-aperturing' is shown in Figure 2.4. It consists in a simple aperture placed after the non linear medium, across the beam path. When low intensity radiation travels through the non linear medium, it experiences hardly any focusing effect and it is consequently partially absorbed by the sides of the aperture. High intensity radiation is instead focused by means of non linear Kerr effect taking place inside the medium. The smaller beam size allows the high intensity radiation to pass through the aperture without experiencing any significant loss. This intensity dependent behaviour of the cavity losses is effectively the same of a bulky saturable absorber and can be exploited to induce mode-locking operation.

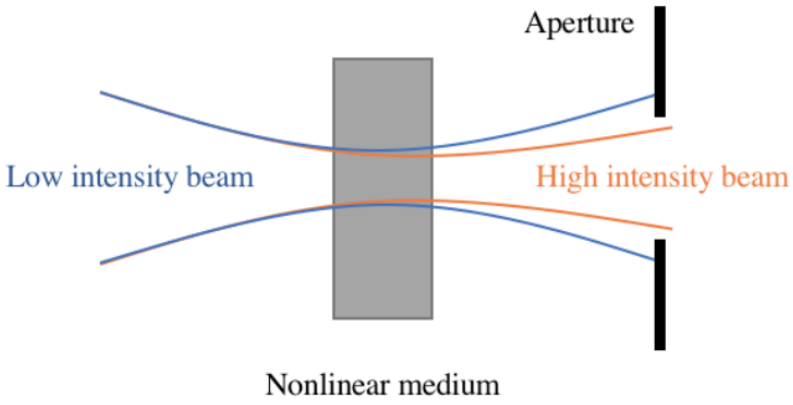

Figure 2.4: Schematic representation of a 'hard aperture' mode-locking configuration. [53]

The second commonly used configuration, also called 'soft-aperture' mode locking, is illustrated in Figure 2.5. In this situation the non linear process takes place

directly inside the laser active medium and no physical aperture is present in the cavity. The overall entity of the resonator losses is determined by the spatial overlap between the pump beam and laser radiation. Modes which are fully overlapped to the spacial region inverted by the pump beam experience a larger gain than modes that are just partially overlapped. The pump beam dimension can be designed so that its spacial distribution is larger than the one of high-intensity self focused beams and smaller than the one of low-intensity beams. In this situation high-intensity modes will experience a stronger gain than low-intensity ones, thus mimicking the behaviour of a fast saturable absorber.

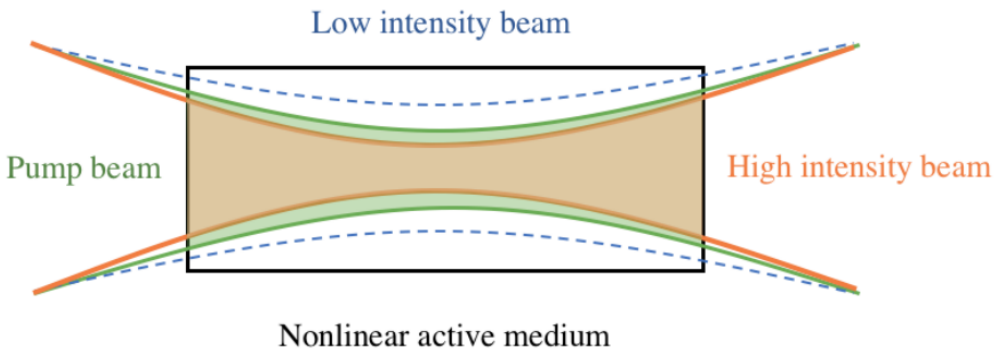

Figure 2.5: Schematic representation of a 'soft aperture' mode-locking configuration.[53]

Nevertheless, a Kerr lens mode locked laser presents the significant drawback of being not self-starting, that means that the mode locking regime needs to be induced by an additional external perturbation that momentarily increases the noise in the cavity, spurring the pulse formation. This perturbation is generally achieved by mechanically shaking one of the laser cavity mirrors. This hinders the application of Kerr lens mode locking to compact, turn-key solid state lasers, for which the adoption of bulky semiconductor saturable absorbers is more indicated.

SESAM A saturable absorber is a material that shows a decreasing absorption in response to an increasing incident light intensity. The saturation of absorption in the material is a direct consequence of the ground state population transition to excited energy states through a sufficiently intense pulse excitation. For a time interval shorter than the decay time of the excited states the ground state remains depleted and therefore no further absorption can take place.

In a simple model of saturable absorption, in which the relaxation time of excited states is considered indipendent from the incident intensity, the absorption rate of the material can be written as:

$$\alpha(I) = \frac{\alpha_0}{1 + \frac{I}{I_0}} \tag{2.9}$$

Where α_0 is the linear absorption and I_0 is the saturation intensity, which is a function of the excited state lifetime τ and the absorption cross-section σ:

$$I_0 = \frac{h\nu}{2\sigma\tau} \tag{2.10}$$

Semiconductor materials are ideally suited for being exploited as intracavity fast saturable absorbers for mode locked lasers. They are characterized by a broad range of absorption wavelengths, from the visible to the mid-infrared, and their absorption recovery time and saturation fluence can be controlled altering growth parameters and design of the devices.

One of the most important type of saturable absorber is the semiconductor saturable absorber mirror. In a SESAM device the semiconductor saturable absorber is directly integrated into a mirror structure which could be used as a cavity end mirror. The SESAM works in reflection, showing a higher reflectivity, and thus lower cavity losses, for higher incident intensities. A characteristic of the reflectivity of a generic SESAM device is shown in Figure 2.6.

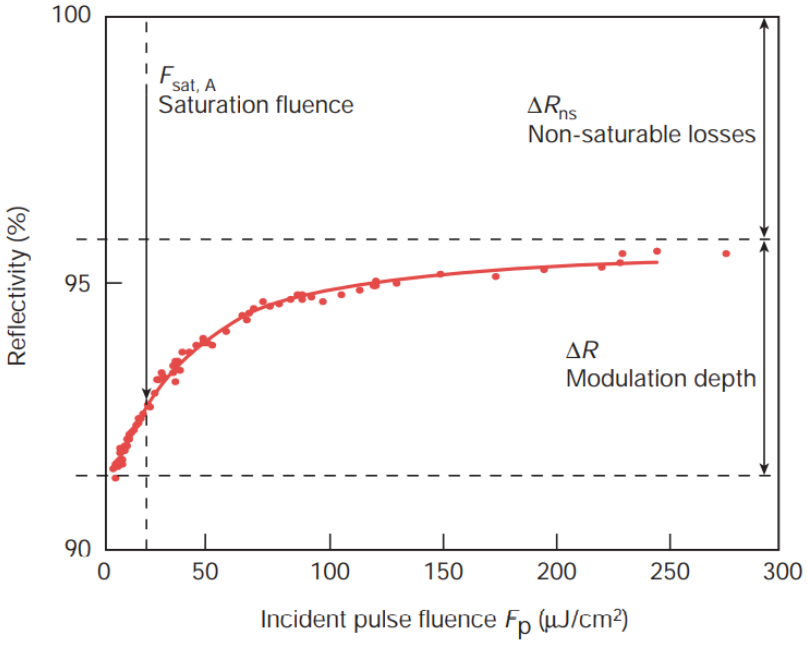

Figure 2.6: Reflectivity of a SESAM device as a function of the incident optical fluence F_p. [48]

In contrast to Kerr lens mode locking lasers, in SESAM mode-locked systems the operation is turn-key and the design of the saturable absorber, thus its main optical characteristics, can be optimized independently from the cavity parameters. These characteristics, coupled with compactness and the well established fabrication processes for semiconductor materials, has made SESAMs widely used in different kinds of lasers, especially in semiconductor and solid state ones.

Some of the most common designs of SESAMs devices are schematized in Figure 2.7. The semiconductor material is generally placed inside a Fabry-Perot cavity, formed by a distributed Bragg reflector on one side and a dielectric mirror on the opposite one. The thickness of the semiconductor absorber can be adjusted in order to obtain a device operating at anti-resonance which results in a broader bandwidth and a lower group velocity dispersion. The top dielectric mirror is another adjustable parameter that determines the radiation intensity entering the absorption layer. Depending on the desired effective saturation intensity or absorption cross-section, the top dielectric mirror be replaced by an anti-reflective coating or not be present at all, exploiting the Fresnel reflection at the semiconductor-air interface [54, 55].

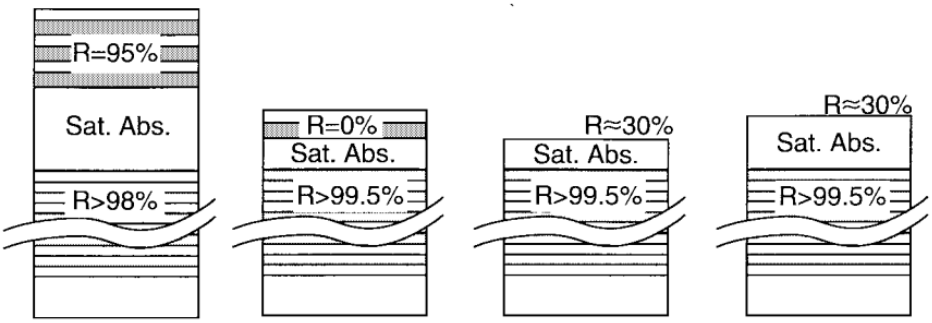

Figure 2.7: Examples of some common SESAM designs. [54]

After this brief review about some of the key principles and tools for ultrafast pulses generation, the actual laser sources used to generate this kind of radiation will be investigated. The next section will be focused on solid state lasers, which are the most used optical pump sources in THz spectroscopy systems. After a brief introduction on solid state laser technology, some of the most popular solid state lasers are individually analized.

2.2 Solid state lasers

The term Solid State Laser (SSL) is generally used to indicate a laser system whose active media consists in a transparent host material doped with optically active ions. To this class belong all bulk crystalline lasers and glass fiber lasers, whilst semiconductor sources are traditionally not included in the category because of the different mechanism of pump and laser action.

Since the first demonstration of the lasing capabilities of ruby crystals [56], SSL have played a central role in the advancement of photonic research and a large number of laser systems are now available, providing a wide range of output characteristics in terms of average and peak power, pulse width, pulse repetition rate, bandwidth and wavelength. The flexibility, robustness and excellent performances of these lasers has made them popular in many scientific and industrial applications, from manufacturing to health care devices.

The pump mechanism in SSL is generally optical, relying on flashlamps, arclamp or the more efficient laser diodes. The optical resonator can be built according to the characteristics of the active medium in order to guarantee efficient laser emission, either in air or in fiber. A large number of passive and active components have been developed to shape the spectral, temporal, and spatial profile of the output beam.

The basic properties of a solid-state laser are dominated by the interaction of the laser-active ion and the host lattice. In order to guarantee proper operating conditions, the host crystal must posses appropriate optical, mechanical and thermal properties. Favorable optical properties such as the absence of refractive index variations are fundamental to avoid inhomogeneous propagation of light through the crystal, that would otherwise result in a poor quality of the output beam. Thermo-mechanical properties, such as thermal conductivity, hardness and fracture strength, influence the heat dissipation and stability of the laser. Another important factor is the lattice structure itself since symmetry and distribution of the crystal field directly

affect the energy of the optical transitions of the laser and the lattice parameters determine the compatibility with the dopant ions.

Elements belonging to the transition series of the Periodic Table are the most commonly used as active impurities in the host materials. In particular Transition Metals (TM) and Rare-Earths (RE) ions proved to be excellent active species for laser action.

The general electronic configuration of lanthanoid RE elements can be written in the form $(Xe)4f^N5s^25p^65d^06s^2$, with N electrons in the partially filled $4f$ shell and the $6s$ shell completely full, as listed in table 2.1 for some elements of the lanthanoid series. Once doped in host materials, RE elements triply ionize using two of the $6s$ and one of the $4f$ electrons to form the ionic binding. The remaining N-1 electrons can then rearrange into different states, corresponding to a manifold of energy levels that are further splitted by the Coulomb interaction among the $4f$ electrons and Spin-Orbit coupling. Crystal field interaction has a rather weak effect on energy levels distribution, being the electrons in the inner $4f$ orbital partially shielded by the $5p$ and $5s$ ones. Consequently, the emission wavelengths of RE solid state lasers are to a large extent independent from the host lattice [57]. On the other hand, it is thanks to the weak effect of the crystal field interaction on wavefunctions with opposite parity that parity forbidden $4f$-$4f$ transitions have a non-zero, although still rather low, transition probability [47]. This low probability and the weak electron-phonon coupling, due to the screening effect of external orbitals, result in long radiative lifetimes. Therefore in general SSL based on RE can achieve laser action with moderate threshold pump powers.

Table 2.1: Electronic configurations of some common solid-state laser active species. [53]

	Elements	**Electronic configuration**
Rare Earths	Pr	$(Xe)4f^35d^06s^2$
	Tb	$(Xe)4f^95d^06s^2$
	Dy	$(Xe)4f^{1}05d^06s^2$
	Ho	$(Xe)4f^{1}1^5d^06s^2$
	Er	$(Xe)4f^{1}25d^06s^2$
	Tm	$(Xe)4f^{1}35d^06s^2$
	Yb	$(Xe)4f^{1}45d^06s^2$
Transition Metals	Ti	$(Ar)3d^24s^2$
	Cr	$(Ar)3d^54s^1$
	Fe	$(Ar)3d^64s^2$

The electronic configuration of transition metal is also represented in Table 2.1. These elements experience a double or triple ionization when used as dopants for host materials. In the case of doubly ionized elements, such as Co and Ni, the two electrons in the $4s$ shell are used to form the ionic binding, whilst for the triply ionized metals, among which Ti and Cr, also one of the $3d$ electrons is involved in the bond. As it happens in lanthanoids, the electrons remained in the partially

filled shell can rearrange themselves into a manifold of energy states useful for laser operation. However in the case of TM ions the interaction with the crystal field is quite strong, due to the absence of external shielding shells. The interaction result in a remarkable broadening of the absorbtion and emission cross-sections for the $3d$-$3d$ transitions. An additional effect of the crystal field is to facilitate the transitions within the $3d$ shells which, in combination with the stronger electron-phonon coupling due to the absence of the shielding effect of external orbitals, result in a shorter radiation lifetime with respect to RE elements. This translates into the need of pump sources with higher powers than the one used in lasers based on RE ions. On the other hand the broader transition bandwidths of TM lasers could be beneficial in ultrafast pulse generation.

In the following the most diffuse SSL sources used as optical pump for THz photoconductive antennas are discussed. Among bulk crystalline active mediums, Ti:Sapphire is the most common choice due to the 800 nm emission wavelength which is strongly absorbed by the GaAs substrate of PCAs. The advent of new substrate materials allowed to pump at longer wavelengths, which opened to the possibility of using RE doped lasers such as Ytterbium ones.

2.2.1 Ti:Sapphire laser

Ti:Sapphire is perhaps the most widely used solid-state laser in the near-IR range, appreciated for its great wavelength tunability and its versatility in the generation and amplification of femtosecond mode-locked pulses. Ti:Sapphire is characterised by a broad vibronic fluorescence band that allows for a wide range of variation of the emission wavelength between 670 and 1070 nm, with the peak of the gain curve around 800 nm.

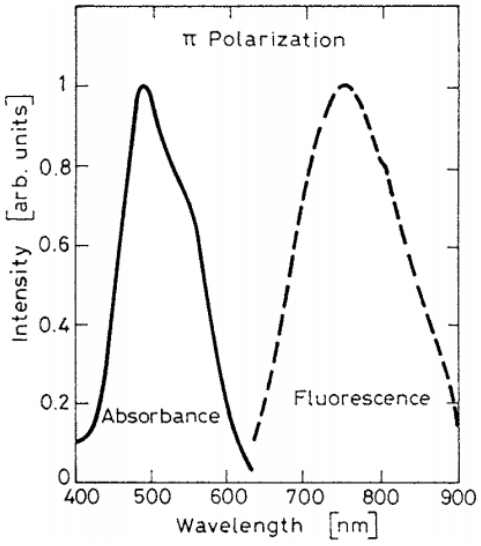

Figure 2.8: Absorption and emission spectra of Ti:sapphire [58].

The host sapphire crystal (Al_2O_3) present a very high thermal conductivity, exceptional chemical inertness and mechanical rigidity. Transition metals can be readily incorporated in the crystal substituting the Aluminum ions at the centre of an octahedral site.

When doped in Al_2O_2, only one electron is left in the $3d$ shell of the Ti ionized atom, being both the $2s$ electrons and one of the $3d$ electrons involved in the ionic binding. The Ti^{3+} takes the place of an Al^{3+} ion at the centre of an octahedral site, with the six apexes occupied by oxygen anions. The structure of the doped crystal lattice is represented in Figure 2.9a. Assuming a perfect symmetry of the octahedral site and neglecting spin effects, the influence of the crystal field of the nearest O^{2-} ions splits the initially five-fold degenerate d-electron levels of an isolated Ti^{3+} into a triply degenerate $^2T_2$ ground state and a doubly degenerate ^2E upper state [47] as shown in Figure 2.9b. Further corrections to the energy levels of the ground and upper states due to higher order effects of the crystal field and spin-orbit interaction are of much weaker entity and have not been considered in detail herein, for a more exact discussion the interested reader is referred to [59, 60].

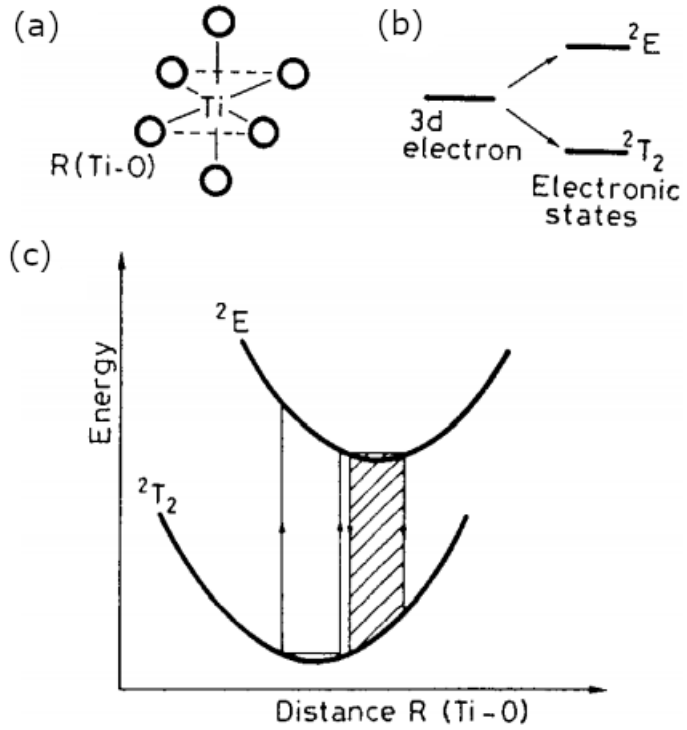

Figure 2.9: (a) Octahedral configuration of Ti:sapphire; (b) Splitting of 3d energy states under the effect of an octahedral crystal field; (c) Energy states in a configuration-coordinate model. [47]

The energy level structure of the Ti^{3+} ion is quite unique among transition-metal laser ions because of the lack of other d-state energy levels above the ^2E state. This eliminates the possibility of excited-state absorption of the laser radiation, an effect which generally limits tuning range and efficiency of other transition-metal-doped lasers. As represented in Figure 2.9c Laser action is originated from the transition between the lowest vibrational level of the ^2E state and the vibrational levels of the $^2T_2$ state. The energy difference between the lower and the upper laser states is roughly 19000 cm^{-1} [61]. More data about laser parameters of Ti:sapphire can be found in table 2.2.

Sapphire doped with $\sim 0.1\%$ Ti^{3+} by weight exhibit a broad absorption band in the blue–green region of the visible spectrum, peaked around 490 nm. The ab-

sorption and fluorescence spectra for Ti:Al2O3 are shown in Figure 2.8. Ti:sapphire lasers are commonly pumped by argon lasers or by frequency-doubled Nd:YAG and Nd:YLF lasers at ~ 532 nm. Generally a very high pump flux is required owning to the short fluorescence lifetime of the upper state.

Table 2.2: Laser parameters of $Ti : Al_2O_3$ [58]

Index of refraction	1.76
Fluorescent lifetime	3.2 μs
Fluorescent linewidth (FWHM)	180 nm
Peak emission wavelength	790 nm
Peak stimulated emission cross-section:	
parallel to c-axis	$\sigma_{\parallel} \sim 4.1 \cdot 10^{-19}$ cm^2
perpendicular to c-axis	$\sigma_{\perp} \sim 2.0 \cdot 10^{-19}$ cm^2
Stimulated emission cross-section at 0.795 nm	$\sigma_{\parallel} \sim 2.8 \cdot 10^{-19}$ cm^2
Quantum efficiency of converting a 0.53 μm pump photon into an inverted site	$\eta_Q \approx 1$
Saturation fluence at 0.795 nm	$E_S = 0.9$ J/cm^2

2.2.2 Yb-Doped Solid-State Lasers and Materials

In the development of ultrafast lasers, Ti:Sapphire has proven to provide the most remarkable pulse duration (< 5 fs), but the lack of direct high power diode pumping systems matching the absorption wavelength imposes some limitations to the efficiency and costs of these lasers. In contrast, Ytterbium (Yb)-doped materials show a large absorption cross-section around 975 nm, where high power InGaAs diodes and specific pumping schemes are avalaible, thus allowing for direct diode pumping. This pumping mechanism and the high optical-to-optical efficiency obtainable in Yb-lasers are among the main reasons of the rapid expansion of industrial and research market of these systems.

The trivalent Yb^{3+} ion is characterized by just two optically accessible electronic states, the $^2F_{7/2}$ ground state and the $^2F_{5/2}$ excited state, separated approximately 10000 cm^{-1} from one another and composed of four and three Stark levels respectively. The absence of additional parasitic levels above the excited one eliminates commonly undesired effects such as excited-state absorption, upconversion, cross-relaxation, and concentration quenching, providing the possibility of high doping levels. The separation between the $^2F_{7/2}$ ground state and the $^2F_{5/2}$ excited state can generally be considered independent from the particular host material and equal to the one of the free ion [62]. This approximation stems from the fact that the spin orbit interaction responsible for the separation between the two levels is only marginally affected by the presence of the crystal field. In general there are two mechanisms in which the spin-orbit coupling can be affected by an external crystal field. The first could be a direct modification of the spin-orbit coupling constant. The second contribution of the crystal field to the energy separation could come

from J-mixing, which correspond to the mixing of states belonging to $^2F_{7/2}$ and $^2F_{5/2}$ that could result in an increase in the energy separation between the two levels. However the impact of the crystal field on the spin-orbit constant is predicted to be rather weak for lanthanide ions and the effect of J-mixing can be neglected to a good approximation due to the relatively large energy separation between the two levels [62]. Hence it is reasonable to assume the energy separation between the ground and excited manifolds of states in a Ytterbium laser equal to the spin-orbit splitting measured for the free Yb^{3+} ion.

In contrast, the splitting of some spectroscopic levels within the ground and excited Stark levels, in particular in the $^2F_{7/2}$ state, is proportional to crystal field strength. Laser action is precisely allowed by the splitting of these degenerate electronic states under the effect of the external field [63], resulting in a quasi three level scheme. As a consequence of the sensibility of the energy levels distribution on the crystal field, the spectroscopic characteristics and laser properties of Ytterbium show a marked dependence on the type of host material employed. For this reason a variety of different host materials have been studied for the Yb^{3+} laser.

The laser transition takes place from the lower level of the $^2F_{5/2}$ manifold to an intermediate Stark level above the ground state of the $^2F_{7/2}$ manifold. The energy separation between the terminal laser level and the ground state of the $^2F_{7/2}$ manifold is generally comparable to the thermal energy at room temperature. For instance in a $Y_3Al_5O_{12}$ (YAG) crystal doped with Yb^{3+} the separation is 612 cm^{-1} while thermal energy at room temperature is $\sim$ 207 cm^{-1}, making the terminal state of the laser thermally populated. Therefore Yb^{3+} lasers are generally best described by a quasi-three level system, as shown in Figure 2.10.

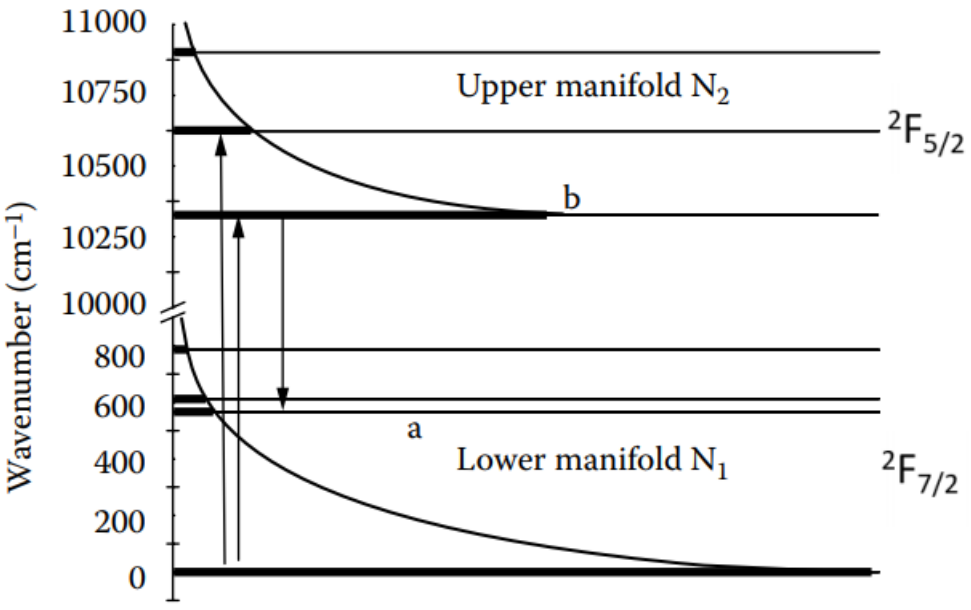

Figure 2.10: scheme of the energy level diagram in the case of Yb:YAG. The population corresponds to the length of the energy level. [62]

Considering the $^2F_{7/2}$ manifold, the population within sublevels can be described according to Boltzmann distribution:

$$f_a = \frac{exp(-E_{la}/kT)}{Z_l} \tag{2.11}$$

Where f_a and E_{la} represent respectively the fraction of population in the terminal laser level a and the energy of the level. Z_l is the partition function of the whole ${}^2F_{7/2}$ manifold and can be expressed as:

$$Z_l = \sum_i exp(-E_{li}/kT) \tag{2.12}$$

Where E_{li} is the energy of the i level within the lower manifold.

In Yb lasers the unpumped medium is therefore absorbing at the laser wavelength, making the pump intensity needed to reach threshold different from zero even in an ideally lossless cavity. Strong pump intensities are generally required to deplete the ground state and prevent reabsorption. A strong crystal field is generally desirable because it results in a wider separation between the split energy levels which in turns makes the laser operating scheme resemble more to a four level one, with a lower thermal population in the terminal level and a limited reabsorption of the laser radiation [64, 65].

The fraction of the population in the excited level to achieve population inversion $f_b N_2 \geq f_a N_1$ corresponds to the β coefficient:

$$\beta \geq \frac{f}{1+f} \tag{2.13}$$

with $f = \frac{f_a}{f_b}$ and $\beta = \frac{N_2}{N_{total}}$.

The minimum β value describes the tendency of the laser system toward a quasi-four level scheme: the lower the β_{min} the lower fraction of the population is needed in the upper laser level to reach population inversion. For instance to the laser transition of the Yb:YAG crystal represented in Figure 2.10 correspond a $f = 0.066$ and a $\beta_{min} = 0,062$. Clearly for this transition, the fraction of population that needs to be in the upper manifold in order to reach population inversion is relatively small.

For what concerns absorption, Yb-doped active media show an intense and broad absorption spectra around 975 nm. As a consequence of the energetic structure of the Yb^{3+} ion, the active medium can be pumped at wavelengths really close to the laser's one. This results in a low quantum defect, typically less than 10%, which in turn reduces the thermal load on the host material and increases the laser global efficiency.

The influence of the crystal host in a Yb-laser extends far beyond the solely thermo-mechanical properties of the active material. In addition to the aforementioned crystal field effect on the energy levels splitting, also an unusually strong electron-phonon coupling is showed in Yb^{3+} doped materials [66]. This coupling is responsible for an homogeneous broadening of the electronic lines, which in combination to the splitting of the energy levels lead to a remarkably broad absorption and emission spectra.

A variety of crystals and glasses have been tested as host materials for Yb^{3+} ions. In general, crystals are characterized by higher emission cross-sections and a better thermal behavior with respect to glasses, but due to the ordered lattice structure the emission bandwidths are generally narrower. On the other hand, the disordered structure of glasses contributes to a inhomogeneous broadening of the emission spectra, but at the cost of a poor thermal conductivity and mechanical

resistance, which coupled with generally weaker emission cross-sections result in severe limitations, especially in high power applications.

Aside of ordered crystals there is an entire class of particular crystal hosts which present a disordered structure around one type of substitution site. This configuration leads to a locally variable crystal field around the dopant ions which determines a broadening of the linewidths of the electronic transitions for ytterbium cations as it happens in glasses. Some examples of crystals with these characteristics are tetragonal double tungstate and molybdate, which show an almost random distribution of Na^+ and trivalent Yb^{3+} cations over two lattice sites, or the Yb:$CaGdAlO_4$ (CAlGO) where the broad absorption and emission bands are due to Yb^{3+} occupancy in Ca^{2+} and Gd^{3+} crystallographic sites which present different sizes and cationic charges [67]. The main properties of the most interesting Yb-doped crystals for femtosecond laser applications are summarized in table 2.3.

Table 2.3: Main experimental results of Yb-Doped laser materials developed in diode-pumped fs mode-locked laser oscillators [62]

Material	*Experimental Duration*	*Central Laser Emission*	*Minimum Theoretical Duration*	*Average Output Power*
Yb:YAG	340 fs	1031 nm	124 fs	110 mW
Yb^{3+}:$Y_3Al_5O_{12}$	810 fs	1030 nm		60 W
Yb^{3+}:glass	58 fs	1020 nm	31 fs	65 mW
Yb^{3+}:$Ca_4GdO(BO_3)_3$	89 fs	1044 nm	26 fs	40 mW
Yb^{3+}:$Sr_3Y(BO_3)_3$	69 fs	1062 nm	18 fs	80 mW
Yb^{3+}:$KGd(WO_4)_2$	240 fs	1028 nm	44 fs	22 W
Yb:KGW	112 fs	1045 nm	44 fs	200 mW
Yb^{3+}:$KY(WO_4)_2$	71 fs	1025 nm	46 fs	120 mW
Yb^{3+}:$SrY_4(SiO_4)_3O$	110 fs	1070 nm	16 fs	420 mW
Yb:SYS	94 fs	1070 nm		110 mW
Yb^{3+}:Sc_2O_3	230 fs	1044 nm	95 fs	540 mW
Yb^{3+}:CaF_2	150 fs	1033 nm	30 fs	880 mW
Yb^{3+}:Y_2O_3 ceramic	615 fs	1076 nm	75 fs	420 mW
Yb^{3+}:YVO_4	120 fs	1021 nm		185 mW
Yb:SYS//YAG	130 fs	1072 nm	40 fs	1 W
Yb^{3+}:Lu_2SiO_5	260 fs	1059 nm	75 fs	2.6 W
Yb^{3+}:$CaGdAlO_4$	47 fs	1050 nm	15 fs	300 mW

Yb:CAlGO in particular seems to be a promising active material because it combines some interesting properties for the generation of ultrashort pulses. The first one is the record low quantum defect achievable in these type of lasers, $\eta = 0.8\%$ with $\lambda_{pump} = 980$ nm and $\lambda_{laser} = 987.6$ nm [67], which combined with the very high thermal conductivity, $k > 6\frac{W}{mK}$ for 2%-doped crystals [68], results in excellent thermal properties allowing for high power pumping. In addition Yb:CAlGO presents one of the broadest and flattest emission spectra of all the Yb-doped mate-

rials, exhibiting a plateau between about 990 nm and 1060 nm with relatively high emission cross-section values. The emission features of the Yb:CAlGO are presented in Figure 2.11 for different values of the β coefficient.

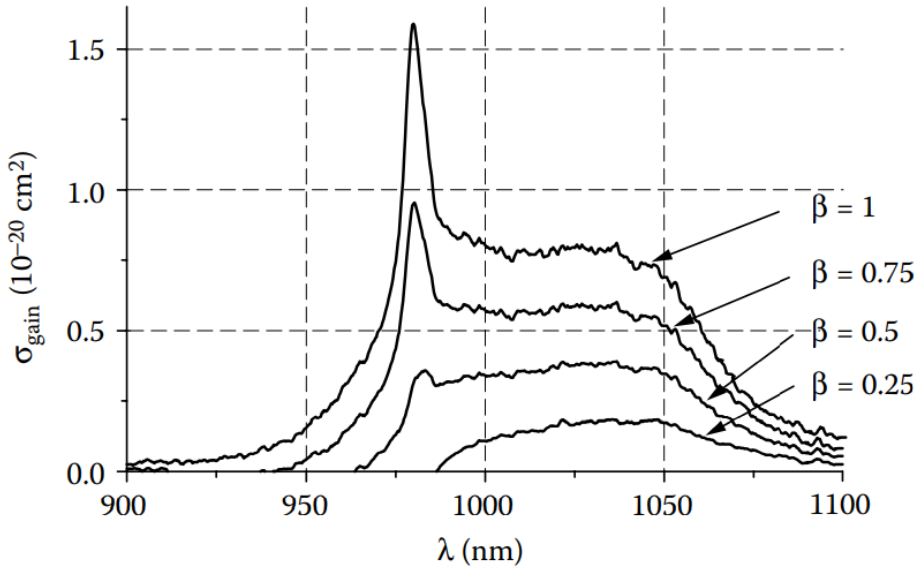

Figure 2.11: Gain cross section for the Yb:CAlGO laser material in sigma polarization. Only the positive values are presented in this spectrum. [62]

Yb-doped crystals are a class of excellent active materials, however progresses in the development of glass fibers have enabled an increasingly attractive alternative for RE active species. While the electronic configuration of fiber lasers is similar to the one of bulk crystals (considering the same host material), many other laser characteristics such as output power, beam quality, thermal management and wall plug efficiency are quite different in fiber lasers. For this reason, a brief introduction to the characteristics of RE-doped fiber lasers is provided in the next section.

2.2.3 Fiber lasers

Fiber lasers are among the most recently developed and disruptive class of solid-state lasers, allowing for high power CW or pulsed operation from nanoseconds down to ultrafast durations, turn-key operation and small footprint. Although already proposed soon after the first laser demonstration [69], fiber lasers have become of practical use only in more recent times thanks to the evolution of efficient diode-lasers pumping systems and the advent of suitable techniques for the fabrication of single-mode silica fibers.

In a fiber laser the inner core is doped with rare earth ions, the most common being Ytterbium and Erbium, and acts as active medium for the amplification of laser radiation. The most diffused types of fibers are silica-glass and single mode, nevertheless multimodal fibers and different glass compositions are not uncommon, an example is the ZBLAN fluoride glass widely used in IR lasers due to its large transmission bandwidth and low chromatic dispersion. The laser cavity may be built either by means of bulk mirrors or fiber Bragg gratings directly incorporated in the fiber core. The pump beam is coupled along the longitudinal axis of the fiber and,

depending on the fiber design, it is guided directly by the inner core (conventional single mode fiber lasers) or by an additional cladding around the active core (double-clad laser).

There are a number of features that differentiate fiber lasers from other laser technologies and result in superior overall performance in several situations. Standard silica glass fibers are characterized by excellent thermo-mechanical properties. The large surface to volume ratio of the long and slender geometry allows efficient heat transfer radially from the active core to the fiber surface resulting in a superior thermal management and elimination of thermal lensing effects. The flexible optical fiber construction guarantees also the robustness of the device and low maintenance requirements. In addition the amorphous nature of the glass host produces inhomogeneously broadened active-ion emission and absorption spectra [70], which enables the tuning of fiber lasers from continuous wave to ultra-short pulse operation.

Another benefit of fiber lasers is the remarkable wall-plug efficiency. This is obtained in high power devices through the double-clad design, shown in Figure 2.12, which confines pump light into a larger multimode optical waveguide around the smaller doped central core, forcing multiple interactions along the length of the fiber. The double-clad design has been the key enabling advance to scale up emission power of fiber lasers, allowing to harness the high power of lower brightness diodes as pump sources [63]. In principle, the smaller overlap between pump light and active core medium should lead to weaker pump absorption but the effect is well compensated by the longer interaction length offered by the fiber.

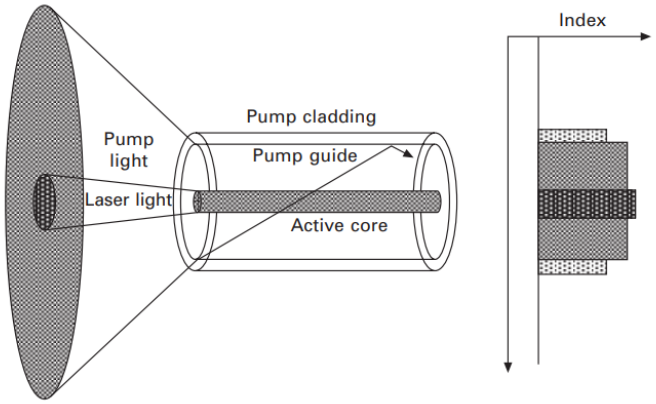

Figure 2.12: Illustration of a double-clad optical fiber and its refractive index profile. [58]

Perhaps the most characterizing feature of fiber lasers is the superior beam quality and stability. Through an appropriate design, the optical waveguide can be made to support a single transverse Gaussian-like optical mode. This high degree of mode control is complex to achieve with other laser technologies and was the main reason why fiber lasers were studied in the first place. Single-mode optical fibers are currently widely used in telecommunication systems.

Given the refractive index of core and cladding layers the numerical aperture of a conventional fiber can be written as [58]:

$$NA = \sqrt{n_{co}^2 - n_{cl}^2} = n_0 \sin(\theta_a) \tag{2.14}$$

Where n_0 is the refractive index of the medium outside the fiber, usually air, and θ_a is the acceptance angle of the incident cone of pump radiation, as illustrated in Figure 2.12.

Under weak guiding approximation, i.e. small difference between n_{co} and n_{cl} which is the case for the vast majority of fibers, propagating modes are well approximated by linearly polarized LP_{lm} modes [71], with l radial mode number and m azimuthal mode number. A useful adymensional parameter used to describe the modal characteristics of a fiber is the normalized frequency V:

$$V = \frac{2\pi}{\lambda}\rho NA \tag{2.15}$$

Where ρ is the core radius and λ is the radiation vacuum wavelength. Fibers with V number lower than 2.405 can sustain only a single transverse guided mode and are therefore monomodal. For larger normalized frequencies the number of modes increases as $\propto \frac{V^2}{2}$. It is worth noting that different combinations of core radius and numerical aperture can end up in fibers with the same modal characteristics. Each mode experiences an effective index n_{eff} which assumes a value between n_{co} and n_{cl}. The closer is the effective index to the core index the higher is the guiding strength of the mode. A normalized propagation constant, bounded within 0 and 1, can be defined for each mode in the form:

$$b = \frac{n_{eff}^2 - n_{cl}^2}{n_0^2 - n_{cl}^2} \tag{2.16}$$

Normalized propagation constants as a function of normalized frequency up to $V = 10$ are represented in Figure 2.13 for different guided modes.

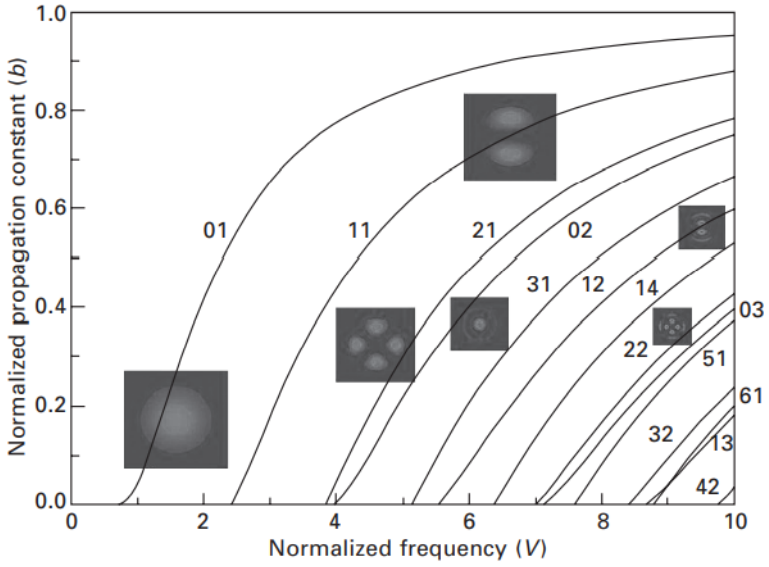

Figure 2.13: Normalized propagation constants for a step-index fiber and spacial profile of different LP modes.[58]

Another aspect that differentiate fiber lasers from crystal ones regards optical dispersion. Total dispersion in an optical fiber is given by the sum of the effects of

intrinsic material dispersion, the same contribution that can be found in a crystal laser, and the additional waveguide dispersion:

$$D = D_m + D_{wg} \tag{2.17}$$

Where the waveguide dispersion D_{wg} is a function of the normalized frequency, the index contrast and the radiation wavelength:

$$D_{wg} = \frac{n_{co} - n_{cl}}{\lambda} D(V) \tag{2.18}$$

Where $D(V)$, also referred to as normalized waveguide dispersion, is a dimensionless function of V whose behaviour is shown in Figure 2.14. It is worth noting that waveguide dispersion is entirely normal ($D_{wg} < 0$) in the single-mode regime and becomes anomalous in the multimode regime only when $V > 2.68$ for step-index fibers.

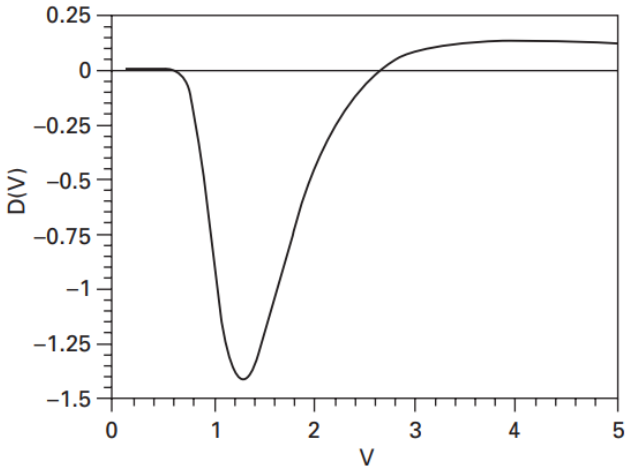

Figure 2.14: Normalized waveguide dispersion in optical fibers for different values of the normalized frequency V [58]

Chapter 3

Experimental Setup

The spectrometer developed and characterized during this thesis work is based on a 800 nm Ti:Sapphire laser source, pumping a pair of LT-GaAs dipole photoconductive antennas. The generated THz signal is collimated and focused in the receiver antenna by means of a couple of parabolic mirrors. This setup allows to analyze different kind of materials: the sample can be placed in between the two mirrors or directly in front of the receiver photoantenna and the THz signal transmitted through the sample is measured and compared to the one gathered for free propagation. Material's response in the THz region can be completely characterized from the analysis of the spectrum of the acquired time domain signal.

In this chapter the most important components of the spectrometer under consideration, namely the pump laser and the photoconductive antennas, are firstly introduced, followed by a synoptic analysis of the entire experimental setup,the measurement process and the optimization of the THz signal.

3.1 Ti:Sapphire pump laser

As pointed out in chapter 1, LT-GaAs is characterized by a strong absorption band in the 800 nm region of the electromagnetic spectrum. For this reason, in the experimental setup the choice of the laser pump source for the photoconductive antennas fell on a solid-state Ti:Sapphire laser. The laser is Kerr-lens mode locked, providing ultrafast, large bandwidth pulses with duration approaching tens of femtoseconds.

In this section a general overview of the main characteristics of this laser, such as the pumping system, cavity configuration and output pulse characterization, is presented. A more detailed discussion of every aspect concerning the design and performance characterization of the system under consideration can be found in [72].

3.1.1 Pumping system

As for all active laser materials, Ti:Sapphire needs to be pumped in order to reach the population inversion that allows for laser action. The absorption band of Ti:Sapphire is between 450 nm and 600 nm, peaking approximately at 500 nm, which makes frequency-doubled Neodymium solid state lasers a convenient choice for the pump system. In this type of lasers the output radiation is obtained starting from the 1064 nm laser radiation of a Nd crystal by means of second harmonic generation inside

a non-linear optical material lacking inversion symmetry, such as Barium Borate (BBO). Efficient frequency doubling in continous-wave operation can generally be accomplished by means of intracavity frequency doubling, i.e., by placing the non linear crystal directly inside the laser resonator in order to exploit the high intracavity radiation intensity. The actual experimental configuration used during this thesis work implements a commercially available 532 nm Verdi V 10 frequency-doubled Nd ring laser, whose technical specifications and cavity layout are reported in Table 3.1 and Figure 3.1 respectively.

Table 3.1: Laser parameters of Verdi V10 [73]

Output Power (CW)	> 10 W
Wavelength	532 nm
Line-width	< 5 MHz
Beam Diameter	$2.25(\pm 10\%)$ mm
Beam Divergence	< 0.5 mrad
Polarization	vertical; $> 100 : 1$
Power Stability	$\pm 1\%$
Noise (RMS)	$< 0.01\%$

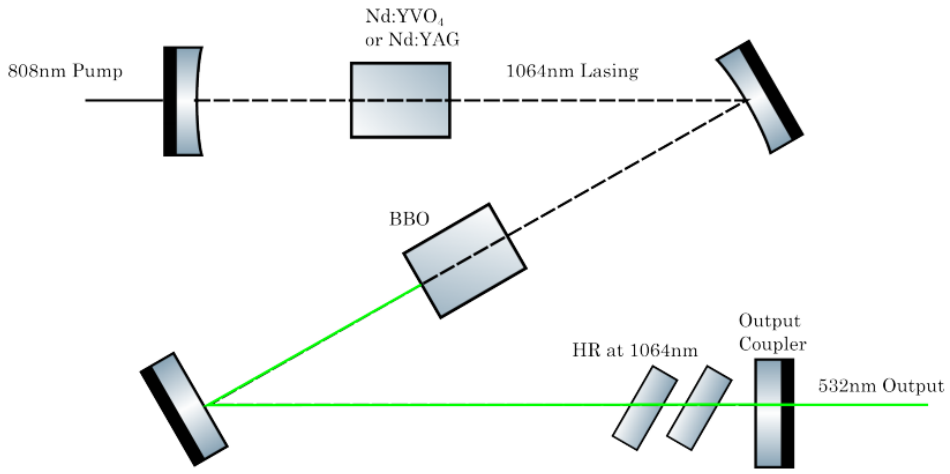

Figure 3.1: Simplified scheme of the frequency-doubled Nd laser cavity. [72]

Before entering the Ti:Sapphire laser cavity, the initially vertical polarization of the 532 nm pump beam is rotate by 90 degree to the horizontal direction by means of a periscope. In this way the pump radiation is p-polarized with respect to the Ti:Sapphire crystal surface and reflection losses can be minimized taking advantage of the total transmission at the Brewster's angle. Right after the polarization rotation, the pump beam is focused on the Ti:Sapphire crystal by a $f = 60$ mm plano-convex spherical lens. Both the two identical $r = 50$ mm plano-concave mirrors of the laser cavity that lie along the pump direction present a very low reflectivity at the pump wavelength ($R(532\text{ nm}) < 5\%$)

3.1.2 Ti:Sapphire cavity configuration

In addition to the two plano-concave mirrors, the laser cavity is constituted by other five flat chirped mirrors and an output coupler. The cavity configuration and geometrical dimensions are illustrated in Figure 3.2. The Ti:Sapphire active

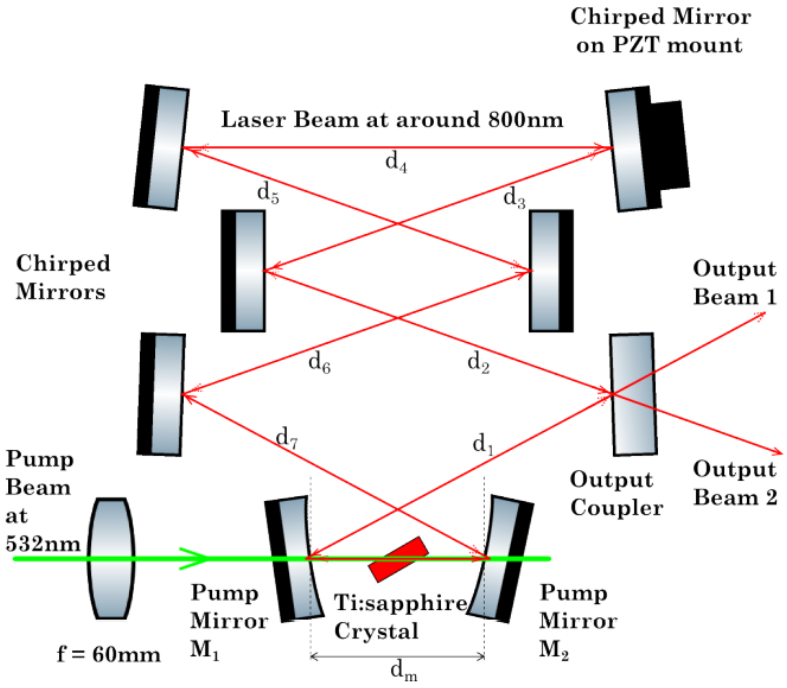

Figure 3.2: The ring resonator, where the red lines represent the approximate paths of the laser beam, and the green line represents that of the pump beam. Where $dm = 52.7$ mm, $d1 = 156$ mm, $d2 = 150$ mm, $d3 = 145$ mm, $d4 = 208.2$ mm, $d5 = 166.1$ mm, $d6 = 172$ mm, $d7 = 150$ mm. The two pump mirrors $M1$ and $M2$ have radius of curvatures of 50 mm and chirped multilayer coatings. [72]

material is mounted on a Peltier cell which is used to control and stabilize the crystal temperature, preventing mode locking instabilities and thermal lensing effects. The Peltier cell itself is in turn connected to a water cooling system for efficient heat dispersion. The crystal temperature is constantly monitored by means of a resistive thermistor.

The length of the resonator has been originally designed in order to assure a 250 MHz pulse repetition rate:

$$L \approx \frac{c}{f_r} = \frac{3 \cdot 10^8 m/s}{250 \cdot 10^6 Hz} = 1.2m \tag{3.1}$$

The effective optical length of the cavity depends both on the geometrical distance between the mirrors and the refractive index of air. Since these parameters can vary with environmental factors such as temperature, humidity and mirror vibrations, one of the resonator mirrors is mounted on a piezoelectric transducer (PZT) which gives a fine control on the cavity length.

Dispersion compensation is obtained by means of chirped multilayer coatings on seven of the eight mirrors of the laser cavity. Mode locking operation is achieved by means of 'soft aperture' Kerr lens, as described in chapter 2.1, the pump beam being

tightly focused into the active crystal. In order to produce transient instabilities to spur the initial mode locking pulse, the length of the cavity can be temporary varied. One of the mirrors is indeed mounted on a elastically movable support which allows for temporary changes in the cavity length without detrimental effects on the laser alignment. To reduce instabilities due to fluctuations in environmental parameters, the whole structure is eventually encapsulated in an acoustic isolation case made of a metal box internally coated with isolating foam. Figure 3.3 shows the Ti:Sa laser cavity in proper operating conditions.

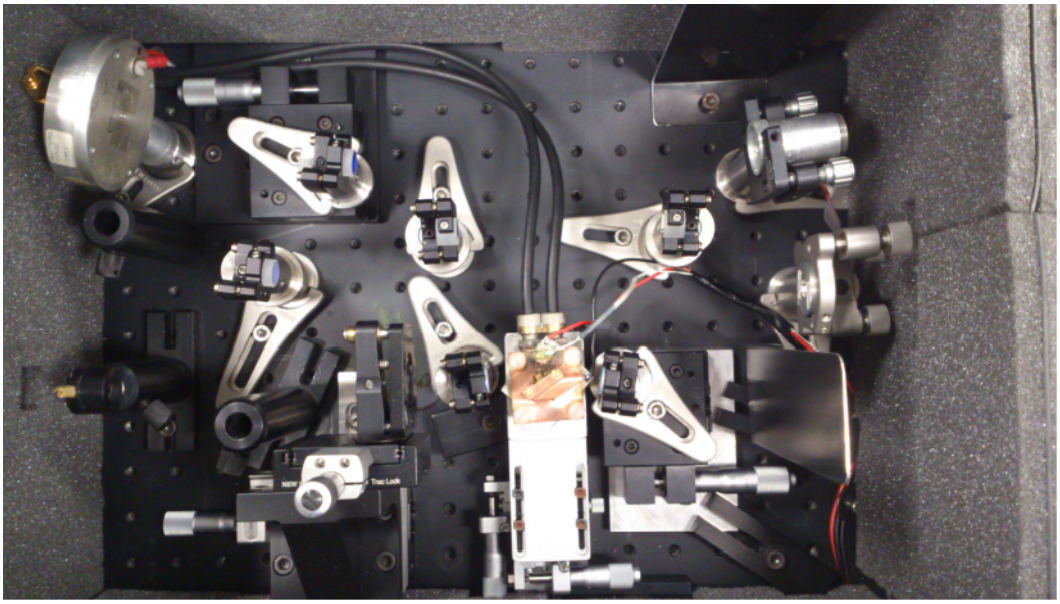

Figure 3.3: Picture of the experimental setup of the Ti:Sapphire laser.

3.1.3 Pulse characteristics

In this paragraph the salient output performance of the experimental Ti:Sapphire laser under operating conditions are reported. A more extensive and detailed characterization of the pulse train can be found in [72].

Given the extremely short time scale, the temporal profile of the output pulse of the Ti:Sapphire laser has been characterized by means of nonlinear-non collinear intensity autocorrelation. With a 5% output coupler and a pump power of 3.5 W, the estimated width of the output pulse is close to 30 fs [41]. Under the same pump and coupling conditions the mean output power is measured to be of the order of 220 mW. Main characteristics of the experimental Ti:Sapphire laser are summarized in table 3.2.

It's worth noting that, in contrast to CW operation which is bidirectional, the mode-locked laser generally works unidirectionally due to mode competition. Therefore the output pulse train can be observed along just one of the two CW output directions illustrated in Figure 3.2.

The spectral content of the fs pulse has been acquired with a spectrum analyzer and is shown in Figure 3.4. It is necessary to specify that, because of the limited space available, the radiation spectrum has not been taken straight out of the laser but instead after the passage through a beam splitter. The effect of the finite

Table 3.2: Operational parameters of Ti:Sapphire [41, 72]

Pump power	3.5 W
Avg emission Power (ML regime)	$\sim$ 220 mW
Central wavelength λ_c	$\sim$ 816 nm
Spectral bandwidth $\Delta\lambda$	35.3 nm
Pulse duration	19.7 fs
Pulse repetition frequency	250 MHz
Peak power	$\sim$ 44 kW.

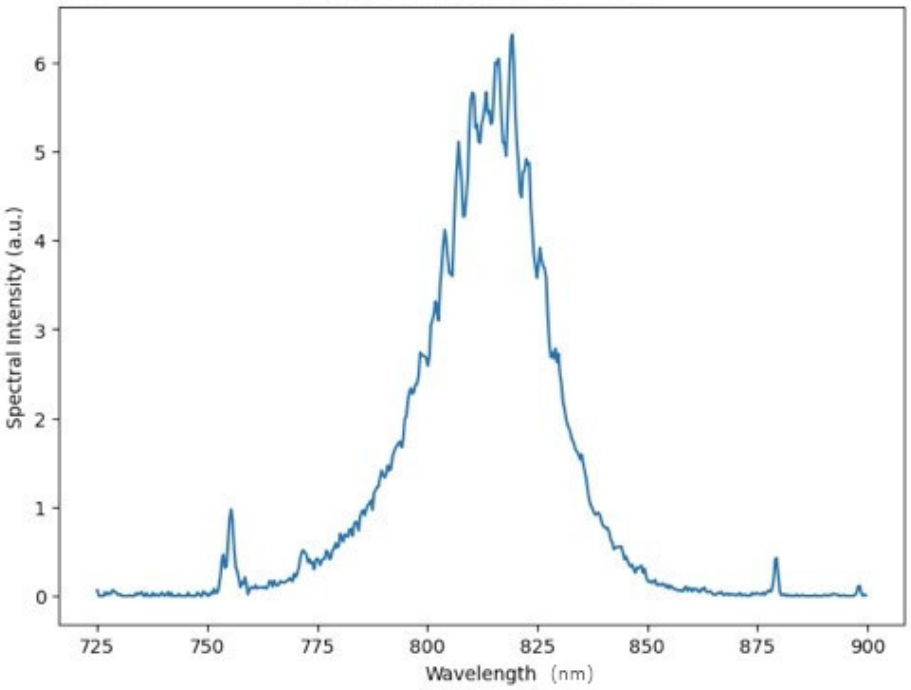

Figure 3.4: Spectral intensity of a Ti:Sapphire laser pulse. The spectrum was acquired after the passage through a beam splitter.

thickness of the beam splitter is clearly visible in the periodic modulation of the spectral intensity in the main peak. Another interesting feature of Figure 3.4 is the presence of the so called Kelly sidebands on either side of the central peak. These narrow peaks are more commonly observed in fiber lasers, where the long nonlinear interaction length is responsible for energy perturbation to the average soliton model [74] and are evident in bulk lasers only at wavelengths for which the cavity dispersion has a value close to zero.

3.2 Photoconductive antennas

Photoconductive antennas are perhaps the most important components of a time domain THz spectrometer, being every aspect of the THz signal directly influenced by the PCA features. In the experimental setup of this thesis work a pair of commer-

cial devices were used, namely two TERA 8-1 photoconductive antennas produced by Menlo Systems Inc, a first one for the emission and a second one for the detection of the THz signal. These antennas are characterized by a single wrapped metal dipole structure deposited onto a LT-GaAs substrate. The wrapped dipole geometry is a particular variant of the simple dipole geometry discussed in Chapter 1. The wrapped design presents a spiral layout of the metal contacts around the central dipole, as can be seen in Figure 3.5. This layout, along with the four crosses surrounding the central dipole, has the advantaged of facilitating the alignment procedure of the photoantennas. The dipole has a 20 μm extension with a central gap size of 5 μm and the whole photoantenna chip is mounted on a PCB which makes for a robust structure of the device.

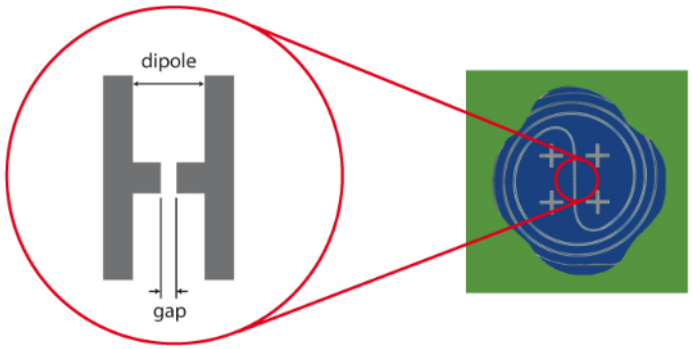

Figure 3.5: TERA 8-1 THz antenna structure [75]

In ideal conditions the TERA 8-1 should guarantee a bandwidth exceeding 4 THz for a 800 nm laser pump system, with THz pulses shorter than 100 fs. For a correct usage of the device, the input optical power of the pump laser pulse must not exceed 10 mW and in order to prevent substrate breakdown the bias voltage applied to the emitter must be kept below 40 V. A summary of the most relevant technical specifications of this model of photoconductive antenna is reported in Table 3.3.

Table 3.3: TERA 8-1 specifications [75]

Antenna material	LT GaAs
Antenna structure	Wrapped dipole
Dipole length	20 μm
Gap size	5 μm
Substrate size	$5.0x5.0x0.35$ mm^3
Laser wavelength	$\sim$ 800 nm
Bandwidth	$>$ 4 THz
Optical power	$<$ 10 mW
Pulse duration	$<$ 100 fs
Bias voltage	recommended $\pm$35 V (max $\pm$40 V)

The PCA chip has been mounted on a specific holder, the T8-H2 THz mount [76], from the same producer of the photoantennas. The holder offers the possibility

to regulate and finely adjust the position of the photoantenna along both vertical and horizontal directions, which is a fundamental requisite to correctly align the impinging Ti:Sapphire laser pulse onto the microscopic gap of the dipole. In order to optimize the perfomance of the photoantennas two different lenses are integrated in the mount. A first infrared aspheric focusing lens, of focal length $f = 7.5$ mm, is placed in front of the PCA chip in order to focus the pump infrared beam into the tiny area of the gap. The mount offers the possibility to regulate the position of this aspheric lens along the direction perpendicular to the PCA plane. The second lens, a high resistivity silicon hyperhemispherical lens of diameter 10 mm, is placed right after the PCA and has the double function of filtering the remaining infrared radiation and collimating the THz wave.

A correct alignment of the infrared beam into the gap region of the photoconductive antenna is of fundamental importance, for both an efficient generation and a correct detection of the THz signal rely on the photocurrent generated by the excitation of the impinging pulse. The alignment procedure is composed of different stages. Initially the infrared beam coming from the Ti:Sapphire laser is made to travel parallel to the optical table and to impinge perpendicularly onto the aspherical lens. During this procedure the antenna's chip can be replaced by an iris in such a way to use the position of the infrared beam beyond the PCA plane to verify the alignment and to maximize the transmitted power. After this preliminary stage, the two photoantennas and the silicon lenses are installed in the mount, a 30 V bias voltage is applied to the PCAs and an infrared camera is used to look at the radiation reflected by the antenna's metal electrodes. With the help of the camera and an amperometer which measures the photocurrent in the antennas, the position of the chip is scanned in the vertical and horizontal direction until the infrared beam is correctly aligned into the gap of the dipole, see Figure 3.6. The generated photocurrent is then further maximized by optimizing the focus of the input infrared lens changing its distance from the antenna.

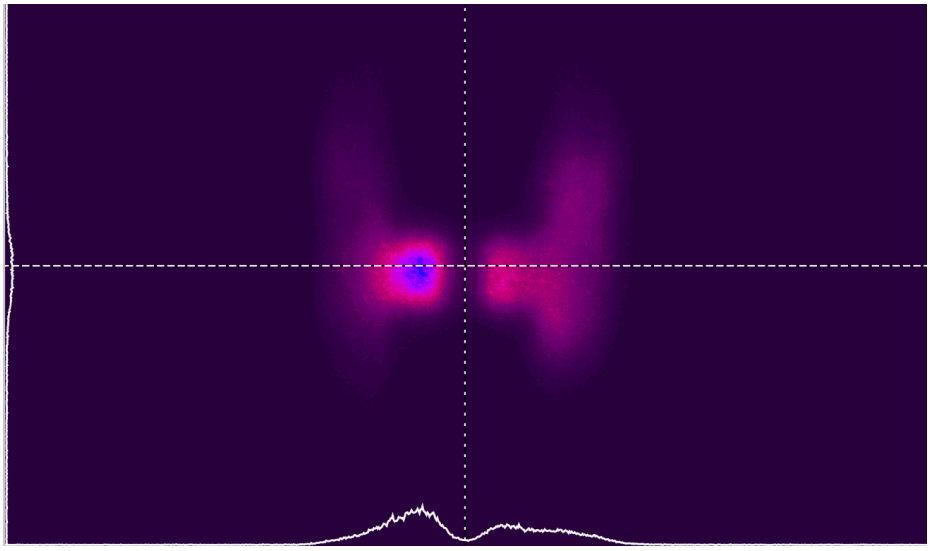

Figure 3.6: Image of the photoantenna's gap as seen from the infrared camera during the alignment. The reason why the dipole structure is clearly visible is that the focal distance has not been optimized yet and therefore the beam is not fully focused into the antenna's gap

3.3 Complete experimental setup

A schematic representation of the experimental setup for the time domain spectrometer can be found in Figure 3.7. The output pulse of the mode locked Ti:Sapphire

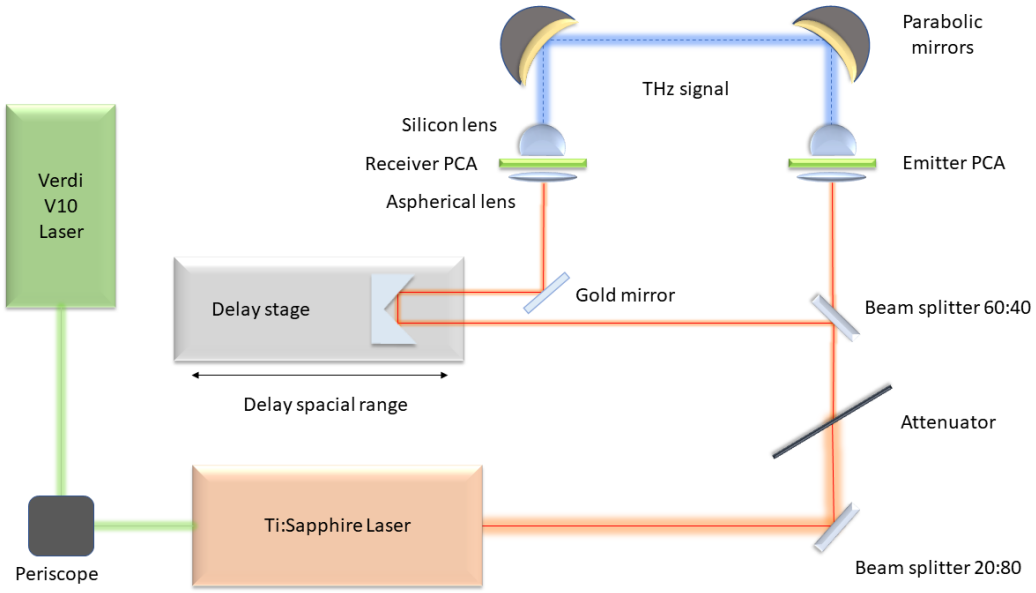

Figure 3.7: Schematic representation of the main components of the experimental spectrometer. The electronics for supply voltage modulation and data acquisition has not been represented.

laser has to be attenuated in order to comply with the specifications on maximum input optical power of the photoantennas. For this reason a pair of beam splitters and an attenuator are placed along the optical path. The first beam splitter (BSS11R, Thorlabs) filters out 80% of the $816nm$ radiation and the remaining pump radiation from the Verdi V10 laser. The variable attenuator is placed on the optical path to further reduce and regulate the optical power of the pulse. Eventually the second beam splitter (BSW11, Thorlabs) divides the incident radiation into two optical paths, one for the emitter and the other for the receiver antenna.

Radiation along the emitter path, which after the attenuation is reduced to ~ 4 mW, directly impinges on the first photoconductive antenna. Radiation reflected by the second beam splitter goes through a variable delay stage, which encompasses a square retro-reflecting hollow roof silver coated prism mirror (HRS1015-AG, Thorlabs) mounted on a movable sled (Newport PM500 series, Newport Corporation [77]) which is used to vary the optical path's length during the measurement process. Changing the delay between the pulses impinging on the photoantennas allows for a temporal scan of the generated THz signal. The sled can be either manually or electronically controlled, in the last case the maximum translation speed is limited to at most 5 mm/s but the spacial precision is greatly increased. After the delay stage a simple gold plated mirror is used to align the infrared radiation through the aspherical lens into the gap of the second photoantenna.

The THz radiation generated by the emitter PCA is firstly collimated and successively focused onto the receiver photoantenna by a pair of 90 degrees off axes gold coated parabolic mirrors (MPD249-M03, Thorlabs [78]). The two parabolic

mirrors have been mounted on a rigid support that can be moved along the direction perpendicular to the PCA plane in order to optimize the focusing effect of the mirrors. The whole system is initially pre-aligned using the infrared radiation from the Ti:Sapphire laser making use of an optical diffuser to simulate the divergence of the generated THz signal. Since the actual signal will then present a different divergence, the distance between the pair of mirrors and the photoantennas can be adjusted to maximise the intensity of the THz waves reaching the receiver.

In order to improve the final signal to noise ratio, the voltage applied to the emitter antenna's electrodes is modulated at 10 KHz and the uni-directional square wave is amplified to $30V$ before reaching the antenna. The signal acquired from the receiver photoantenna is demodulated and processed by means of a lock-in amplifier and sent to a digital data acquisition system (DAQ). The measurement process is managed by a Matlab application which controls both the movement of the sled and the flow of data from the DAQ. A picture of the optical table with the experimental setup of the spectrometer is reported in Figure 3.8

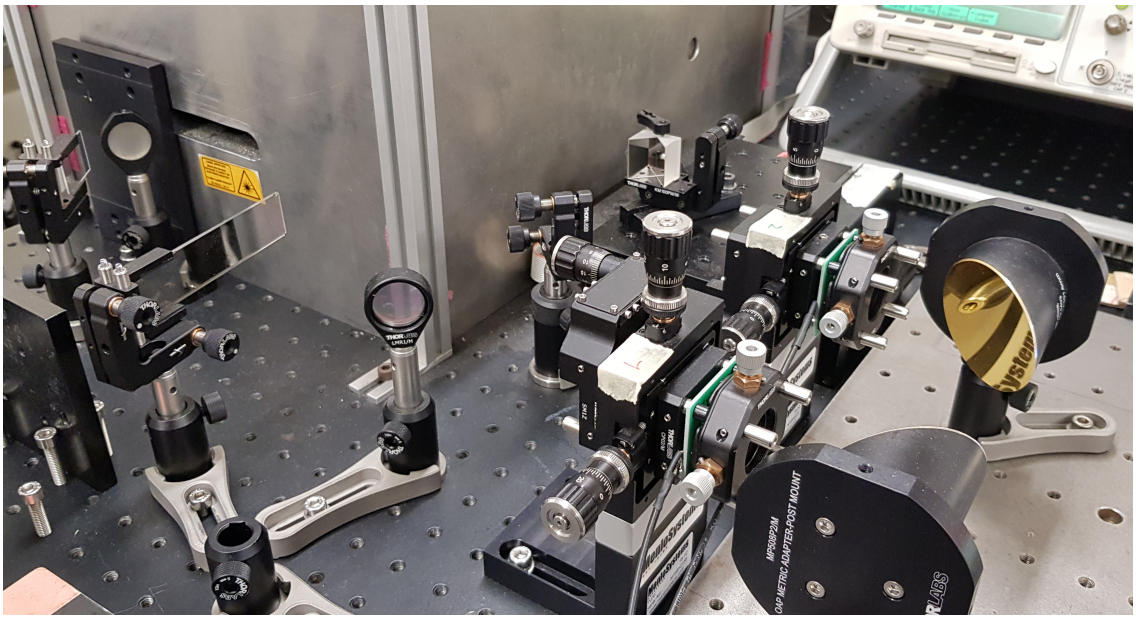

Figure 3.8: Picture of the experimental setup of the THz spectrometer

3.3.1 Measurement process

To perform a measurement of the time profile of the THz radiation, the prism mirror is moved at a constant speed while the demodulated signal from the receiver photoantenna is acquired from the DAQ. This procedure varies the delay between the emitted THz pulse and the narrow time window in which the receiver photoantenna is sensible to the THz radiation due to the excitation of photocarriers caused by the impinging infrared pulse. For a sufficiently broad scan of the sled a complete time profile of the THz signal can be retrieved.

In order to improve the signal to noise ratio a number of complete scans can be performed in the same experimental conditions, eventually averaging the resulting signals into a single measure. In ideal experimental conditions, the detected signal $x_k(t)$ of a generic k scan can be indeed expressed as the sum of the $x_0(t)$ noise

free signal from a time invariant system and the random noise normally distributed around zero:

$$x_k(t) = x_0(t) + n_k(t) \tag{3.2}$$

Averaging different $x_k(t)$ measures, the resulting signal $\langle x_k(t) \rangle$ will be composed by the time independent averages of the $\langle x_0(t) \rangle = x_0(t)$ signal from the time invariant system and the average of the noise measures, which for a large number of measures tends to the central value of the noise distribution $\langle n_k(t) \rangle \approx 0$. Therefore for an ideally large number of scans the averaged signal is given by:

$$\langle x_k(t) \rangle \approx x_0(t) \tag{3.3}$$

It is worth pointing out however that in experimental conditions not all the noise sources have a zero-centered distribution and the number of averages that can be applied is necessarily limited by time constraints and the stability of the measurement system condition. As a consequence the averaging procedure will not completely remove the noise, nevertheless it results in a tangible improvement in the signal to noise ratio, as illustrated in the next section.

3.4 Signal optimization

A significant portion of the experimental activity for this thesis work has been devoted to the optimization of the THz signal emitted and detected in standard experimental conditions by the pair of photoconductive antennas. A preliminary phase during the development of the spectrometer consisted in the study of the impact of several different experimental parameters on the quality of the acquired signal. A list of the most relevant of these parameters, as well as the values they were set on during the measures, can be found in table 3.4.

Table 3.4: Relevant experimental parameters with the standard values used for most of the measures (unless otherwise indicated).

Optical Pump power (800 nm)	~ 4 mW
Modulation voltage	$0 - 30$ V
Modulation frequency	10 KHz
Number of averages	100
Delay stage speed	2 mm/s
Lock-in integration time	1 ms
Lock-in sensibility	$1 \div 5$ mV
Delay scan range	2 cm

In the choice of the best acquisition configuration, the optimization effort has been focused towards the maximization of signal to noise ratio in the measured THz trace, in order to facilitate a cleaner extraction of the spectral features. For what concerns the intensity of the infrared pump beam impinging on the photoantennas, measures showed a positive correlation between the input optical power and the amplitude of detected peak of the THz pulse. For the majority of the measures, the optical pump power has been set to ~ 4 mW, a value that guarantees a reasonable

level of signal while still remaining well below the maximum tolerated value by the photoantennas. The modulation voltage applied to the first photoantenna has been chosen complying to the specification of the device while for the modulation frequency two distinct values where tested, nominally 1 KHz and 10 KHz, with the faster modulation showing a better overall quality of the signal.

According to the measurement process described in the previous section, several individual scans of the delay stage are performed and then averaged into a single final measure to improve the overall signal to noise ratio. The impact of this procedure on the noise level can be seen in Figure 3.9. It is sufficiently evident that increasing the

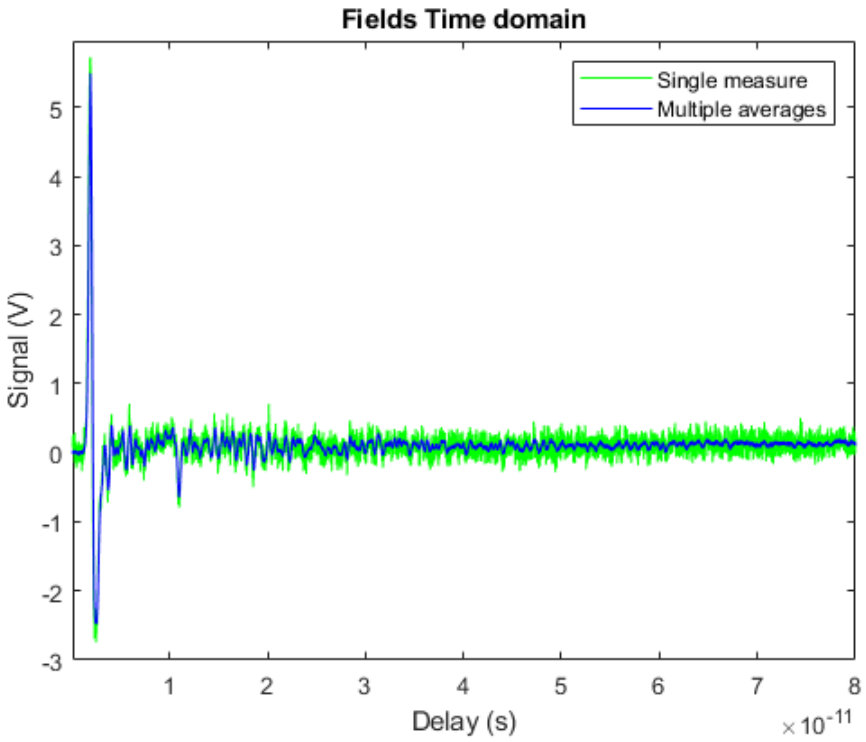

Figure 3.9: Measured THz-TDS traces in case of a single scan (green) and multiple scans averaged (blue)

amount of averages involved in a complete measure translates in an better overall quality of the signal. It is not worthwhile however to increase the number of averages beyond a certain amount because, in the face of a linear increase in time demanded to complete a measure, the improvement in noise reduction becomes less and less noticeable.

The lock-in integration time, i.e. the time interval in which the lock-in integrates the input signal before upgrading the output one, is another parameter having a major impact on the TDS measure. A longer integration time generally results in a less noisy measure, being the zero centered distributed noise partially removed by the integration process. Experimental conditions ought to remain unchanged during the whole integration interval, otherwise some relevant information about the pulse shape and amplitude could be filtered out and lost. For this reason the lock-in integration time has to be set taking in consideration the acquisition time per step, which is directly reflected in the speed of translation of the delay stage: a slow drift of the delay line allows for longer integration times and a better noise reduction but

results in longer measures, faster sliding of the delay line involves quicker measures but limits the integration time and thus the effectiveness of noise reduction. From a signal analysis point of view, the procedures of averaging multiple fast scans or setting a long integration time for the lock-in and performing a single measure should bring to similar results in ideal conditions for a the same amount of data points averaged. In real experimental conditions however there could be potential non idealities, such as inaccuracies in the movement of the delay stage or slow drifts in the experimental environment parameters, that differentiate the result obtained with the two measurement methods. In order to find out which of the two measurement processes is best fitted for the spectrometer under consideration, two complementary measures have been compared as shown in Figure 3.10. In the first measure a series

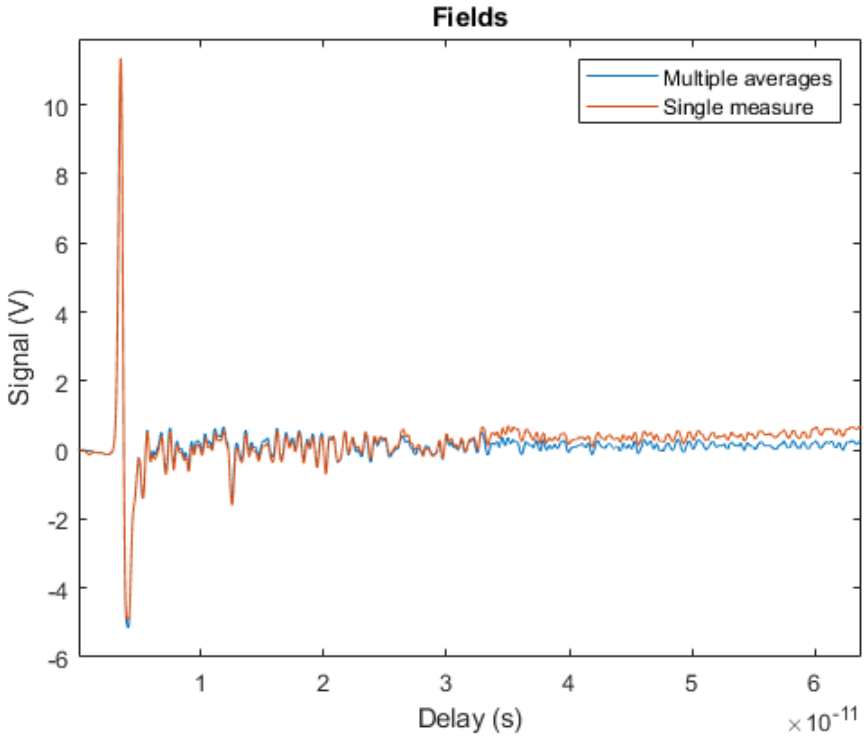

Figure 3.10: Measured THz-TDS traces in case of: (Blue) 100 scans each one with a 1 ms integration time and; (Orange) a single scan with a 100 ms integration time

of 100 scans were performed with a lock-in integration time of 1 ms and a delay line speed of 5 mm/s and then averaged. A second measure has successively been taken with a single slow scan of the delay line, $v_{delay-line} = 0.05$ mm/s, with a lock-in integration time of 100 ms. The two measures present analogous features around the main peak but the single slow scan is slightly more noisy and shows an increasing drift for larger delay times. This behaviour may reflect a constant slow drift in the experimental conditions which is better tolerated by the averaging process of the first measure.

The last experimental parameter worth of a more detailed discussion is the extension of the delay scan, i.e. the distance covered in a single sweep by the delay sled. This parameter has a major influence on the spectral information that can be extracted out of the acquired time domain trace. First, the scan has to be sufficiently wide to sample the entire signal, that means both the main THz peak and the

subsequent oscillations above the noise level, in order to collect the most complete information as possible on the material's response. Secondly, in ideal conditions, the sweep range directly determines the spectral resolution obtainable once the signal is transformed in its frequency spectrum:

$$\Delta f_{min} = \frac{c}{2L} \tag{3.4}$$

where L is the physical length of the mechanical delay line [79]. It is worth notice that even in the case of a noise free system with an infinite delay line the resolution would be ultimately limited by the pulse repetition rate of the pump laser. Nevertheless, in realistic experimental conditions, the actual spectral resolution turns out to be much poorer and ultimately limited by the signal to noise ratio in time domain. As the delay time is increases, the signal information gets progressively buried below the noise floor and after a certain threshold even a longer scan doesn't add any relevant information to the measure. This set the maximum spectral resolution typically achievable with this kind of spectrometers to the order of 1 GHz [80]. Thus in experimental practice the scan length has been limited to a value sufficient to cover the region of the signal with an appreciable signal to noise ratio. Limiting the scan range has also the not negligible advantage of fastening the whole measurement process.

It is not an uncommon practice to increase the apparent spectral resolution of measures that employ short scans by zero padding the signal, i.e., extending the time domain data vector by appending to it a string of null values. Zero padding forces the fast Fourier transform algorithm, used to extract the spectrum out of the time trace, to interpolate additional frequency data points, which results in an apparent better frequency resolution compared to the unprocessed data. It's important to point out that the null data points attached to the time signal carry no additional information but rather help the algorithm to interpolate more finely the existing ones. Nonetheless the zero padding works generally well, producing spectra that are very similar to the high resolution ones obtained with longer sweeps of the delay line. A relevant exception is represented by measured spectrum characterized by narrow-frequency features that are not detected with the short scan and thus can't be recovered even with a zero padding. An example of the effectiveness of this technique is shown in Figure 3.11 which represents a detail of the spectrum of the THz signal obtained with a short scan, a long scan and the same short scan with zero padding. It is worth noting in Figure 3.11 the coincidence of all points in the spectrum of the unpadded short measure with those of the padded spectrum, with the latter containing also additional points that refine the spectral profile. The padded signal is indeed much more similar to the long scan than the short one. Nevertheless, the padded spectrum does not entirely succeed in reproducing the detailed long-scan spectrum, in 3.11a indeed the shape of the peak is accurate but its magnitude is underestimated while in 3.11b the padding even fails to recover the exact peak profile.

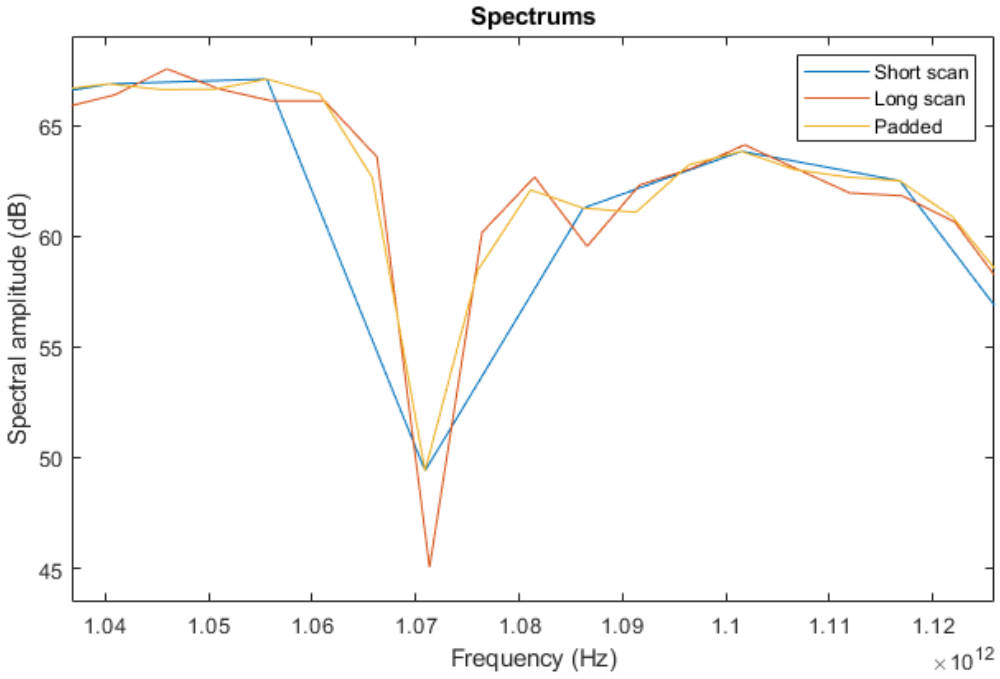

(a)

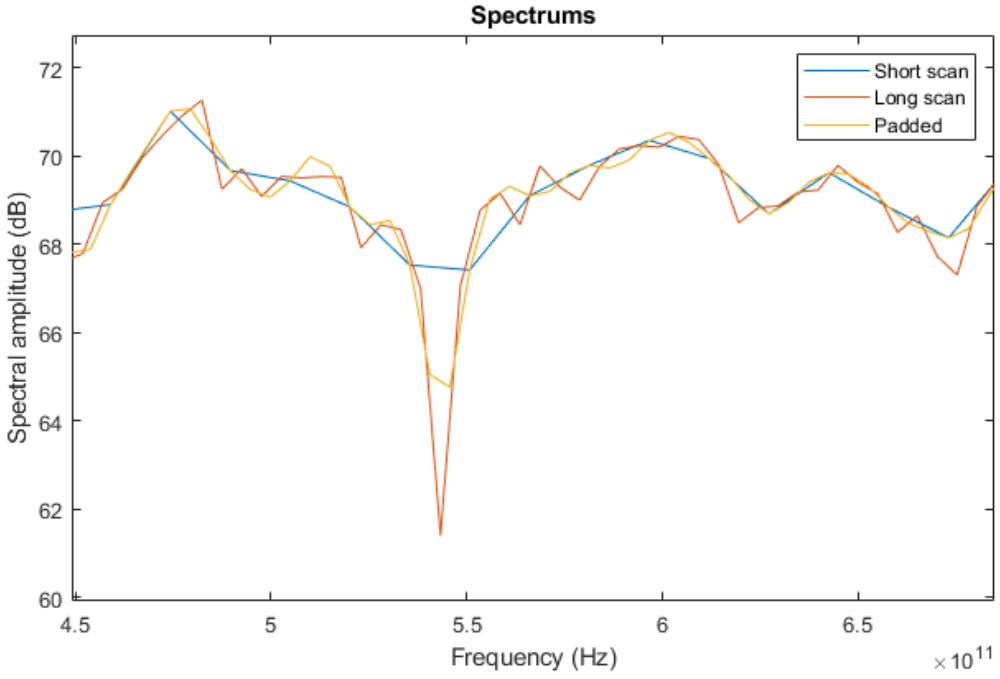

(b)

Figure 3.11: Close up view of water absorption peaks in the spectrum of the THz signal. The long scan has a range of 3 cm, the short one of 1 cm, the zero padding extends the time signal of the short measure to the same number of data points of the long measure. In both figures the narrow peak is better resolved by the zero padded signal with respect to the short scan.

Chapter 4

Spectroscopy Results

As discussed in the previous chapters, THz-TDS is quite unique among the spectroscopy techniques in its way of measurement, being the signal directly sampled in time domain by means of a pump-probe configuration driven by an ultrafast laser. Nevertheless, most of the meaningful optical properties of the materials studied with this kind of spectrometers, as well as the most relevant parameters used to characterize the performance of these devices, are frequency dependent. As a consequence a series of signal processing techniques are generally applied to the acquired time domain raw data in order to extract meaningful insights on the frequency domain characteristics of the detected field.

This chapter deals with the characterization of the emitted THz signal and its implementation to study relevant parameters of some illustrative samples. Some of the most relevant characteristics of the spectrometer are analyzed in the first section, such as measured profile of the time domain signal, THz spectral amplitude, signal bandwidth and spectral resolution.

In the second section, the spectrometer is employed to study the optical properties of a set of materials in the THz region. First a simplified theoretical model to retrieve characteristic optical parameters, nominally refractive index and absorption coefficient, of a generic sample from its transmission mode measurements is presented. Subsequently the model is tested and validated on some measures of paper and plastic samples. The spectrometer is then used to characterize the refractive index of a Gallium Phosphide crystal, a material used inter alia for THz generation by optical rectification process. At last the measures of refractive index and absorption coefficient for different types of edibles oils are carried out and compared to the available literature.

4.1 Characterization of the THz signal

Time domain signal A close up view of the reference signal of the THz pulse acquired with the experimental setup described in chapter 3 is shown in Figure 4.1 all along with the noise floor. This latter has been detected in the same experimental conditions of the reference signal, while blocking the THz propagation with an opaque metallic slab placed in between the two parabolic mirrors.

The main THz pulse is clearly visible in the graph at a delay between zero and 5 ps where the pulse peak stands out at $\sim$ 5 V with a lock-in sensitivity set to 2 mV. Pulse duration is about 2 ps, which is in line with the values specified by the

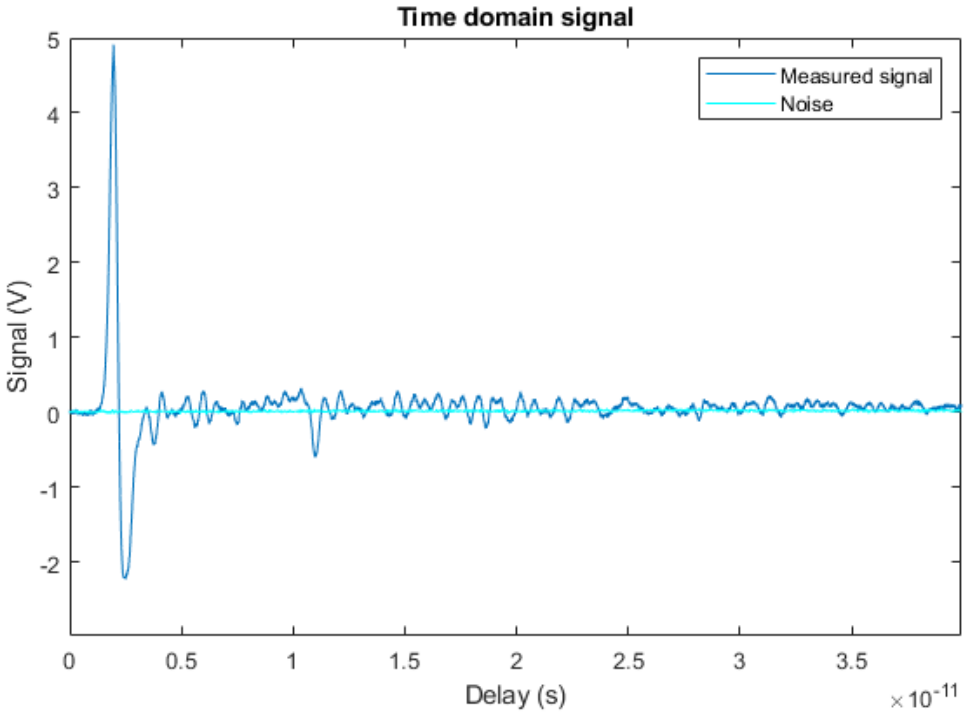

Figure 4.1: Enlarged view of the THz pulse time trace (blue) detected by the receiver photoantenna, noise floor (cyan) is also reported. Measure parameters as reported in Table 3.4

producer. The negative peak which stands out on the weaker oscillations between 10 and 13 ps shows a certain degree of resemblance with the descending tail of the main THz peak, this induces to believe that the smaller peak could be generated by a weaker replica of the main pulse due to reflection by a component along the optical path.

The series of oscillations detected after the main peak is traceable to the presence of atmospheric gases, in particular water vapour, that are optically active in the THz region. Rotational states of water vapor molecules are indeed narrowly separated, thus being characterized by transition in resonance with the energy of a THz photon. These resonances are responsible for the oscillations observed after the main THz peak in the detected signal. In fact, in spectrometers equipped with vacuum systems on the THz path, none of these oscillations is observed. Having the THz radiation propagating through air has two major drawbacks on the final signal quality. The first one is a general attenuation in the signal amplitude in time domain due to water vapour absorption. A second disadvantage, in view of applications in spectroscopic material analysis, is the presence of water absorption peaks in the spectrum of the THz signal, which is likely to cause artifacts in the retrieved frequency dependent optical parameters.

Signal to noise ratio Taking into account that different methods of representing the signal to noise ratio in TDS systems can be found in the literature, the choice of this work is to apply the definition used in references [79, 81], in which the SNR

of a measure obtained averaging multiple scans is expressed as:

$$SNR = \frac{\overline{E}}{s_E} \tag{4.1}$$

where $\overline{E}$ is the mean magnitude of the amplitude, i.e. the value of the averaged signal, whilst s_E is the corresponding amplitude standard deviation in the n scans used to obtain the averaged signal.

Signal to noise ratio of the measured field is represented in Figure 4.2 along with the averaged time domain trace of the signal and its standard deviation. It

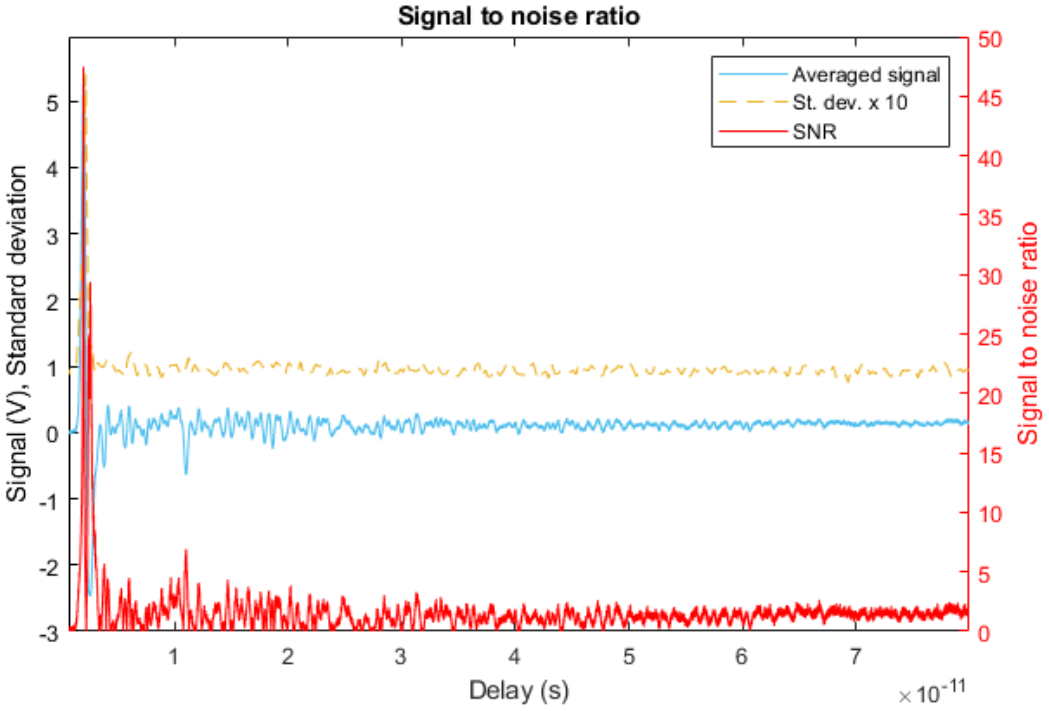

Figure 4.2: Signal to noise ratio (red) for the detected signal calculated according to equation 4.1. The reference signal (blue) and its standard deviation (yellow) are obtained by averaging 100 individual scans. Standard deviation is represented with a $10X$ amplification factor to facilitate data visualization.

is seen that the standard deviation is highly correlated with the signal amplitude, being larger where the signal is stronger. The TDS-SNR strong fluctuations from point to point make it as a whole a poor indicator for the accuracy and resolution of different measures. A more comparable indication of the time domain SNR, and also a commonly accepted practice, is to consider just the ratio between the main signal peak and the standard deviation of its value, which for the measured signal is $SNR_{peak} = 47.5$

Signal spectrum The magnitude of the discrete Fourier transform of the measured signal is represented in Figure 4.3 against the spectral content of the noise floor measured blocking the THz radiation. The spectrum has been obtained through a Fast Fourier Transform (FFT) algorithm, using a uniform rectangular window on the time domain data.

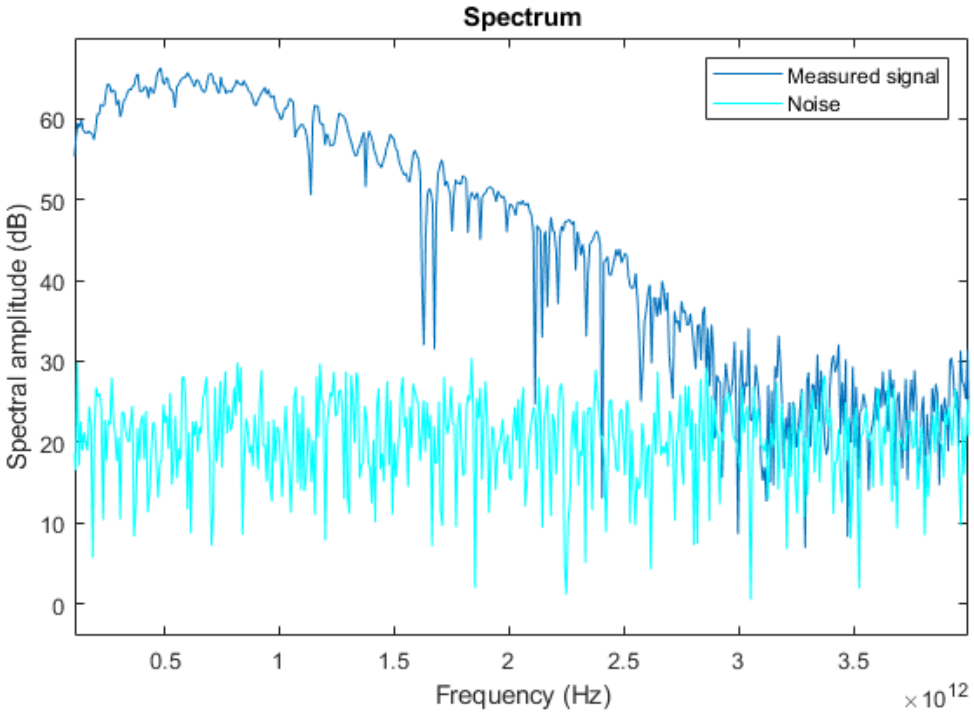

Figure 4.3: Measured signal (blue) and noise floor (cyan) spectral amplitudes up to 4 THz. Measurement parameters as reported in table 3.4

The spectral amplitude of the THz signal has its maximum plateau between 0.5 and 1 THz, then progressively decreases and is eventually buried in the noise floor. Because of the propagation through room atmosphere, the available signal bandwidth is narrower than the one indicated in the photoantennas specifications, nevertheless up to 3 THz the signal contribute is clearly distinguishable from the noise floor. The effect of water absorption is in this case evident in the presence of many narrow absorption peaks from 0.5 THz up to the edge of the available bandwidth. The spectral resolution is sufficient to distinguish the closely spaced absorption peaks between 2 and 2.25 THz and is estimated to be approximately $\Delta f_{min} \approx 7.5$ GHZ, on the basis of equation 3.4.

Dynamic Range Another important parameter used to characterize the performance of a spectrometer is represented by its dynamic range. In contrast to the SNR, which indicates the minimum detectable signal, the dynamic range is a measure of the maximum quantifiable signal change. Two specific aspects have to be considered concerning the dynamic range of a THz-TDS: The first is that the dynamic range of spectral data is strongly frequency dependent, steeply decreasing for increasing frequencies; Second, no simple analytical relationship subsists between the dynamic range of time domain data and that of the corresponding spectra and generally the two quantities can differ by orders of magnitude. Given that data are acquired as time domain traces whereas optical parameters of interest are derived from the spectra of the measurements, it is important to specify to which domain the dynamic range of a certain system is referred. The dynamic range is defined as the ratio between the largest and the smallest measurable signal, in practical terms it can be expressed as [81]:

$$DR = \frac{E_{max}}{N_{rms}} \tag{4.2}$$

where DR denotes the dynamic range, E_{max} the maximum signal amplitude, and N_{rms} the root-mean-square value of the noise floor.

The dynamic range of the measured signal is represented in Figure 4.4. It is

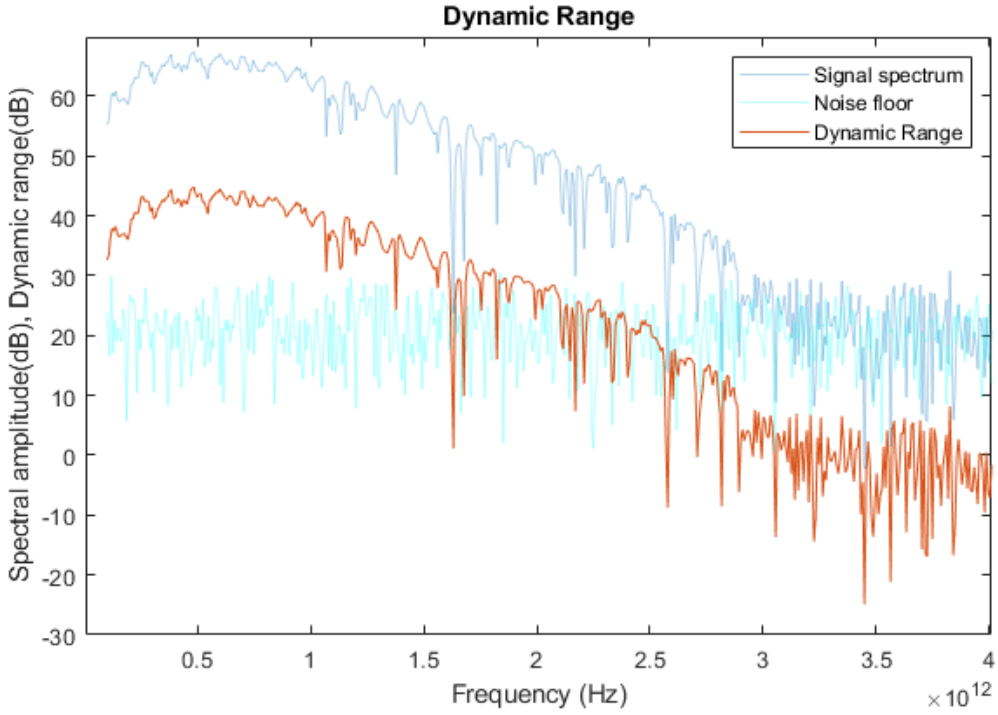

Figure 4.4: Dynamic range of the detected signal calculated according to equation 4.2. Signal spectrum and noise floor are also represented as references.

evident how the dynamic range of THz-TDS in the frequency domain follows the spectral profile of its signal amplitude. As with SNR, it is a widely accepted practice to quote the maximum value in the frequency range of interest as the dynamic range of THz-TDS, in this case $DR_{max} = 350,74$.

4.2 Material Characterization in Transmission-Mode

After the characterization of the reference signal, the THz spectrometer under consideration has been employed to study the optical parameters of different samples. In particular, the ability of TDS of detecting both amplitude and phase of the THz field allows to estimate the complex refractive index of the sample as well as its frequency dependent absorption coefficient in the THz range. In this section the theoretical model used to retrieve the refractive index from the detected field is initially discussed and subsequently applied to the analysis of the measurements of the THz signal acquired in transmission mode for different samples.

4.2.1 Theoretical model for refractive index measurement

The following model, presented in [79], is a simplified version of the iterative method firstly introduced by Duvillaret et al. [82], which relates amplitude and phase changes in a measured THz-TDS signal to the optical properties of the considered sample.

Assume to model the sample as a homogeneous dielectric slab, with complex refractive index $\tilde{n}_s(\omega) = n_s(\omega) + jk_s(\omega)$ and thickness l, onto which the THz field, considered as a plane wave, impinges at normal incidence. Reflections at the interfaces between the two sample surfaces and free space result in multiple propagation paths in the dielectric slab. In general, the field detected after the transmission through the sample can be expressed as a summation of the contribution from all the optical paths:

$$E_t(\omega) = tt' \cdot \exp\left[-j\tilde{n}_s(\omega)\frac{\omega l}{c}\right] \cdot \mathbf{FP}(\omega) \cdot E_0(\omega) \tag{4.3}$$

where $t = 2/(1+\tilde{n}_s)$ and $t' = 2\tilde{n}_s/(1+\tilde{n}_s)$ are the transmission coefficients respectively for air-sample and sample-air interfaces; $\mathbf{FP}(\omega)$ is the Fabry-Pérot term which represents the effect of the multiple reflections inside the sample, given by:

$$\begin{aligned}\mathbf{FP}(\omega) &= \left\{1 + \rho'^2 \cdot \exp\left[-2j\tilde{n}_s(\omega)\frac{\omega l}{c}\right] + \rho'^4 \cdot \exp\left[-4j\tilde{n}_s(\omega)\frac{\omega l}{c}\right] + ...\right\} \\ &= \sum_{m=0}^{\infty}\left\{\rho'^2 \cdot \exp\left[-2j\tilde{n}_s(\omega)\frac{\omega l}{c}\right]\right\}^m \\ &= \left\{1 - \rho'^2 \cdot \exp\left[-2j\tilde{n}_s(\omega)\frac{\omega l}{c}\right]\right\}^{-1}\end{aligned} \tag{4.4}$$

with $\rho' = (\tilde{n}_s - 1)/(\tilde{n}_s + 1)$ transmission coefficient of the sample slab.

For the sake of simplicity, in the following it is assumed that $\mathbf{FP}(\omega) = 1$ considering only the first directly transmitted THz pulse. This is reasonable in a first approximation, since the contributions arising from multiple reflections taking place inside the sample are of much weaker entity that the first main transmitted pulse. The approximation is particularly well suited for optically thick samples, in which the echoes of the terahertz pulse are well separated in time. In this case it is also possible to apply a temporal window to select only the first transmitted pulse. It follows that the simplified terahertz signal being transmitted through a dielectric sample with parallel surfaces at a normal angle of incidence can be expressed as:

$$E_{sam}(\omega) = \eta\frac{4\tilde{n}_s(\omega)}{\left[\tilde{n}_s + 1\right]^2} \cdot \exp\left[-j\tilde{n}_s(\omega)\frac{\omega l}{c}\right] \cdot E_0(\omega) \tag{4.5}$$

where η is the transmission factor of the media surrounding the sample.

The complex frequency spectrum of the reference signal, obtained from a measure of the THz pulse free propagating from the emitter photoantenna to the receiver in the same experimental conditions, is in contrast given by:

$$E_{ref}(\omega) = \eta \cdot \exp\left[-j\frac{\omega l}{c}\right] \cdot E_0(\omega) \tag{4.6}$$

Both E_{sam} and E_{ref} can be directly obtained as Fourier transform of the time domain measurements. The complex transfer function of the sample in the frequency domain $H(\omega)$ is given by the ratio between the spectrum gathered with the sample and the one of the free propagating pulse:

$$\begin{aligned} H_0(\omega) &= \frac{4\tilde{n}_s(\omega)}{[\tilde{n}_s+1]^2} \cdot \exp\left\{-k_s(\omega)\frac{\omega l}{c}\right\} \cdot \exp\left\{-j[n_s(\omega)-1]\frac{\omega l}{c}\right\} \\ &\approx \frac{4n_s(\omega)}{[n_s+1]^2} \cdot \exp\left\{-k_s(\omega)\frac{\omega l}{c}\right\} \cdot \exp\left\{-j[n_s(\omega)-1]\frac{\omega l}{c}\right\} \end{aligned} \tag{4.7}$$

where the complex refractive index in the Fresnel coefficients has been approximated by its real part:

$$\tilde{n}_(\omega) = n_s(\omega) + jk_s(\omega) \approx n_s(\omega) \tag{4.8}$$

Taking the argument and logarithm of the simplified transfer function gives respectively:

$$\angle H(\omega) = -[n_s(\omega)-1]\frac{\omega l}{c} \tag{4.9a}$$

$$ln|H(\omega)| = ln\left[\frac{4n_s(\omega)}{[n_s+1]^2}\right] - k_s(\omega)\frac{\omega l}{c} \tag{4.9b}$$

The real part of the complex refractive index $n_s(\omega)$ and the extinction coefficient $k_s(\omega)$ can be derived from the equations above as:

$$n_s(\omega) = 1 - \frac{c}{\omega l}\angle H(\omega) \tag{4.10a}$$

$$k_s(\omega) = \frac{c}{\omega l}\left\{ln\left[\frac{4n_s(\omega)}{[n_s+1]^2}\right] - ln|H(\omega)|\right\} \tag{4.10b}$$

Furthermore, the absorption coefficient of the sample is directly related to the extinction coefficient:

$$\alpha_s(\omega) = 2\frac{\omega k_s(\omega)}{c} \approx -\frac{2}{l}ln|H(\omega)| \tag{4.11}$$

Particular attention has to be paid when calculating the argument of the transfer function $\angle H(\omega)$. The phase directly obtained from the angle between real and imaginary parts of the transfer function is wrapped around the values $-\pi$ and π because of the shape of arctan function. This results in discontinuous jumps of polarity whenever the absolute value of the calculated phase angle is greater than π. An example of wrapping in the phase spectrum of the measured transfer function of a Gallium Phosphide crystal sample is illustrated in Figure 4.5.

The discontinuity artefacts deriving from wrapping mechanism in the phase spectrum are extremely detrimental in the retrieval of optical parameters. Therefore, in order to obtain meaningful insights on the optical properties of the measured sample, this kind of artifacts have to be removed in the signal processing stage. A standard approach in this sense consists in resolving the wrapped phase by adding or subtracting to the phase spectrum multiples of 2π in order to smooth the phase discontinuities, the unwrapped phase can then be expressed as:

$$\phi(\omega) = \angle(\omega) - 2\pi M(\omega) \tag{4.12}$$

where $M(\omega)$ is the integer number of frequency discontinuities from zero to ω in the wrapped phase spectrum.

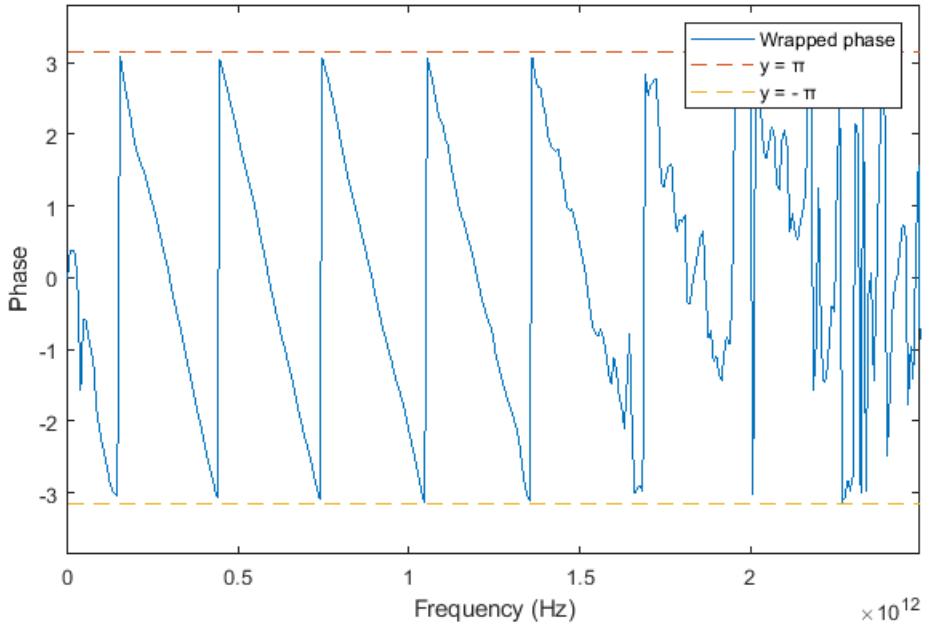

Figure 4.5: Example of phase wrapping in the phase spectrum obtained from the measure of a Gallium Phosphide crystal sample.

4.2.2 Plastic and paper

The first spectroscopic measurements were performed on samples of paper and plastic, with the aim of testing the capability of the spectrometer to discriminate between different materials and characterize the spectral response of the two samples in the THz region. A simple piece of white drawing paper of thickness 0.19 mm, slightly heavier than common printing paper sheets, has been chosen for the first of the two samples. The second sample was a slab of black plastic 1.70 mm thick, of the type used in protective cases for electronic devices.

A measure of the THz field with no sample was initially acquired in order to be used as reference signal in the optical parameters calculation. Successively the two transmission-mode measures were performed placing the sample in front of the silicon lens of the receiver photoantenna, right where the THz field is focused by the second parabolic mirror, with the same experimental conditions of the reference measure.

The time trace of the measured THz signal for the three measures is shown in Figure 4.6 together with the noise floor acquired blocking the THz radiation. A preliminary analysis of the samples optical characteristics can be carried out by comparing peaks positions and amplitudes of the three acquired signals. First, in both measures with plastic and paper the peaks are delayed in time with respect to the reference measure. This is symptomatic of an increased optical path length due to the passage of signal through a media characterized by a refractive index higher than the one of air. Peak delay is larger for the passage through the plastic sample than through the paper one, this is clearly due to the larger thickness of the first sample but could also indicate a higher medium refractive index. It can be also noted a similar attenuation in the maximum signal amplitude for both samples which, given the larger thickness of plastic, induces to expect a larger absorption

coefficient in the paper sample.

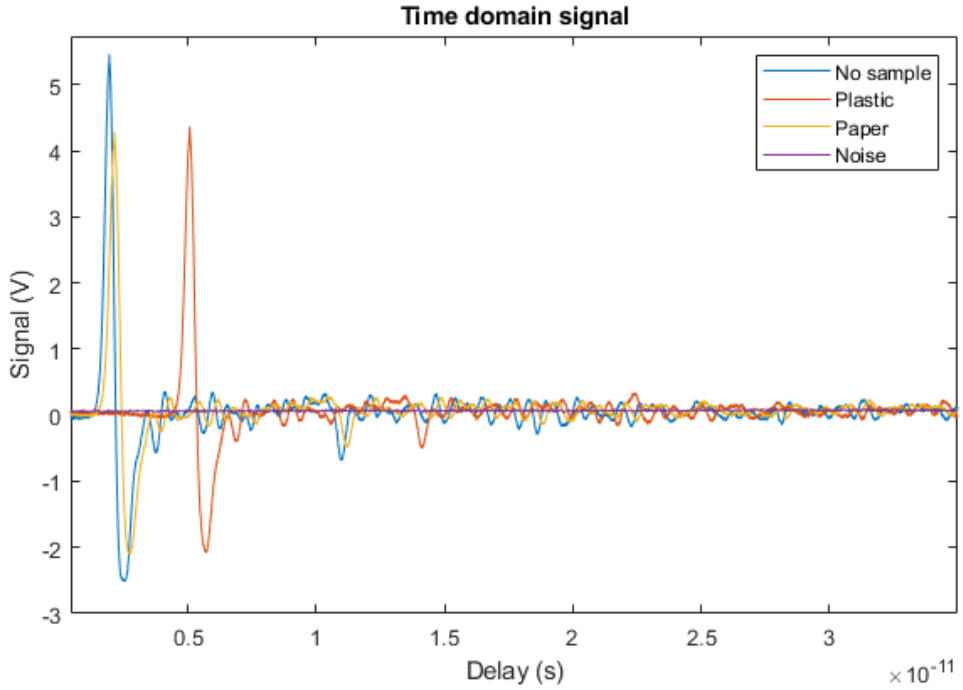

Figure 4.6: Time trace of the measured THz signal for: (blue) Reference measure with no sample; (red) Plastic sample; (yellow) Paper sample. The noise floor is represented as well.

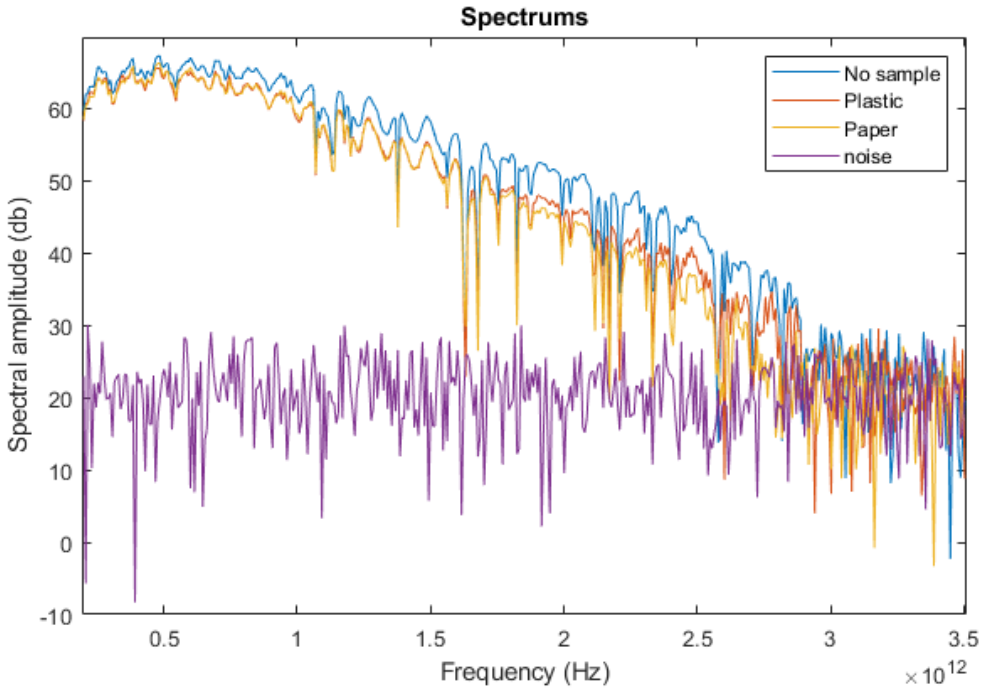

Figure 4.7: Calculated spectra of the measured THz signal for: (blue) Reference measure with no sample; (orange) Plastic sample; (yellow) Paper sample. The noise floor is represented as well.

Calculated spectrum for the three signals is represented in Figure 4.7. Except for a generalized attenuation in the spectral amplitude, no significant difference is appreciable between the different spectra, thus highlighting the absence of specific fingerprint features in the THz region for both plastic and paper. Moreover, in spite of material absorption there seems to be no significant reduction in the available bandwidth for the signal transmitted through the plastic sample whilst for the paper one the effective bandwidth is reduced to approximately 2.6 THz due to a combination of general attenuation and the presence of water vapour absorption lines.

In Figure 4.8 are represented the real parts of the refractive indexes of the two samples, calculated as discussed in the previous section. As expected, refractive index of plastic is generally higher than the one of paper, which causes the larger pulse peak shift in time domain signals. The difference in signal bandwidth is also clearly visible at high frequencies, with plastic refractive index that is correctly estimated up to 3 THz, while for the paper sample the calculated refractive index is generally noisier and starts to show strong oscillations beyond 2.6 THz. The small localized peaks present in both the calculated parameters, for instance the one at $\sim$ 1.6 THz, are actually artifacts due to the presence of water vapour absorption lines in the signal spectrum.

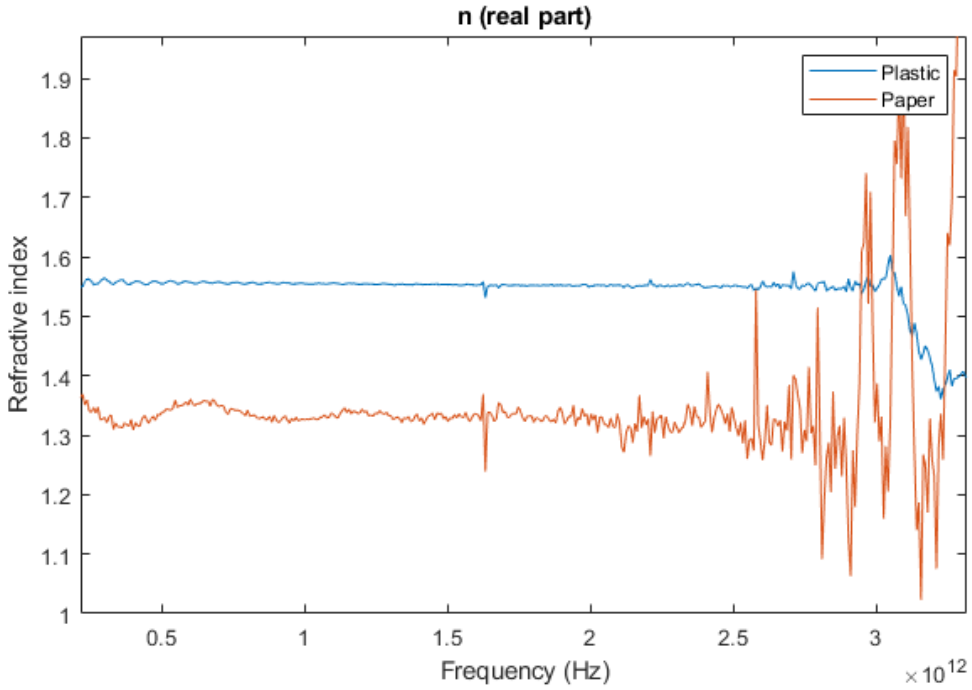

Figure 4.8: Refractive index, calculated as in equation 4.10a, for (blue) Plastic sample and (orange) Paper sample.

The absorption coefficient of the two samples has been calculated as described in equation 4.11 and is represented in Figure 4.9. The most evident element in the graph is the larger slope and magnitude of the absorption coefficient of the paper sample with respect to plastic, to such an extent that it has been necessary to use two different scales to accommodate both characteristics into a single graph. Another interesting particular is that the slope of the absorption coefficient of paper slightly increases for higher frequencies. This behaviour can be observed also in

the spectrum, Figure 4.7, where the attenuation of the paper signal is initially comparable to the one of plastic up to 1.6 THz, but sharply increases at higher frequencies.

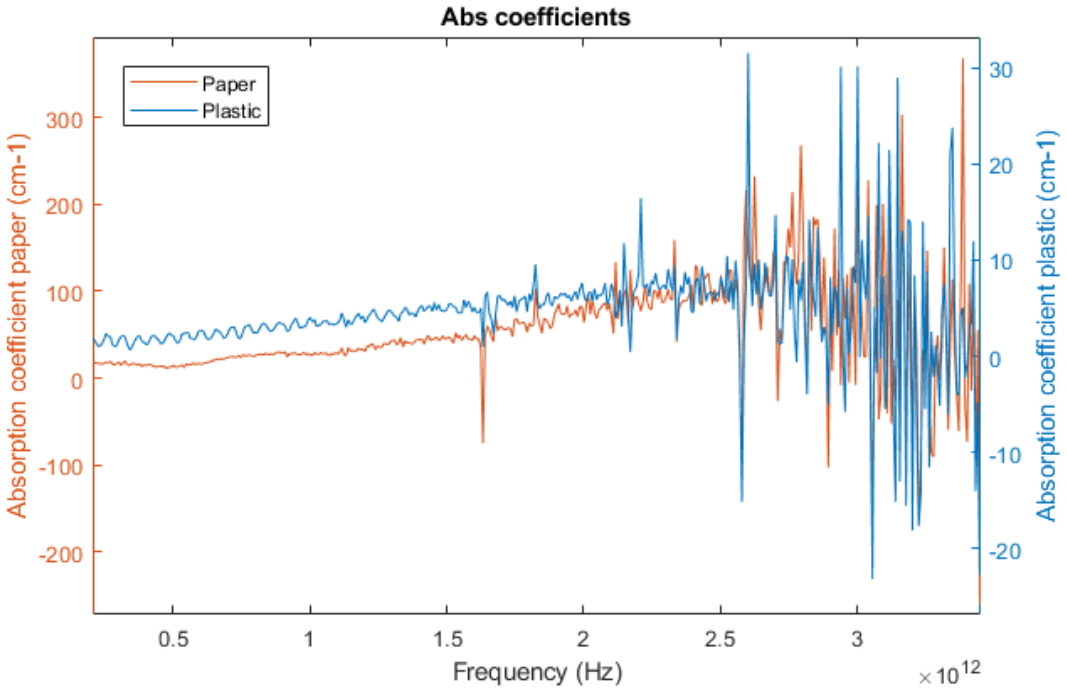

Figure 4.9: Calculated absorbtion coefficient for: (blue) Plastic and (orange) Paper samples.

It is also worth noting that the calculated absorption coefficient shows a more or less linear behaviour, aside for the water vapour induced artifacts, only up to roughly 2.5 THz even in the case of the plastic sample. This limitation is directly related to the frequency dependence of the dynamic range of the measure. Inspection of equation 4.11 and 4.10b shows that the largest absorption coefficient that can be measured reliably with a given DR corresponds to the situation where the sample signal is attenuated to a level equal to the noise floor, as initially pointed out by Jepsen and Fischer in [83]. This largest measurable absorption coefficient can be expressed as:

$$\alpha_{max}(\omega)l = 2ln\left[DR(\omega)\frac{4n_s(\omega)}{(n_s(\omega)+1)^2}\right] \tag{4.13}$$

What happens in the case the absorption coefficient exceeds α_{max} is that the analysis will show an apparent absorption coefficient equal to α_{max}. In transmission THz-TDS the measurement of the refractive index is not subject to the same principal limitations as the measurement of the absorption coefficient, that is the reason why refractive index of the plastic sample is correctly retrieved up to almost 3 THz. In Figure 4.10 it is shown the frequency dependence of the maximum measurable absorption coefficient for the plastic sample measure. From the peak of the spectrum, at roughly 0.5 THz, the α_{max} decreases in an almost linear fashion until cutoff frequency, in this case around 2.5 THz. Above this frequency the algorithm fails to retrieve a realistic absorption coefficient.

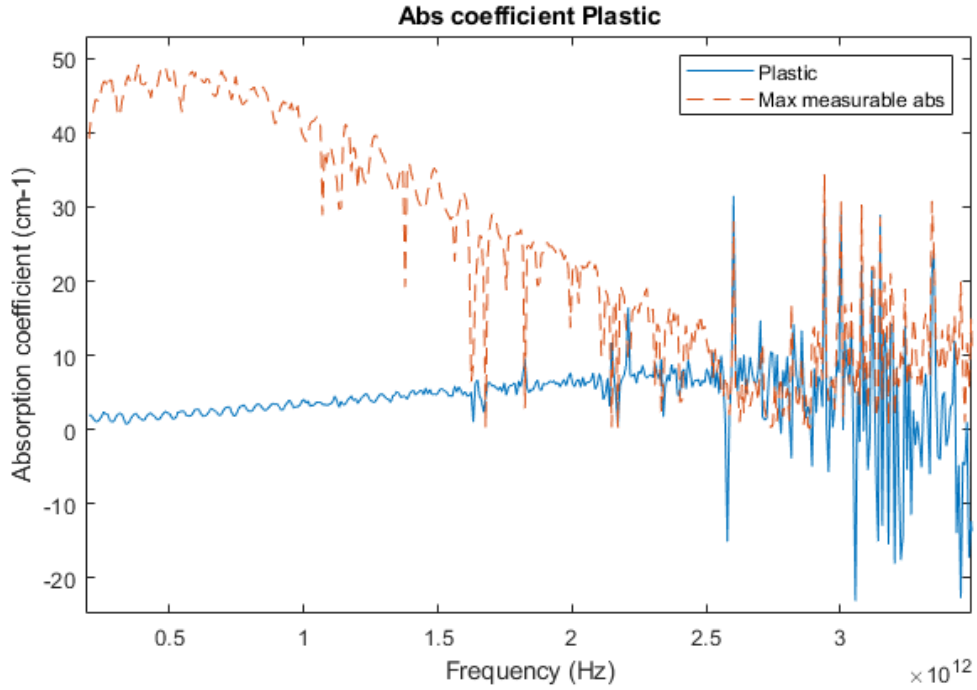

Figure 4.10: Plastic absorption coefficient (blue) with upper limit of the detectable absorption (orange).

Finally, it is worth to investigate more in detail the oscillating trend present in the absorption coefficient, especially of the plastic sample, up to 1.5 THz. These almost periodic oscillations induces to think at the effect of some kind of multiple reflections, either in the experimental setup or in the material itself in the form of the Fabry-Pérot effect discussed in the previous section. A viable way to remove these oscillations from the final measurements could be to apply a temporal window to the signal in such a way to eliminate, or at least reduce, the effect of pulse replicas. Two examples of windows of this type are represented in Figure 4.11. The two windows used to test the effectiveness of temporal windowing were based on Hann functions of width respectively 30 ps and 10 ps. The choice of an Hann shaped window has been suggested by the results of the study on different windows in THz signal processing carried out in [84]. The application of temporal windowing resulted in a general smoothing of the THz spectrum, with clear effects also on the absorption coefficient. As shown in Figure 4.12, the oscillations in the absorption coefficient are progressively filtered out as the temporal duration of the window is decreased and the whole α parameter follows a more linear pattern. In particular the oscillations seem to be completely removed as long as the small replica of the main pulse, of the same kind of the one noted during the characterization of the signal and thus probably due to some reflection along the optical path, is filtered out.

Nevertheless this smoothing comes at the cost of poorer spectral resolution and of a general loss of information in the signal spectrum. The first drawback, the deterioration in spectral resolution, is a direct consequence of the shortening of the windowed signal with respect to the original one, as pointed out in equation 3.4. The second downside of time windowing is that, along with pulse replicas, it removes part of the oscillations in the time domain signal which contain essential information

on the response of the media to the THz pulse.

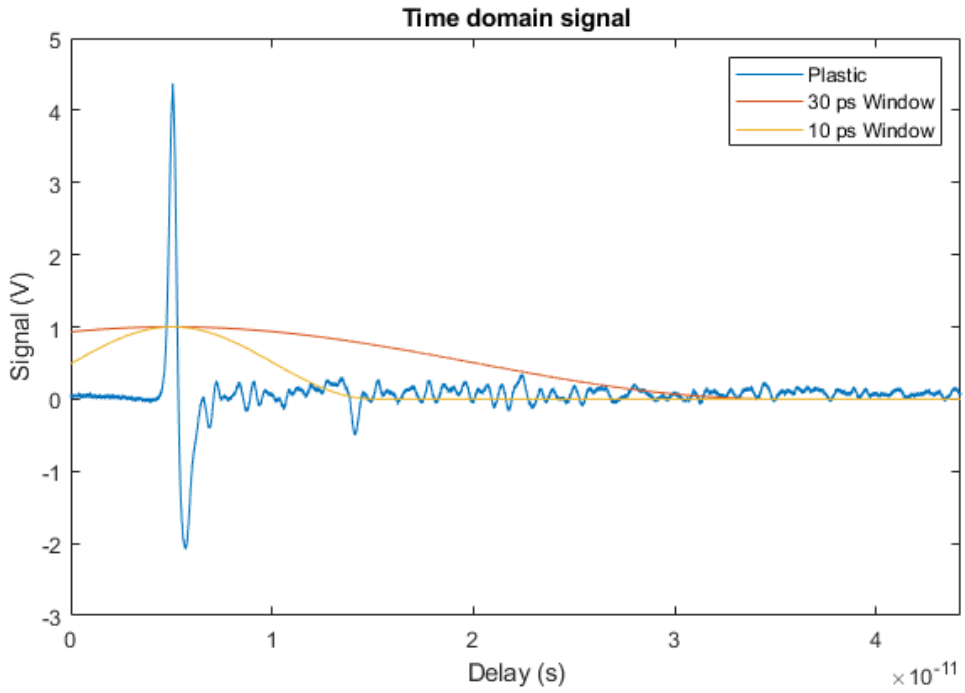

Figure 4.11: Time trace of the detected THz field for the plastic sample and applied temporal windows.

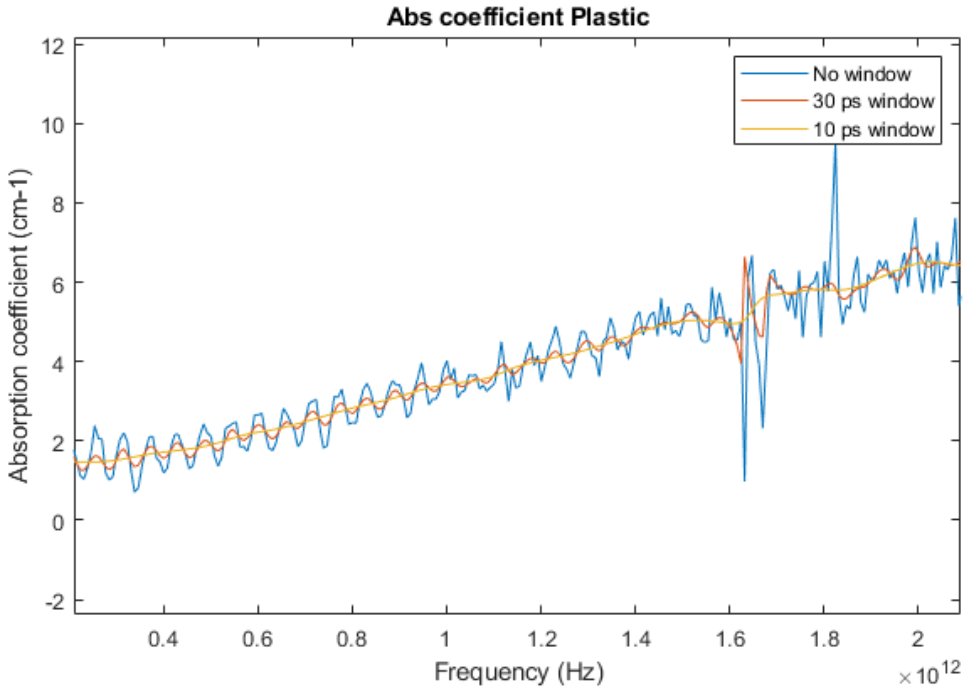

Figure 4.12: Effect of different temporal windows on the calculation of the absorption coefficient of plastic: (red) Hann window, 10 ps width; (yellow) Hann window, 30 ps width; (blue) measured signal, no windowing.

4.2.3 Gallium Phosphide crystal

Gallium Phosphide (GaP) is a compound semiconductor material which has various applications in optical systems. One of the most widespread implementation of GaP is in the production of efficient red, orange and green light-emitting-diodes (LEDs) due to its transparency to yellow and red light. GaP crystals are also appreciated as active materials for non linear optical rectification processes due to the large bandwidth in the THz region. In general, the three material parameters used to describe radiation generation in optical rectification processes are the refractive indices of GaP in optical and THz frequency ranges and the crystal thickness [85]. In light of these elements it seemed interesting to characterize the behaviour of GaP refractive index in the THz region.

Gap refractive index is known to vary between 3.2 and 5 across the THz to visible wavelengths, which is higher than most of other semiconductor materials. A theoretical model for the refractive index in the THz frequency range is discussed in [86] in which the refractive index is modeled as a Lorentzian oscillator:

$$n(\Omega) = \sqrt{\epsilon(\Omega)} = \sqrt{\epsilon_\infty + \frac{\epsilon_\infty(\omega_{LO}^2 + \omega_{TO}^2)}{\omega_{TO}^2 - \Omega^2 + j\Gamma\Omega}} \tag{4.14}$$

where ϵ_∞ is the high frequency dielectric constant, ω_{LO} and ω_{TO} are the longitudinal and transversal optical phonon frequencies, Γ is the phonon damping rate and Ω is the THz angular frequency. The experimental values for GaP parameters are listed in table 4.1

Table 4.1: Relevant experimental parameters of GaP crystal [87]

Parameter		**Value**
High frequency dielectric constant	ϵ_∞	9.075 mW
Longitudinal phonon frequency	Ω_{LO}	$2\pi \cdot 12.082$ THz
Transversal phonon frequency	Ω_{TO}	$2\pi \cdot 11.011$ THz
Phonon damping rate	Γ	$2\pi \cdot 0.129$ THz
Thickness	l	500 μm

The real part of the refractive index based on the theoretical model, as calculated from equation 4.14, is represented in Figure 4.13. In order to formulate an experimental estimate of the refractive index of GaP, the two measurements of the transmitted THz field with and without the sample were performed as in the paper and plastic case.

A complication in these measurements was represented by the lower signal to noise ratio, due to the strong absorption of the THz signal in the GaP sample. The low signal to noise ratio, especially in the lower frequencies region of the spectrum ($f < 0.2$ THz), plagues the magnitude and phase data and can introduce discontinuities in the phase of the transmission function even when standard phase unwrapping is applied. Moreover, unwrapping the phase starting from the noisy signal at low frequencies causes errors that are incrementally propagated to phase at increasing frequencies, as represented in Figure 4.14, with evident detrimental effects on the estimation of optical parameters.

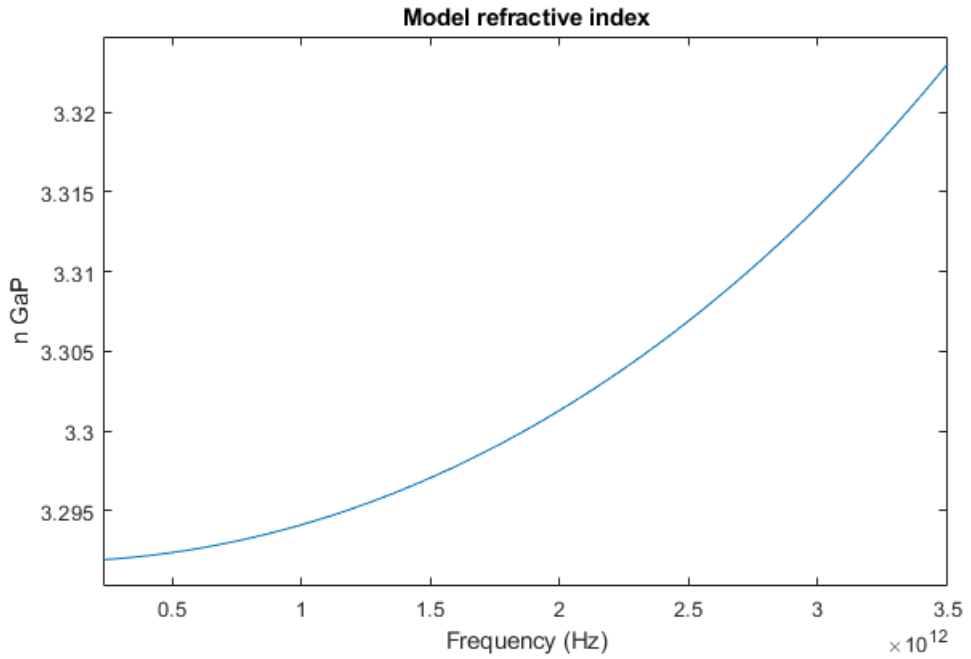

Figure 4.13: Modeled behaviour of the real part of Gallium Phosphide refractive index up to 3.5 THz

A linear phase extrapolation step at signal processing stage is necessary to avoid false phase unwrapping. In the extrapolation process the noisy low frequency part of the transmission function is discarded for phase calculation, while phase calculation and unwrapping is normally performed as described in previous sections for the reliable part of the data. The missing phase profile for low frequencies is then extrapolated from the phase calculated for reliable frequencies assuming a linear phase profile. The whole phase function is eventually forced to start from zero radians at null frequency. The result of low frequencies linear phase extrapolation on the phase profile is clearly visible in Figure 4.14.

The estimates of the real part of GaP refractive index obtained with and without linear phase extrapolation are finally reported in Figure 4.15 along with the theoretical results from equation 4.14.

The most evident element in the graph is the skewed behaviour of the refractive index obtained with standard phase unwrapping which is clearly out of range for low frequencies and never really approaches the theoretical value. In comparison to the theoretical model it is also clear the effect of low frequency errors propagation which cause a general underestimation of the refractive index at all frequencies. On the other hand, the refractive index obtained applying linear phase extrapolation for low frequencies shows a relevant accordance with the theoretical model up to the limit of signal bandwidth ($\sim$ 3 THz). The effect of noise at low frequencies, approximately from 0 to 0.5 THz, is still visible but does not affect the reconstruction at higher frequencies. As it could reasonably be expected, the measure fails to recover the correct refractive index at frequencies higher than the signal bandwidth. Some artifacts, in the form of narrow peaks, are present in the measured refractive index, most probably caused by the presence of water vapour absorption lines in the spectrum.

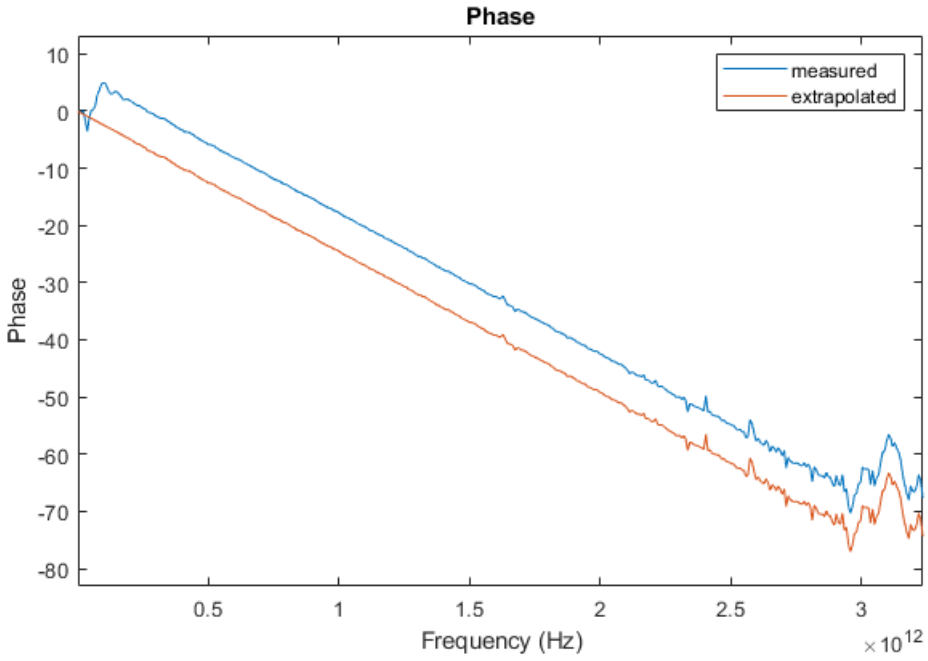

Figure 4.14: Unwrapped phase of GaP transmission function in case of: (blue) standard unwrapping starting at frequency $f = 0$ Hz; and (orange) linear phase extrapolation for low frequencies

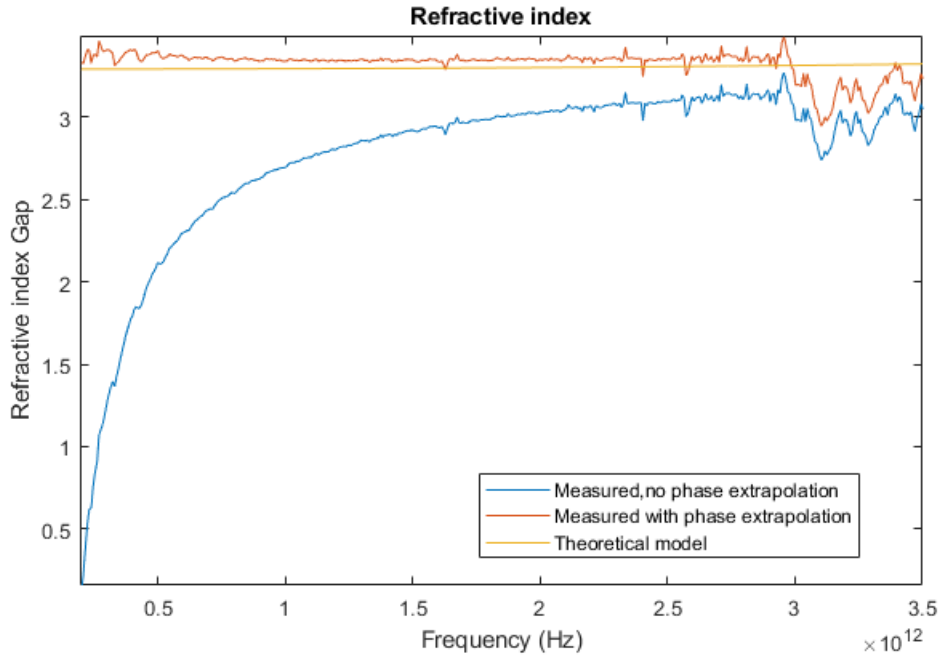

Figure 4.15: Real part of Gallium Phosphide refractive index: (Yellow) Theoretical model; (Blue) Retrieved from measurement with standart phase unwrapping; (Orange) Retrieved from measurement with linear phase extrapolation

4.2.4 Edible oils

One of the most coveted applications of THz technology is the rapid and reliable detection and identification of chemical substances, in particular in food industry where the low invasiveness of the THz spectroscopy measurement process is expected to play a major role in food monitoring and quality control. Real-life applications however have to overcome a series of complications, such as scattering of the THz signal, limited penetration length and complexity of the medium containing the sample under test. THz range absorption lines are indeed very sensitive to even small changes in the environment of the sample due to the low energy of vibrational transitions involved in the absorption process.

Among the rapidly growing literature on the subject of THz food investigation [88], spectroscopy of mineral and edible oils represent a rather active branch, with a discrete amount of experimental data available from different studies, see for example [89, 90]. It was therefore of some interest to carry out the spectroscopy of some edible oil samples and compare the consistency of the gathered data with the available experimental studies. The samples of choice were two different commercial oils, the first one made from olives and the second one from coconut fruits. The particularity of these measures with respect to the ones presented in previous sections is the need of a plastic cuvette, of internal thickness 0.18 mm, in which to place the sample during the measure. For this reason the reference measure has been performed with the empty cuvette in place along the optical path, in such a way to remove the effect of plastic on the sample transmission function. Furthermore, being coconut oil solid at room temperature, its sample has been melted, prior to the measurements, by increasing its temperature above 24°C.

The three measures of time domain traces of the THz signals and the respective spectrum are represented in Figure 4.16 and 4.17.

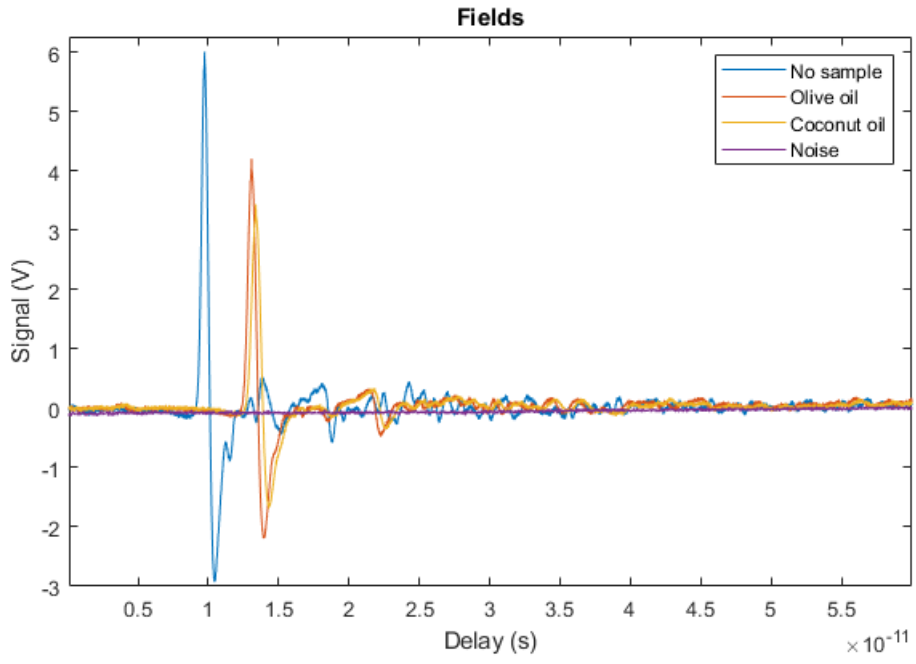

Figure 4.16: Time traces of the measured THz signal for: (blue) Reference measure; (red) Olive oil; (yellow) Coconut oil. The noise floor is represented as well (purple).

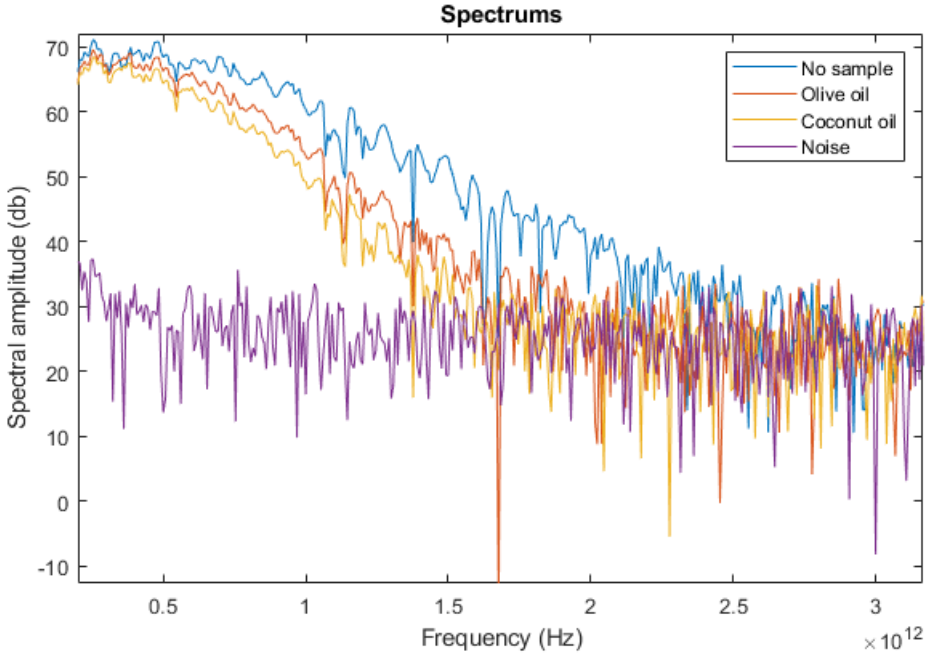

Figure 4.17: Calculated spectra of the measured THz signal for: (blue) Reference measure with no sample; (orange) Plastic sample; (yellow) Paper sample. The noise floor is also represented (purple).

A strong attenuation is clearly visible in the time domain signals of the two samples, with coconut oil peak slightly more delayed and attenuated with respect to the olive oil one. In the frequency spectra it is possible to note a drastic reduction of the spectral amplitude at high frequencies, traceable to the strong absorption of the samples, which effectively limits the signal bandwidth to $\sim$ 1.6 THz. The strong absorption also inevitably results in a generally poorer signal to noise ratio and dynamic range, which in turn have a detrimental effect on the quality of the retrieved optical parameters. The calculated refractive indexes for the two samples are illustrated in Figure 4.18 and can be compared to the ones found in literature, represented in Figure 4.19.

It can be noticed that the measured properties are in line with the one reported in [90] although it is present a general tendency to overestimate the refractive index, in particular for the coconut oil sample. A possible explanation for this trend could be attributed to a possible difference in experimental conditions with respect to [90], regarding in particular the temperature at which the measures have been carried out. A direct correlation between the refractive index of an oil and its viscosity in the THz range has been reported by Naftaly et al. [91]. Being the inverse dependence of a fluid viscosity on its temperature well known, a lower temperature of the samples analyzed in this work could explain the increase in the refractive index observed in both measures with respect to [90]. This could be true especially for coconut oil, in which case the warming procedure needed to bring the sample to liquid state, prior to the measurement process, pose a larger degree of uncertainty over sample's temperature value and stability during the entire measure.

For the calculation of the absorption coefficients, the presence of additional reflection losses at the air-cuvette interface has been taken into account in equation

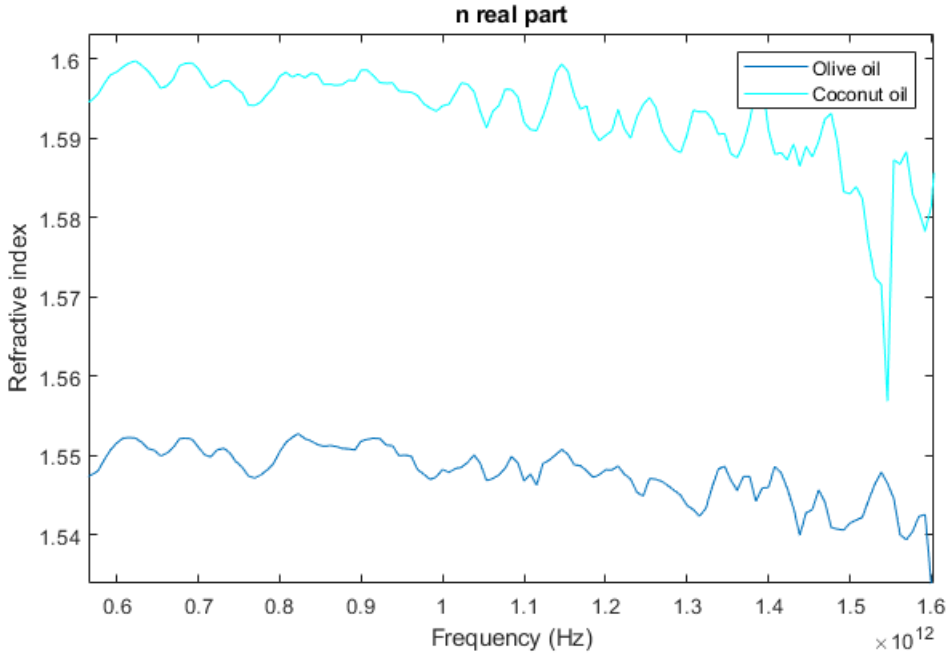

Figure 4.18: Real part of the measured refractive indexes for: (blue) olive oil; (cyan) coconut oil.

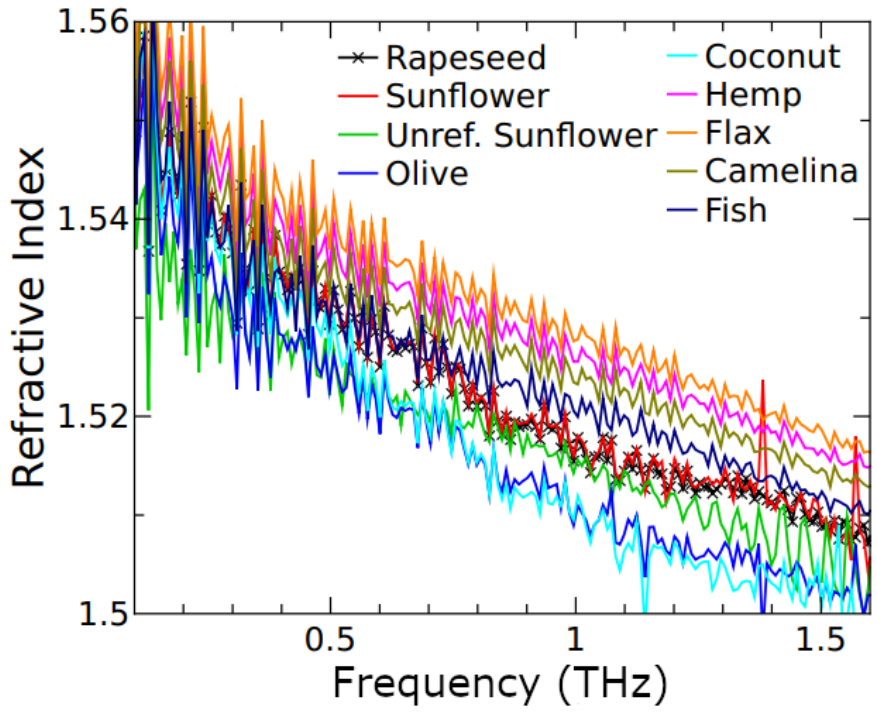

Figure 4.19: Real part of the refractive indexes for different edible oils, after [90]. Olive oil is in blue, coconut oil is in cyan.

4.11 by means of a compensation term L [92]:

$$\alpha(\omega) = -\frac{2}{d}\frac{ln|H(\omega)|}{L} \tag{4.15}$$

where the L coefficient is given by:

$$L = \frac{4n_{cuvette}}{(1+n_{cuvette})^2} \tag{4.16}$$

with $n_{cuvette}$ real part of the refractive index of the plastic cuvette. The calculated absorption coefficients can be found in Figure 4.20 while the data from [90] are represented in Figure 4.21.

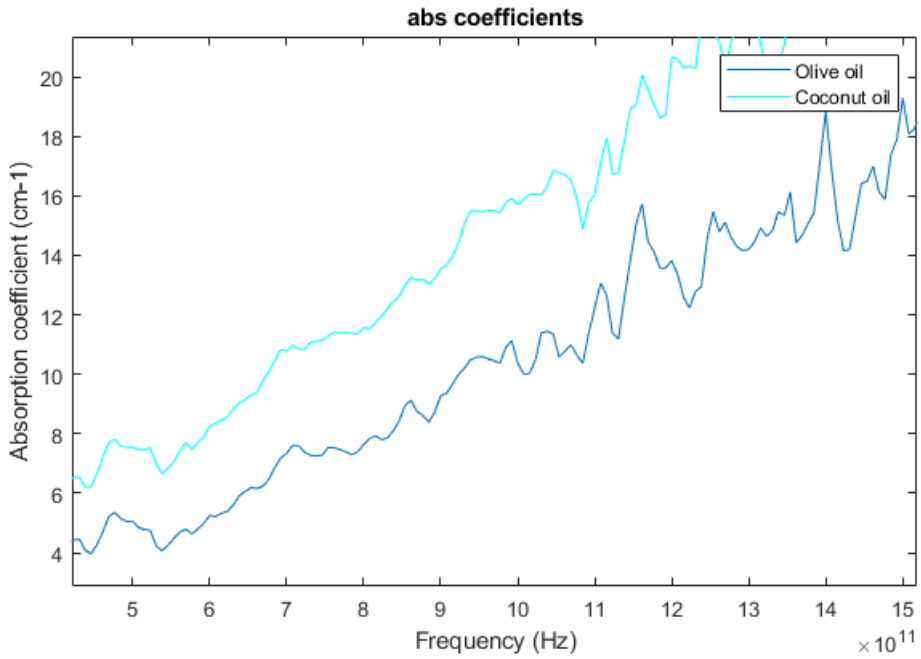

Figure 4.20: Measured absorptin coefficients for: (blue) olive oil; (cyan) coconut oil.

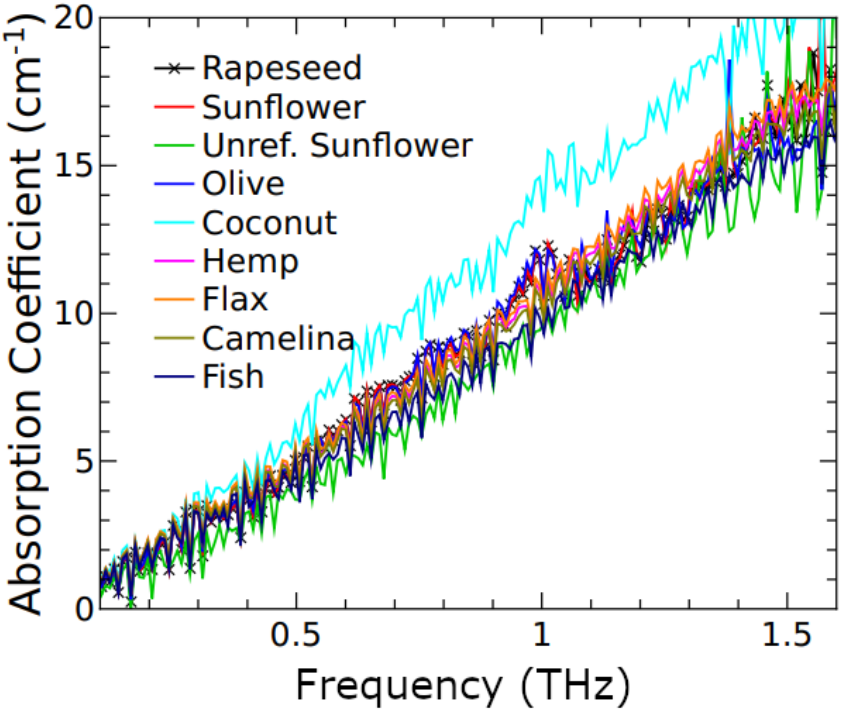

Figure 4.21: Absorption coefficient of different edible oils, after [90]. Olive oil is in blue, coconut oil is in cyan.

Chapter 5

Conclusions and perspectives

This experimental thesis work has reported on the design, development and characterization of a THz time-domain spectrometer, as well as its implementation for the study of the transmission function, complex refractive index and absorption coefficient of different materials. The spectrometer was characterized by a detection bandwidth exceeding 3 THz, in the absence of a sample, and a sub-10 GHz spectral resolution.

The spectroscopic analysis on the paper and plastic samples revealed appreciable differences in the values of the refractive indexes and absorption coefficients in the THz range, although the presence of water vapour along signal's path has produced noticeable artefacts in all the measurements. The measure of Gallium Phosphide's refractive index showed relevant agreement with theoretical models once compensated for the effects of low frequency noise. The spectroscopy of olive and coconut oils demonstrated the capability of the device to discriminate the nature of edible oils, in accordance to the available literature on the subject.

Future perspectives targeted to the improvement in performance of this spectrometer could consist in the embedding of the THz signal in a low vacuum chamber, in order to limit the detrimental effects on the measurements related to strong absorption of water vapour. An alternative viable way to compensate for water vapour absorption could also be to develop numerical methods for the post-measurement removal of the related artifacts, such as the ones presented in [93]. Furthermore, the materials analyzed in this thesis work are just a narrow ensemble among the various chemicals worth of a complete characterization in the THz range, a stimulating potential application for the developed spectrometer could be related to the analysis of gases released during decomposition processes by organic materials, whose fingerprints in the THz range, if present, can be exploited for remote quality control in the food industry.

The seamless implementation in industrial contexts of these kind of spectrometers is still limited, other than by the effect of water absorption, by the size of the devices, mainly due to the large footprint of the Ti:Sapphire laser source, and the need to manually start the mode-locking regime. Both these issues can be addressed in the future with the development of compact, turn-key operation THz spectrometers based on diode-pumped Yb laser sources, either solid state or fiber solutions, like the ones described in the second chapter of this thesis.

Bibliography

1. Auston, D. H. & Nuss, M. C. Electrooptic Generation and Detection of Femtosecond Electrical Transients. *IEEE Journal of Quantum Electronics* **24,** 184–197 (1988).
2. Leisawitz, D. *et al.* Scientific motivation and technology requirements for the SPIRIT and SPECS far-infrared/submillimeter space interferometers. *Proc. SPIE* **4013,** 36–46 (2000).
3. Nagatsuma, T. Terahertz technologies: Present and future. *IEICE Electronic Express* **8,** 1127–1142 (2011).
4. Kazarinov, R. & Suris, R. Possibility of amplification of electromagnetic waves in a semiconductor superlattice. *Sov. Phys. Semicond.* **5,** 707 (1971).
5. Carpasso, F. *et al.* Quantum Cascade Laser. *Science* **264,** 553–556 (1994).
6. Kohler, R. *et al.* Terahertz semiconductor heterostructure laser. *Nature* **417,** 156–159 (2002).
7. Vitiello, M. S., Scalari, G., Williams, B. & De Natale, P. Quantum cascade lasers: 20 years of challenges. *Optic Express* **23,** 5167–5182 (2015).
8. Dhillon, S. S. *et al.* The 2017 terahertz science and technology roadmap. *J. Phys. D: Appl. Phys.* **50** (2017).
9. Lu, Q. & Razeghi, M. Recent Advances in Room Temperature, High-Power Terahertz Quantum Cascade Laser Sources Based on Difference-Frequency Generation. *Photonics* **3** (2016).
10. Wang, F. *et al.* Generating ultrafast pulses of light from quantum cascade lasers. *Optica* **2,** 944–949 (2015).
11. Nisoli, M. *Semiconductor Photonics, Principles and applications* (Esculapio, 2016).
12. Williams, S. B. Terahertz quantum-cascade lasers. *Nature Photonics* **1,** 517–525 (2007).
13. Maestrini, A. *et al.* A 1.7–1.9 THz local oscillator source. *IEEE Microw. Wirel. Compon. Lett.* **14,** 253–255 (2004).
14. Raisaneen, A. & Lehto, A. *Radio Engineering for Wireless Communication and Sensor Applications* (Artech House, 2003).
15. Asada, M., Suzuki, S. & Kishimoto, N. Resonant Tunneling Diodes for Sub-Terahertz and Terahertz Oscillators. *Japanese Journal of Applied Physics* (2008).
16. Feiginov M.and Sydlo, C., Cojocari, O. & Meissner, P. Resonant-tunnelling-diode oscillators operating at frequencies above 1.1 THz. *Applied Physics Letters* **99** (2011).

17. Maekawa, T., Kanaya H. Suzuki, S. & Asada, M. Oscillation up to 1.92THz in resonant tunneling diode by reduced conduction loss. *Applied Physics Express* **9** (2016).

18. Ling, J. *Resonant Tunneling Diodes: Theory of Operation and Applications* University of Rochester, Rochester, 2007.

19. Mazzanti, A. *Terahertz generation by optical rectification in an enhancement cavity of femptosecond Ti:Sa laser* MA thesis (Politecnico di Milano, 2016).

20. Reinmann, K. Table-top sources of ultrashort THz pulses. *Reports on Progress in Physics* **70,** 1597–1632 (2007).

21. Vidal *et al.* Impact of dispersion, free carriers and two-photon absorption on the generation of intense THz pulses in ZnTe crystals. *Applied Physical Letters* **98** (2011).

22. Et al., H. Influence of free-carrier absorption on terahertz generation from ZnTe(110). *Journal of Applied Physics* **107** (2010).

23. Ku, S. A. *et al.* Saturation of the free carrier absorption in ZnTe crystals. *Opt Express* **21,** 13930–13937 (2013).

24. Zhao, Z., Hamaeau, S. & Tignon, J. THz generation by optical rectification and competition with other nonlinear processes. *Chin. Phys. Lett.* **25,** 1868–1870 (2008).

25. Zhang, X.-C. & Xu, J. *Introduction to THz Wave Photonics* (Springer, 2010).

26. Hoffmann, M. C., Ka-Lo Yeh, J. H. & keith A. Nelson. Efficient terahertz generation by optical rectification at 1035 nm. *Optic Express* **15,** 11706–11713 (2007).

27. Smith, P. R., Auston, D. H. & Nuss, C. M. Subpicosecond Photoconducting Dipole Antennas. *IEEE Journal of Quantum Electronics* **24,** 255–260 (1988).

28. Burford, N. M. & El-Shenawee, M. O. Review of terahertz photoconductive antenna technology. *Optical Engineering* **56** (2017).

29. Benicewicz, P. K., Roberts, J. P. & Taylor, A. J. Scaling of terahertz radiation from large-aperture biased photoconductors. *J. Opt. Soc. Am. B* **11,** 2533–2545 (1994).

30. Jepsen, P. U., Jacobsen, R. H. & Keiding, S. R. Generation and detection of terahertz pulses from biased semiconductor antennas. *J. Opt. Soc. Am. B* **13,** 2424–2436 (1996).

31. Lepeshov, S. I., Gorodetsky, A., Krasnok, A. E., Rafailov, E. U. & Belov, P. A. Enhancement of Terahertz Photoconductive Antennas and Photomixers Operation by Optical Nanoantennas. *Physics.Optics* (2016).

32. Darrow, J. T., Zhang, X.-C., Auston, D. H. & Morse, J. D. Saturation Properties of Large-Aperture Photoconducting Antennas. *IEEE Journal of Quantum Electronics* **28,** 1607–1616 (1992).

33. Brown, E., Smith, F. W. & McIntosh, K. A. Coherent millimeter-wave generation by heterodyne conversion in low-temperature-grown GaAs photoconductors. *Journal of Applied Physics* **73,** 1480–1484 (1993).

34. Korter, T. M. & Plusquellic, D. F. Continuous-wave terahertz spectroscopy of biotin: vibrationalanharmonicity in the far-infrared. *Chemical Physics Letters* **385,** 45–51 (2004).

35. Ironside, D. J. *et al.* Enhancing THz generation in photomixers using a metamaterial approach. *Optics Express* **27,** 9481–9484 (2019).

36. Verghese, S., McIntosh, K. A. & Brow, E. R. Optical and terahertz power limits in the low-temperature-growngaas photomixers. *Appl. Phys. Lett.* **72,** 2743–2745 (1997).

37. Verghese, S. *et al.* Generation and detection of coherent terahertz waves using two photomixers. *Applied Physics Letters* **73,** 3824–3826 (1998).

38. Roggenbuck, A. *et al.* Coherent broadband continuous-wave terahertz spectroscopy on solid-state samples. *New J. Phys.* **12** (2010).

39. Luo, J. K. *et al.* The electrical breakdown properties of GaAs layers grown by molecular beam epitaxy at low temperature. *Semicond. Sci. Technol.* **9,** 2199–2204 (1994).

40. Shi, W., Xu, J. & Zhang, X.-C. Terahertz generation from Si_3N_4 covered photoconductive dipole antenna. *Chinese Optics Letters* **1,** 308–310 (2003).

41. Molteni, L. M. *Realization of a THz spectrometer using Photoconductive Antennas* MA thesis (Politecnico di Milano, 2018).

42. Tani, M., Matsuura, S., Sakai, K. & Nakashima, S. Emission characteristics of photoconductive antennas based on low-temperature-grown GaAs and semi-insulating GaAs. *Applied Optics* **36,** 7853–7859 (1997).

43. Castro-Camus, E. & Alfaro, M. Photoconductive devices for terahertz pulsed spectroscopy: a review. *Photon. Res.* **4,** A36–A42 (2016).

44. Hale, P. J. *et al.* 20 THz broadband generation using semi-insulating GaAs interdigitated photoconductive antennas. *Opt. Express* **22,** 26358–26364 (2014).

45. Heshmat, B. *et al.* Nanoplasmonic terahertz photoconductive switch on GaAs. *Nano Lett.* **12,** 6255–6259 (2012).

46. Tani, M. *et al.* Novel Terahertz Photoconductive Antennas. *International Journal of Infrared and Millimeter Waves volume* **27,** 531–546 (2006).

47. Svelto, O. *Principles of Lasers* 5th ed. (Springer, 2010).

48. Keller, U. Recent developments in compact ultrafast lasers. *Nature* **424,** 831–838 (2003).

49. Spence, D. E., Kean, P. N. & Sibbett, W. 60-fsec pulse generation from a self-mode-locked Ti:sapphire laser. *Optics Letters* **16,** 42–44 (1991).

50. Morgner, U. *et al.* Sub-two-cycle pulses from a Kerr-lens mode-locked Ti:sapphire laser. *Optics Letters* **24,** 411–413 (1999).

51. Keller, U. Ultrafast solid-state laser oscillators: a success story for the last 20 years with no end in sight. *Appl. Phys. B* **100,** 15–28 (2010).

52. Haus, H. A., Fujimoto, J. G. & Ippen, E. I. Analytic Theory of Additive Pulse and Kerr Lens Mode Locking. *IEEE Journal of Quantum Electronics* **28,** 2086–2096 (1992).

53. Wang, Y. *Broadband and Ultrafast mid-IR Lasers for High-Precision Molecular Spectroscopy* PhD thesis (Politecnico di Milano, 2019).

54. Keller, U. *et al.* Semiconductor Saturable Absorber Mirrors (SESAM's) for Femtosecond to Nanosecond Pulse Generation in Solid-State Lasers. *IEEE Journal of Selected Topics in Quantum Electronics* **2,** 435–453 (1996).

55. Spuhler, G. J. *et al.* Semiconductor saturable absorber mirror structures with low saturation fluence. *Appl. Phys. B* **81,** 27–32 (2005).

56. Maiman, T. H. Stimulated Optical Radiation in Ruby. *Nature* **187,** 493–494 (1960).

57. *Handbook of solid-state lasers. Materials systems and applications* (eds Dencker, B. & Shklovsky, E.) (Woodhead Publishing, 2013).

58. Koechner, W. & Bass, M. *Solid state lasers. A graduate text* (Springer, 2002).

59. Moulton, P. F. Spectroscopic and laser characteristics of $Ti : A1_20_3$. *J. Opt. Soc. Am. B* **3,** 125–133 (1985).

60. Albers, P., Stark, E. & Huber, G. Continuous-wave laser operation and quantum efficiency of titanium-doped sapphire. *J. Opt. Soc. Am. B* **3,** 134–139 (1986).

61. McClure, D. S. Optical spectra of transition–metal ions in corundum. *The Journal of Chemical Physics* **36,** 2757 (1962).

62. *Solid-State Lasers and Applications* (ed Sennaroglu, A.) (CRC Press Taylor Francis Group, 2007).

63. Zervas, M. N. High power ytterbium-doped fiber lasers — fundamentals and applications. *International Journal of Modern Physics B* **28** (2014).

64. Lacovara, P. *et al.* Room-temperature diode pumped Yb:YAG laser. *Opt. Lett.* **16,** 1089–1091 (1991).

65. Sumida, D. *et al.* Diode-pumped Yb:YAG catches up with Nd:YAG. *Laser Focus World,* 63–70 (1999).

66. Hufner, S. *Optical Spectra of Transparent Rare Earth Compounds* (Academic Press, 1978).

67. Petit, J. *et al.* Quest of athermal solid state laser: case of Yb:$CaGdAlO_4$. *Advanced Solid State Photonics,* paper WD1 (2006).

68. Petit, J., Goldner, P. & Viana, B. Laser emission with low quantum defect in Yb:$CaGdAlO_4$. *Optics Letters* **30,** 1345–1347 (2005).

69. Snitzer, E. Optical Maser Action on Nd^{3+} in a Barium Crown Glass. *Phys. Rev. Lett.* **7,** 444–446 (1961).

70. Snitzer, E. Glass lasers. *Applied Optics* **5,** 1487–1499 (1966).

71. Snyder, A. W. & Love, J. D. *Optical Waveguide Theory* (Chapman and Hall, 1983).

72. Wang, Y. *Femtosecond Ti:Sapphire ring laser with a stabilized pulse repetition rate of 250 MHz* MA thesis (Politecnico di Milano, 2015).

73. *Verdi family Datasheet* Coherent Inc. (2011). `https://www.coherent.com/assets/pdf/Verdi-Family-Data-Sheet.pdf`.

74. Smith, N. J., Blow, K. J. & Andonovic, I. Sideband Generation Through Perturbations to the Average Soliton Model. *Journal of Lightwave Technology* **10,** 1329–1333 (1992).

75. *TERA8-1-SpecSheet* Menlo Systems, Inc (2017). `https://www.thorlabs.com/thorproduct.cfm?partnumber=TERA8-1`.

76. *T8-H2 Mount for TERA8-1 THz Antenna* Menlo Systems, Inc (2017). `https://www.thorlabs.com/thorproduct.cfm?partnumber=T8-H2`.

77. *Newport PM500Series, Operation and Command Reference Manual* Newport Corporation (2001). `https://www.equipx.net/uploads/Newport-Kensington/NewportPM500-operation-and-command.pdf`.

78. *MPD249-M03 - Ø2" 90 Off-Axis Parabolic Mirror, Unprot. Gold, RFL = 4"* Thorlabs (2015). `https://www.thorlabs.com/thorproduct.cfm?partnumber=MPD249-M03`.

79. Withayachumnankul, W. & Naftaly, M. Fundamentals of Measurement in Terahertz Time-Domain Spectroscopy. *J Infrared Milli Terahz Waves* **35,** 610–637 (2014).

80. Mickan, S. P., Xu, J., Munch, J., Zhang, X.-C. & Abbott, D. The limit of spectral resolution in thz time-domain spectroscopy. *SPIE Microelectronics, MEMS, and Nanotechnology,* 54–64 (2004).

81. Naftaly, M. & Dudley, R. Methodologies for determining the dynamic ranges and signal-to-noise ratios of terahertz time-domain spectrometers. *Optics Letters* **34,** 1213–1215 (2009).

82. Duvillaret, L., Garet, F. & Coutaz, J.-L. A reliable method for extraction of material parameters in terahertz time-domain spectroscopy. *IEEE Journal of Selected Topics in Quantum Electronics* **2,** 739–746 (1996).

83. Jepsen, P. U. & Fischer, B. M. Dynamic range in terahertz time-domain transmission and reflection spectroscopy. *Optics letters* **30,** 29–31 (2005).

84. Cabo, J. V. *et al.* Windowing of THz time-domain spectroscopy signals: A study based on lactose. *Optics Communications* (2016).

85. Faure, J., Van Tilborg, J., Kaindl, R. A. & Leemans, W. P. Modelling Laser-Based Table-Top THz Sources: Optical Rectification, Propagation and Electro-Optic Sampling. *Opt. Quantum Electron* **36,** 681–697 (2004).

86. Dietze, D., Unterrainer, K. & Darmo, J. Dynamically phase-matched terahertz generation. *Optics Letters* **37,** 1047–1049 (2012).

87. Leitenstorfer, A., Hunsche, S., Shah, J., Nuss, M. C. & Knox, W. H. Detectors and sources for ultrabroadband electro-optic sampling: Experiment and theory. *Appl. Phys. Lett.* **74,** 1516 (1999).

88. Afsah-Hejri, L. *et al.* A Comprehensive Review on Food Applications of Terahertz Spectroscopy and Imaging. *Comprehensive Reviews in Food Science and Food Safety* **18,** 1563–1621 (2019).

89. Yin, M., Tang, S. & Tong, M. Identification of edible oils using terahertz spectroscopy combined with genetic algorithm and partial least squares discriminant analysis. *Anal. Methods* **8,** 2794–2798 (2016).

90. Karaliunas, M. *et al.* Non-destructive inspection of food and technical oils by terahertz spectroscopy. *Nature Scientific Reports* **8** (2018).

91. Naftaly, M. *et al.* Terahertz transmission spectroscopy of nonpolar materials and relationship with composition and properties. *Int. J. Infrared Millim. Waves* **26,** 55–64 (2005).

92. Karaliunas, M. *et al.* Supplementary information for the paper: "Non-destructive inspection of food and technical oils by terahertz spectroscopy". *Nature Scientific Reports* **8** (2018).

93. Withayachumnankul, W., Fischer, B. M. & Abbot, D. Numerical removal of water vapour effects from terahertz time-domain spectroscopy measurements. *Proc. R. Soc. A* **464,** 2435–2456 (2008).